UNIVERSITÀ
DEGLI STUDI
FIRENZE

PhD in
Earth Science

CYCLE XXXV

COORDINATOR Prof. Sandro Moretti

NEW TECHNOLOGIES AND MULTIDISCIPLINARY APPROACHES FOR ANALYZING CLIMATE CHANGE EFFECTS AND ANTHROPOGENIC IMPACTS ON A VULNERABLE AREA: THE EXAMPLE OF A TUSCAN COASTAL PLAIN

PhD Candidate

Dr. Marco Luppichini

Supervisor

Prof. Monica Bini

Co-Supervisor

Prof. Roberto Giannecchini

Years 2019 – 2022

Contents

List of Figures

1 Introduction

Current global warming directly affects the different components of the hydrological cycle (Allan, 2011; Bates et al., 2008). Such components include rainfall and temperature patterns, frequency and intensity of extreme events, and changes in soil moisture (Stagl et al., 2014; Xu et al., 2011), with substantial consequences in terms of socio-economic conditions and financial policy of the countries involved. For instance, from 1980 to 2017 Germany, Italy, France, and the United Kingdom are the European countries that have spent the highest amount of money as a result of the impact of extreme weather and climate-related events (European Environment Agency, 2019).

The annual rainfall amount is influenced by current global warming with spatial differences in Europe where there are areas characterized by an increase in rainfall and a decrease in other areas (Bertola et al., 2019; Blöschl et al., 2019). Current global warming also influences the probability of Extreme Precipitation Events (EPE) caused by an increase in energy and water vapor in the atmosphere (Jonkman, 2005; Tramblay et al., 2013; Westra et al., 2014). The change in rainfall regimes induces pressures and variations on the environments related to the hydrological cycle. The coasts are certainly vulnerable to global warming because of sea-level rise and potential increase in storms (Bini and Rossi, 2021; Ericson et al., 2006). Indeed, rainfall regime change induces a variation of the river capacities to transport solid load, and this can induce an increase in the vulnerability of these environments (Anthony, 2018; Anthony et al., 2014; Besset et al., 2019; Ericson et al., 2006)

1.1 Research aims

This work aims to investigate the rainfall regime variations and to improve the knowledge of the influence of climate change in Tuscany (central Italy). The region has a strategic location: it is situated in the northern sector of the Mediterranean, in the proximity of the Genoa Gulf, by far the most active cyclogenetic center of the Mediterranean (Trigo et al., 2002). The different influences of current global warming on the rainfall regimes, highlighted for northern and southern Europe, induces to have transition zones and central Italy is located in one of these transition zones (Blöschl et al., 2019). However, the accuracy of previous studies carried out on a large-scale does not allow to identify the bounders with great precision. As a matter of fact, these studies are poorly supported by the use of several number of stations, mainly in the

Mediterranean (Blöschl et al., 2019; Deitch et al., 2017; Huo et al., 2021). More detailed studies and the use of larger amounts of data will be necessary to improve the knowledge of these transition zones.

Specifically, the purpose of this climatic work is to investigate the rainfall seasonal trends of the last 70 years in relation to mesoscale circulation and to atmospheric teleconnections. The rainfall dataset employed came from several raingauges with high spatial density and temporal activity from 1950 to 2020. The large number of raingauges allowed us to investigate the rainfall trend in great detail and with direct measurements. The rainfall trends are compared with the NAO, EA and WeMO indices by means of mathematical and statistical methods designed to understand how the climatic trends influence the rainfall regime in this area. We investigated the link between the different indices by using traditional statistical methods (Spearman, 1904) and by introducing an innovative approach, which employs a linear model to understand the influence of each index on rainfall prediction. The combination of these different methods can help us understand the accuracy and the advantages of the new method proposed. In this study, we compare the SSTs with the atmospheric indices to improve knowledge on the rainfall trend and to understand possible future scenarios.

This study also aims to investigate the rainfall-temperature relationship by analyzing the temperature anomalies occurred during the EPEs and by calculating the CC relation for more than 100 rain gauges and for sub-daily and daily rainfalls. This high spatial resolution allows to identify the different effects of temperature on the rainfall regime and to improve the knowledge of an important area of the Mediterranean.

The Pisan coastal plain of Tuscany has been selected to study both the effects of current global warming and the anthropogenic factors on the coastal environment. The long series of data available for the Pisa coastal plain has made it possible to better understand the current evolution and to predict future trends. In this study, we intend to relate the costal erosion to the geomorphological features of the coast, to remote-sensing analysis, and to river flow discharge data. The Pisan coastal plain has been affected by marked erosive coastal processes since the late nineteenth century (1850–1870) (Besset et al., 2019, 2017; Bini et al., 2008; Borgh, 1970; Grottoli et al., 2019; Palla, 1983; Pozzebon et al., 2018; A.R. Toniolo, 1910). Here, the temporal evolution of erosion and the possible effects of the construction of anthropogenic defenses have been extensively studied (Bertoni and Mencaroni, 2015; Bini et al., 2008; Pranzini et al., 2018), while the primary causes of this phenomenon have been less analyzed.

In the awareness of the effects and future scenarios based on current global warming, this work proposes two tools that can help improve territory management. The coastal territory must be monitored so that the infrastructures capable of protecting and safeguarding the environment can be implemented. Coastal environment monitoring is an important procedure and the basis for the correct construction of infrastructures and interventions capable of mitigating and preserving these environments. This work proposes a new method based on the beach profile derived from high resolution Digital Elevation Model (DEM) to identify the shoreline position. More specifically, we suggest a method based on Structure from Motion (SfM) techniques to build a high-resolution DEM from UAV images. We believe this innovative method can be better applied in various contexts with respect to techniques based on image colours, which are influenced by several factors such as acquisition time, period of year, cloudy weather conditions, and waves. These factors have often strongly influenced the results, whereas a method based on beach topography is more objective.

The second tool proposed in this work is aimed at improving the management of flood events through the use of artificial intelligence techniques. Specifically, the goal of this work is to demonstrate that deep-learning approaches can be employed to predict flood events in watersheds characterized by fast flood events. The study area is represented by the Arno River basin (in Tuscany), which experienced many damaging floods in the past (Becchi, 1986; Caporali et al., 2005), and which is characterized by very sudden events that developed in less than 24 hours. We use very high-frequency data for a detailed reconstruction of flood events. The work is designed to create deep-learning models able to predict flood events within a few hours' notice. The architecture of the applied deep-learning model is based on an encoder-decoder LSTM layer, by simply using rainfall and hydrometric height data. The few types of data exploited by a deep-learning model, as opposed to a physically-based model, allows the user to apply the same techniques of this study to different cases. Deep-learning techniques will make it possible to create catchments models for which there is scarce territorial information. Many studies have applied these techniques to large river basins characterized by multi-day events. Some examples may include studies that have involved several watersheds scattered across various continents (Boulmaiz et al., 2020; Kratzert et al., 2018), large basins of North America (Chattopadhyay et al., 2020), and Chinese rivers having large flow rates (Le et al., 2019; Li et

al., 2020; Liu et al., 2020; Van et al., 2020). Thus, the application of the method to smaller catchments is excellent news and of relevant importance for many purposes.

A systematic scheme of the study goals is displayed in Figure 1.1.

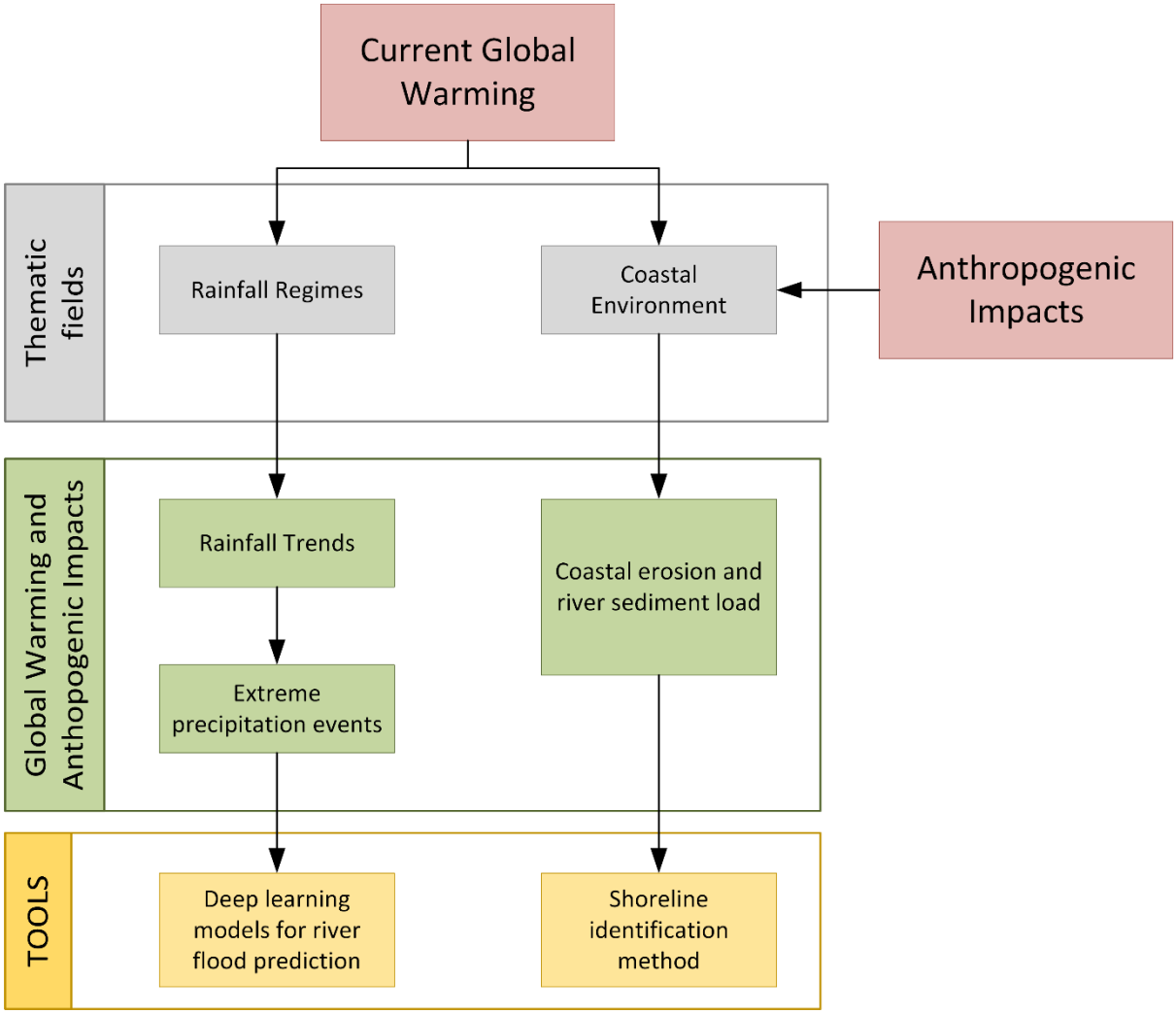

Figure 1.1. Flowchart of the aims of this study.

1.2 Effects of climate change on rainfall regimes

The Mediterranean region is an ideal research testbed for current climatic changes because it is located in a transition zone and is considered a hot spot for future climatic changes (Giorgi, 2006). The Mediterranean, situated between the European humid domain and the North African arid belt, provides alternating circulation regimes with large spatial and temporal variability (Dünkeloh and Jacobeit, 2003). In this context, a correct study of rainfall regimes can improve the management of water resources (Tramblay et al., 2020) and extreme events (Cardoso Pereira et al., 2020; Myhre et al., 2019). Several studies have identified a

general decrease (although with some exceptions) in the annual rainfall amount in the area of the Mediterranean basin (Bertola et al., 2019; Blöschl et al., 2019; Caloiero et al., 2018, 2011; Caporali et al., 2021; Colantoni et al., 2015; Deitch et al., 2017; Dünkeloh and Jacobeit, 2003; Halifa-Marín et al., 2021; Longobardi and Villani, 2010; Martin-Vide and Lopez-Bustins, 2006; Philandras et al., 2011; Ríos-Cornejo et al., 2015), as well as atmospheric patterns related to mesoscale circulation (Brandimarte et al., 2011; Caloiero et al., 2011; Halifa-Marín et al., 2021; Lopez-Bustins et al., 2008; Luppichini et al., 2022b, 2021; Martinez-Artigas et al., 2021; Ríos-Cornejo et al., 2015; Trigo et al., 2004).

During the winter months, one of the main drivers of rainfall variability in southern Europe and in the Mediterranean is the presence of different pressure fields over the Northern Atlantic Ocean and their variability indicated as the North Atlantic Oscillation (NAO) (Hurrell, 1995). NAO is defined by an index measured as a north-southern dipole of pressure anomalies, with one pole located at higher latitudes (Iceland Low 80°N) and the other at the central latitudes of the North Atlantic between 35°N and 40°N (Azores High). The East Atlantic (EA) index is similar to that of NAO but is displaced south-eastward to the approximate nodal lines of the NAO pattern. The EA index is often interpreted as a downward-shifted NAO model, but its strong subtropical link entails a different peculiarity. The EA values increase with a significant drop in pressure occurred in the Atlantic Ocean; at the same time, the subtropical oceanic anticyclone belt rises considerably in latitude and reinforces itself. In response, the African anticyclone gains energy and invasiveness over the Mediterranean, subjecting this area to frequent pulses of hot and dry Saharan air in all seasons (Climate Prediction Center, 2021; Mellado-Cano et al., 2019).

The NAO and EA indexes present interannual and annual variabilities with positive and negative phases. The rainfall in the Mediterranean can be associated with a negative phase of NAO and/or EA, when we observe an expansion of the Iceland Low. Instead, during a positive phase of NAO and/or EA, Northern Europe is the rainiest area (Rousi et al., 2020). Both NAO and EA are influenced by the Sea Surface Temperature (SST) of the Northern Atlantic Ocean (NASST) and of the Mediterranean (MSST). An increase in NASST and in MSST is correlated to an expansion of the Azores High and to a consecutive reduction of the Iceland Low, which results in the formation of the NAO and EA positive phases (Frankignoul et al., 2003; Robertson et al., 2000; Visbeck et al., 2001). More recently, NAO has been correlated to the Atlantic Multidecadal Oscillation (AMO), a representative index of the NASST trend (Knight et al., 2005). AMO

changes the zonal position of the NAO center of action, moving the cyclonic area closer to Europe or to North America. During a positive phase of AMO, the Icelandic Low moves further towards North America, while the Azores High moves further towards Europe, and vice versa, for the negative phase of AMO (Börgel et al., 2020). The statistical correlation between the NAO and the winter rainfalls in Europe varies over time (Vicente-Serrano and López-Moreno, 2008), and this is in relation with the NAO and AMO indices (Luppichini et al., 2021).

The Western Mediterranean oscillation (WeMO) is an index often used to study rainfall variability in alternative to NAO in the Mediterranean region. The WeMO index is the difference of atmospheric pressure in a dipole, with the first pole located in Padua (45.40◦N, 11.48◦E) in northern Italy, and the second one located in San Fernando, Cádiz (36.28◦N, 6.12◦W) in southwestern Spain (Climatic Research Unit, 2021). More specifically, the former is located in the Po plain (an area with relatively high barometric variability due to the different influence of the central European anticyclone and the Genoa Gulf Low), while the latter pole is located in the Gulf of Cádiz in the southwest of the Iberian Peninsula, often subject to the influence of the Azores anticyclone and, episodically, to the cut-off of circumpolar lows, or to its own cyclogenesis (Halifa-Marín et al., 2021; Lopez-Bustins et al., 2020; Martin-Vide and Lopez-Bustins, 2006). A positive phase of WeMO is associated with a low-pressure area in the Ligurian Sea and with an anticyclone in the Gulf of Cadiz. Instead, a negative phase of the index determines a low in the Gulf of Cadiz and an anticyclone in Central Europe. WeMO is influenced by the NASST and MSST, but also by the Genoa Gulf Sea-Surface Temperature (GGSST), with positive values correlating to low values of SST (Martín et al., 2012; Martin-Vide and Lopez-Bustins, 2006). Current global warming causes a progressive increase in NASST, MSST and GGSST (Pastor et al., 2020; Wang and Dong, 2010), so that NAO and EA are likely to be characterized by more positive phases, and WeMO by more negative phases.

Global warming also induces a change in the EPEs, which are one of the most frequent natural hazards that induce landslides and floods, causing severe negative consequences on the society, environment, and economy (Jonkman, 2005; Tramblay et al., 2013; Westra et al., 2014). The expected increase in EPEs is primarily based on the increase in atmospheric saturation vapor pressure as a function of temperature, governed by the Clausius-Clapeyron (CC) relation, at a rate of ~7%/ºC at the Earth's surface (Allan et al., 2010; Allen and Ingram, 2002; Pall et al., 2007; Trenberth et al., 2003).

In the last years, several works have investigated the variation of extreme precipitation intensity on the variation of temperature. In other applications combined temperature-humidity measures, such as the dew point temperature, have been used as alternative measures to study the combined effect of air temperature and moisture availability (Ali et al., 2018; Lenderink et al., 2011; Lenderink and van Meijgaard, 2008; Lepore et al., 2015). Some observational studies conducted in different zones of the world have demonstrated scaling rates that are either higher (super-CC) or lower (sub-CC) than CC scaling (e.g., Berg et al., 2013; Blenkinsop et al., 2015; Hardwick Jones et al., 2010; Pumo et al., 2019). Seasonality plays an important role in defining the scaling rate for precipitation (Berg et al., 2009) and several works are identified a change of scaling rates in relation with seasons (Allan et al., 2010; Haerter et al., 2010; Hardwick Jones et al., 2010). In general, a greater increase in winter than in summer in areas characterized by high mean temperature (>24°C), and negative scaling rates have been observed (Haerter et al., 2010; Hardwick Jones et al., 2010; Panthou et al., 2014; Shaw et al., 2011). Basically, this could imply a decrease in extreme rainfall intensities as temperatures rise; however, it could also be the result of lower humidity at higher temperatures (Lenderink et al., 2018). Wet regions have been extensively investigated, but there are still very few applications in arid or semi-arid areas, most of which adopt global spatial scales and show scaling below CC (O'Gorman and Muller, 2010), consistent with the evidence from previous studies (e.g., Pall et al., 2007; Wentz et al., 2007).

1.3 Effects of climate change on coastal environments

In the last decades coastal erosion has become one of the main environmental threats worldwide (Bird et al., 1985; IPCC, 2018; Lenôtre et al., 2004; Luijendijk et al., 2018). Approximately 28,000 km^2 of the global coastline were eroded between 1984 and 2015 and about twice as many as those formed by accumulation processes (Mentaschi et al., 2018). The foreseen future scenario for coastal zones will worsen as a result of the gradual sea-level rise and of the possible increase of extreme events due to global warming (IPCC, 2013). Specifically, the Mediterranean region is severely affected by the impact of extreme climatic events (e.g., storm surges) coupled with human-induced pressures (e.g., poorly planned buildings on the coast, dam construction, land use changes inland), resulting in growing vulnerability of the coastal areas (Toimil et al., 2020). The change in land cover dynamics is considered one of the most important variables of global change affecting the coastal systems, especially for the effects on river sediment supply (Billi and Fazzini,

2017; Blöschl et al., 2019; Petropoulos et al., 2015; Toimil et al., 2020). A decrease in solid load documented for several river-systems of the Mediterranean basin (e.g., Nile, Ebro, Rhône), in particular after the 1970s (Besset et al., 2019; Billi and Fazzini, 2017; Degeai et al., 2020; Pratellesi et al., 2018), has been considered one of the dominant causes of coastal erosion, together with subsidence and sea-level rise (Anthony et al., 2014; Ericson et al., 2006; Syvitski et al., 2009; Tessler et al., 2016).

Despite the importance of a correct estimation of solid load, for many Mediterranean rivers solid load measurements are inadequate, probably because they are cost- and time-consuming, and difficult to sample for the acquisition of reliable long-term data. For these reasons, the contribution of solid load in countering coast erosion is largely speculative. Fewer data are available regarding the dynamics of long- and off-shore dispersion of sediments carried by rivers, which is another key point for the understanding of coastal erosion dynamics.

1.4 Tools

The study of the effects of global warming allows to identify possible future scenarios of environmental changes and the geo-risks. The next step of these studies must be to propose tools and technologies able to improve the management of anthropogenic and climate pressures on the territory.

The coastal environment evolution caused by climate processes and anthropic pressures induces to use monitoring systems with a higher accuracy and precision to highlight variations of the environment status. However, at the same time, the new data and the data from the past (derived from such as cartographies and aerial photographs) must be comparable to each other. For this reason, the shoreline position is the proxy of the coastal evolution which lends itself more to merging future data (high resolution DEMs, multispectral images, etc.) with those of the past. For these reasons, this PhD study want to propose a new tool for the sample of the shoreline position based on high-resolution data.

The change in the rainfall regime and intensity on a Mediterranean scale induces the need for innovative tools for predicting flood events for correct and more efficient territory management. The geological complexity of hydrographic basins means that the numerical modeling of flow regimes is not always satisfactory for an efficient warning against flood phenomena. Simplifying the mathematical problem, artificial intelligence methods can be a valid alternative to physical models. The possibility of having

different tools for predicting flood events can significantly improve territorial management. For this reason, this PhD thesis proposes a tool for the application of artificial intelligence models for the prediction of flood events.

1.4.1 Shoreline monitoring

The monitoring of coastal areas is very important and meaningful to safeguard the benefits that these areas bring to the environment and to the human activities. Monitoring starts with the control of the shoreline, which is the line where the land meets the sea. Shorelines are idealized as the dynamic interface between water and land (Dolan, R., Hayden, P.B., May, P., May, 1980) and, in agreement with Boak and Turner (2005), there are two main categories of shoreline indicators: the first category includes the technique based on the detection or identification of visible features (e.g., instantaneous water lines, vegetation lines); the second category includes the methodologies based on the intersection of the coastal profile with a specific elevation datum like the 0m Above Mean Sea Level (AMSL). Furthermore, different methodologies exist for coastal monitoring, which are based on direct and remote acquisition systems. Direct shoreline acquisition systems are generally applied by using instruments that permit to directly sample the shoreline position, for example the Differential Global Positioning System (DGPS) technique of post-processing or of real-time methodology (Di Luccio et al., 2018; Kelly and Gontz, 2018). The main drawback of these methods lies in the amount of time required to cover large stretches of coastline. Remote sensing for correct positioning of the shoreline can be distinguished by the observation of satellite images (Dewi and Bijker, 2020; García-Rubio et al., 2015; Kabir et al., 2020; Li and Gong, 2016; Vos et al., 2019b), Unmanned Aerial Vehicles (UAV) (Mahabot et al., 2017; Nunziata et al., 2019; Pitman et al., 2019; Templin et al., 2018), video monitoring (Bouvier et al., 2017; Mackenzie et al., 2016), historic airborne images, and historic cartography (Bini et al., 2008; Moussaid et al., 2015). These methodologies are characterized by a different resolution and accuracy not always sufficient to deeply investigate the coastal dynamics. However, they are the only methodologies that allow us to investigate past evolution and to obtain time series.

Several techniques designed to discriminate between sea and land have been proposed to extract shorelines from images. Plant and Holman (Plant and Holman, 1997) employed a method initially developed for grey-scale cameras, called Shoreline Intensity Maximum (SLIM). Recently, with the adoption of color cameras, spectral information has also been exploited to identify the shoreline, using the water property to

absorb the Red signal (R) and the sand property to absorb the Green (G) and blue signals (Smith and Bryan, 2007).

Some studies use Digital Elevation Models (DEM), for example derived by LiDAR (e.g., Parrish et al., 2010; Stockdon et al., 2002), which do not always have a sufficient resolution due to flight height, and this is their main limit. Other studies use UAV images to extract high resolution DEMs for the study of volume variation over time (e.g., Papakonstantinou et al., 2015; Pollard et al., 2019). With these methodologies, it is necessary to perform further sampling, but the result always yields volume variation. Moreover, the results of these topographical surveys are difficult to compare with those of past measurements performed by using instruments like cartography, DGPS, etc.

1.4.2 Deep Learning models for river flow prediction

River flow-prediction is a fundamental goal for early flood warning, water resource management, water demand assessment, irrigation, agriculture, and hydroelectric power generation. These aspects become more and more critical in the context of climate changes. The extreme weather events causing flash floods, floods, and debris flow phenomena have relevant socio-economic implications and represent a significant scientific issue producing extensive literature on the subject (e.g., Bates et al., 2008; Bryndal et al., 2017; Gaume et al., 2016, 2009; IPCC, 2014).

The method most currently used for modelling of the hydrologic scenario simplifies the hydrologic system features to predict their behaviour (Antonetti and Zappa, 2018). The physical models aim to understand and replicate the natural events by using mathematical and numeric methods based on several parameters simplifying the natural phenomena (Jaiswal et al., 2020). However, the systems in nature (including the hydrologic ones) are inherently heterogeneous (Marçais and de Dreuzy, 2017) and physically-based models may show inherent limitations in reproducing natural phenomena (Islam, 2011). Furthermore, in a physical hydraulic model, a wrong setting or an incorrect estimation of the parameters cause an increase in model errors, since they are the main drawback of the physical models (Luppichini et al., 2019).

The recent developments of artificial intelligence (AI) and graphic processor units (GPU) have enabled advancements in deep-learning applications, and innovative approaches based on multilayer artificial neural networks (ANN) (Goodfellow et al., 2016; LeCun et al., 2015). The application of deep-learning models in

various real-world cases, especially in the time series prediction (Fawaz et al., 2020; Yi et al., 2019; Zheng et al., 2019) has been successful. These procedures are the most appropriate to tackle the noisy and chaotic nature of the time series forecasting problems (Livieris et al., 2020). Several authors have applied different deep-learning techniques to predict river flows, with promising results (Boulmaiz et al., 2020; Chattopadhyay et al., 2020; Kratzert et al., 2018; Marçais and de Dreuzy, 2017; Sit et al., 2020; Tien Bui et al., 2020; Van et al., 2020). The long short-term memory (LSTM) is one of the most popular, efficient and deeply used learning techniques (Fawaz et al., 2020), widely applied in flood prediction studies (Boulmaiz et al., 2020; Hu et al., 2020; Kratzert et al., 2018; Le et al., 2019; Li et al., 2020; Liu et al., 2020; Nguyen and Bae, 2020).

1.5 Structure of the thesis

The thesis is divided into four sections: i) Climatology, rainfall trends, and influences of global warming; ii) Relationship between river discharge and coastal erosion; iiii) Shoreline identification method; iv) Deep learning models to predict flood events. The methods, results and discussions are reported for each section. Finally, there is a Conclusions section which summarizes, elaborates, and links the conclusions of the three sections.

Parts of this PhD research were published in the following papers:

1. Luppichini, M., Bini, M., Paterni, M., Berton, A., Merlino, S., 2020. A new beach topography-based method for shoreline identification. Water (Switzerland) 12, 1–11. https://doi.org/10.3390/w12113110
2. Bini, M., Casarosa, N., Luppichini, M., 2021. Exploring the relationship between river discharge and coastal erosion: An integrated approach applied to the Pisa coastal plain (Italy). Remote Sensing 13. https://doi.org/10.3390/rs13020226
3. Luppichini, M., Barsanti, M., Giannecchini, R., Bini, M., 2021. Statistical relationships between large-scale circulation patterns and local-scale effects: NAO and rainfall regime in a key area of the Mediterranean basin. Atmospheric Research 248, 105270.
4. Luppichini, M., Barsanti, M., Giannecchini, R., Bini, M., 2022. Deep learning models to predict flood events in fast-flowing watersheds. Science of The Total Environment 813, 151885. https://doi.org/https://doi.org/10.1016/j.scitotenv.2021.151885

5. Luppichini, M., Bini, M., Barsanti, M., Giannecchini, R., Zanchetta, G., 2022. Seasonal rainfall trends of a key Mediterranean area in relation to large-scale atmospheric circulation: How does current global change affect the rainfall regime? Journal of Hydrology 612, 128233. https://doi.org/https://doi.org/10.1016/j.jhydrol.2022.128233

2 Climatology, rainfall trends, and influences of global warming

2.1 Tuscany and its climate features

Tuscany has a strategic location being located in the northern sector of the Mediterranean, near of the Genoa Gulf, by far the most active cyclogenetic centre of the Mediterranean (Trigo et al., 2002). As expected, the mean annual precipitation (MAP) in Tuscany is influenced by morphology (Figure 2.1a). The rainiest areas are located at the highest altitudes (Apuan Alps and Northern Apennines; Figure 2.1b). In particular, the Apuan Alps in north-western Tuscany show some of the highest rainfall amounts in Italy (Giannecchini and D'Amato Avanzi, 2012; Rapetti and Vittorini, 1994), often characterized by high intensity (D'Amato Avanzi et al., 2004; Giannecchini, 2006). In Tuscany, MAP is in a range of 400-3000 mm/year with a clear gradient from the northern to the southern (Figure 2.1a). The main rainy season is autumn, with a progressive decrease that generally starts in December. The mean rainfall in the DJF (December-January-Febraury) season is ca 300 mm, ca 250 mm in MAM (March-April-May), ca 130 mm in JJA (June-July-August), and ca 350 mm in SON (September-October-November; Figure 2.1).

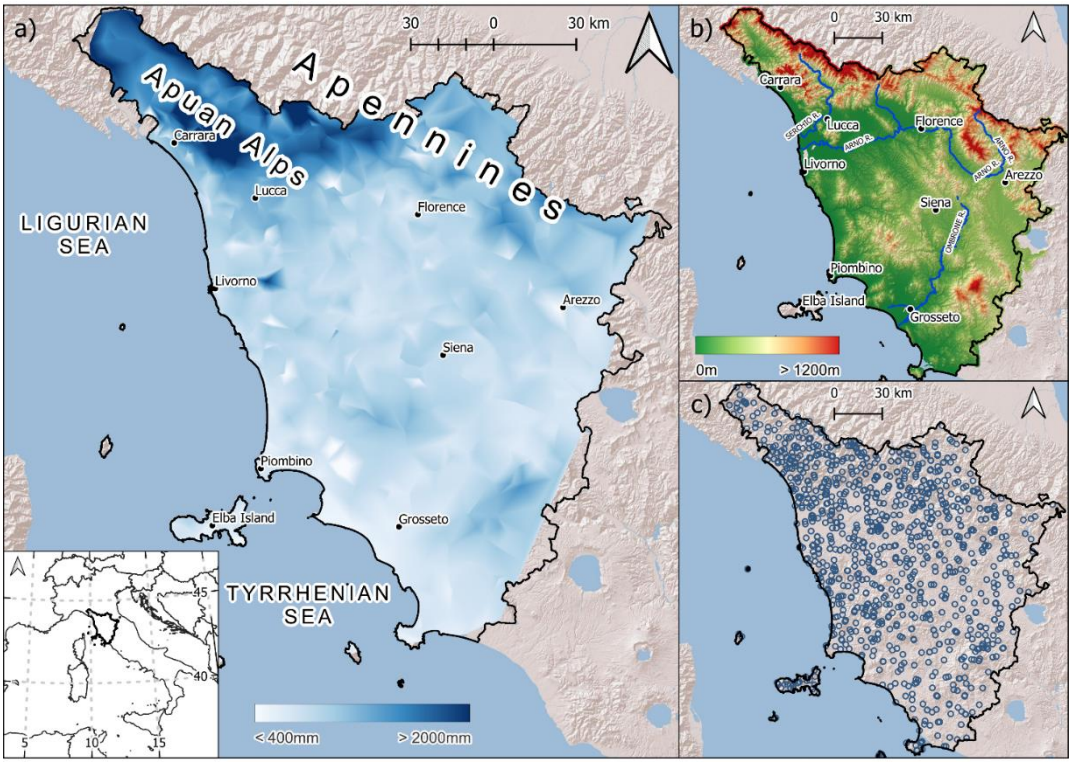

Figure 2.1. a) mean annual precipitation (MAP) of Tuscany linked to the morphology: the rainiest areas correspond to the mountainous areas; b) morphology of Tuscany; c) the 1103 raingauges of the Tuscany Region Hydrologic Service network.

2.2 Material and Methods

2.2.1 Long-term rainfall trends and climatology relation

2.2.1.1 Daily rainfall dataset and processing

The raingauge dataset was provided by the Tuscany Region Hydrologic Service (SIR; https://www.sir.toscana.it/) network and includes 1103 raingauges (Figure 2.1c). The dataset is the best one available in this area and is managed by the SIR which validates and checks the data. The activity period of each raingauge is variable. The older stations have been monitoring since the beginning of the last century, even if a temporal continuity of the data is not always guaranteed for some stations. SIR provides the daily rainfall data for each raingauge in the operation period. To obtain longer and more complete time series from this dataset, we grouped the stations according to a stringent procedure. This step is necessary to reconstruct the time series of the stations that have experienced minor changes in position or that have undergone an administrative variation (e.g., a slight change in name or identification code). The stations have consecutive intermittent activity times due to the decommissioning of one and the subsequent installation of a new one. In these cases, we merged the stations by assigning the same, or part of the same name, with a difference in altimetry less than 20% of the measurement, and a maximum distance less than 2 km. The geographic coordinates of the merged stations derived from a cartesian mean of the original coordinates of the origin stations.

By using the data available and following the procedure described above, a total of 117 time series were obtained from 1950 to 2020. The rainfall data can also be useful for comparison with the results of the linear models which predict rainfall anomalies. The rainfall values are expressed as percentage anomalies of rainfall (PAR), and are calculated as follows:

$$PAR_{s,i} = \frac{x_{s,i} - \overline{x_l}}{\overline{x_l}} \cdot 100 \quad (1)$$

where, $x_{s,i}$ is the annual seasonal rainfall amount of the i-th year and s-th season, $\overline{x_l}$ is the annual rainfall amount mean of the period 1961-1990.

The values of PAR are calculated for the four seasons: winter (DJF); spring (MAM); summer (JJA); autumn (SON). Mean Average PAR (MAPAR) is a ten-year mobile average of PAR calculated for each season, and

the values are associated with the central year. We chose to use a ten-year mobile average because this time range is within the standard 10–30 year time scale considered to be decadal variability (Meehl et al., 2009).

2.2.1.2 Climatic Dataset

The NAO dataset is provided by the Climate Analysis Section of the US National Center for Atmospheric Research (NCAR). This dataset is based on the principal (PC)-based index components of the NAO, which are the time series of the leading Empirical Orthogonal Function (EOF) of SLP anomalies over the Atlantic sector, 20°-80°N, 90°W-40°E. This index is used to measure the yearly NAO, by tracking the seasonal movements of the Icelandic Low and Azores High. The dataset has a monthly frequency from January 1889 to December 2020. PC-based indices are more optimal representations of the full spatial patterns of the NAO (National Center for Atmospheric Research Staff (Eds), 2021).

The EA dataset used in this study is provided by the National Weather Service of NOAA. The frequency of the dataset is on a monthly basis, from 1950 to 2020. The index is standardized by 1981-2010 climatology (Climate Prediction Center, 2021).

The WeMO index is provided by the Climatic Research Unit (CRU) of the University of East Anglia (Climatic Research Unit, 2021). The time series started in 1821 and has a monthly frequency.

The trends of NASST, MSST, and GGSST are calculated from the Extended Reconstructed Sea Surface Temperature (ERSST) dataset version 5 (NOAA, 2021), and they are expressed using a 10-year mobile window of anomalies. The anomalies are referred to the mean of the 1961-1990 period. NASST is calculated in the area 0N-65N 80W-0E; MSST in the area 38N-49N 0E-28E; and GGSST in the area 42.8N-44.8N 7.6E-10.76E.

2.2.1.3 Statistical Correlation and Linear Models

. We investigated the link between the different indices by using traditional statistical methods (Spearman, 1904), but also introducing an innovative approach in this field, which employs a linear model to understand the influence of each index on the rainfall prediction. The combination of these different methods helped us to comprehend the accuracy and the advantages of the new method proposed.

We calculated the correlation coefficient to identify a possible relationship between atmospheric teleconnection and rainfall amount. Several authors use a statistical method of correlation to quantify the relationship between atmospheric indices and rainfalls (Brandimarte et al., 2011; Faust et al., 2016;

Kalimeris et al., 2017; Kotsias et al., 2020; Koyama and Stroeve, 2019; López-Moreno et al., 2011; Vicente-Serrano and López-Moreno, 2008). In particular, some authors (Caloiero et al., 2011; Izquierdo et al., 2014; Luppichini et al., 2021; Nalley et al., 2019; Vergni et al., 2016) use Spearman's correlation coefficient (SCC) (Spearman, 1904) to understand the relationship between atmospheric index and rainfall amount. This relationship is suitable for monotonically-related variables, even when their relationship is not linear. The range of Spearman's coefficients is between -1 and 1; positive values indicate a tendency of one variable to increase or decrease together with another variable, whereas negative values indicate a trend in which the increase in the values of one variable is associated with the decrease in the values of the other variable, and vice versa. We have divided the time series into four seasons: winter from December to February (DJF), spring from March to May (MAM), summer from June to August (JJA) and autumn from September to November (SON). We calculated the SCC among the three atmospheric teleconnections and the rainfall for the four seasons using a 10-year moving time window from 1950 to 2020. We assigned the correlation result to the year halfway through each ten-years.

We can create linear models capable of predicting the rainfall amount by using the NAO, WeMO and EA time series. The equation of a linear model predicting the rainfall (R_p), is the following:

$$R_p = \alpha NAO + \beta WeMO + \gamma EA + \delta \quad (2)$$

We can analyse the best estimates of the model parameters (α, β, γ) to understand the role of each input in the prediction of rainfall. If we want to obtain the best prediction models, we should use models that are more complex than a simple linear model. However, the simplicity of the linear models allows to analyse the influence of the inputs, since one of the tasks of this work is to show that more complex models (for instance with the inclusion of synergies between the input data) are not necessary to explain the rainfall observed. We therefore created a linear model for each raingauge time series for each season. The different range of the three atmospheric teleconnections could influence the information expressed by the parameters of models α, β and δ. For this reason, we scaled the time series of NAO, WeMO and EA in the range between 0 and 1 for the studied period (1950-2020), by applying the following equation:

$$T = \frac{Ts - Ts_m}{Ts_{\mathrm{M}} - Ts_m} \quad (3)$$

where T is the index time series in the 0-1 range, Ts_{M} is the maximum value of the index, and Ts_m is the minimum value of the index. We fitted a linear model for each time series, using the SciPy library in Python Language and, in more detail, the "curve_fit" method (Virtanen et al., 2020). We validated the fits calculating the Root Mean Square Error (*RMSE*) and the Correlation Coefficient (*r*) as follows:

$$RMSE = \left(\frac{1}{N}\sum_{i=0}^{N}(F_i - V_i)^2\right)^{0.5} \tag{4}$$

$$r = \frac{\left(\frac{1}{N}\sum_{i=0}^{N}(F_i * V_i)\right)}{\left(\frac{1}{N}\sum_{i=0}^{N}F_i^2\right)^{0.5} \cdot \left(\frac{1}{N}\sum_{i=0}^{N}V_i^2\right)^{0.5}} \tag{5}$$

where F_i are the forecast values, V_i are the observed values and N the number of years.

2.2.2 Influence of the temperature on rainfall distribution

2.2.2.1 Rainfall and temperature dataset and preprocessing

For this part of the work, the rainfall and temperature datasets were provided by SIR and they have a frequency of 15 minutes. From these datasets, we extracted the rainfall time series with length longer than 10 years and a number of missing values less than 10%. For each rainfall time series, we associated the temperature time series of the nearest station, in a maximum range of 25 km, and with a maximum data loss of 10% referring only to the data with rain values higher than 0.1 mm. This represents a compromise between data completeness and the extensiveness of the dataset. After this procedure, we selected 198 rainfall time series distributed on the study area (Figure 2.2).

The rainfall and temperature datasets were then aggregated to 0.25h, 0.5h, 1h, 3h, 6h and 24h (hereafter called $P_{0.25}$, $P_{0.5}$, P_1, P_3, P_6 and P_{24}) for each station and subdivided into three seasonal sub-samples: 1) Annual Period (data from the entire year, from January to December); 2) Wet Season (data from October to March); 3) Dry Season (data from April to September). For the following elaborations, we selected the only records with rain values higher than 0.1 mm.

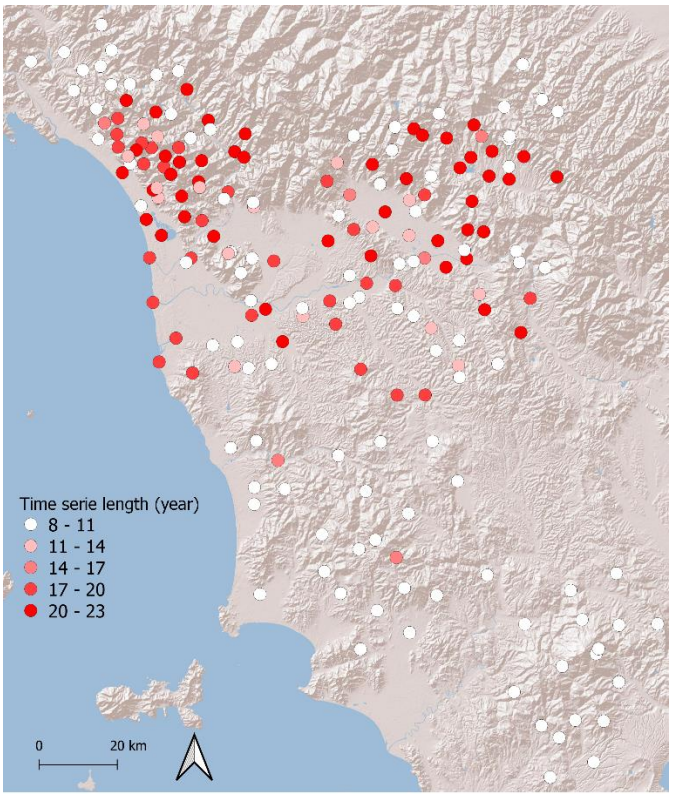

Figure 2.2 Spatial distribution and length of the time series of the 198 selected stations.

2.2.2.2 Quantile regression and CC-like scaling

The relationship between rainfall and temperature was here evaluated by using a quantile regression as suggested by (Visser et al., 2021; Wasko and Sharma, 2014) improving the method propose by (Hardwick Jones et al., 2010). Quantile regression is calculated by the Python package "statsmodels" (Seabold and Perktold, 2010), with the scaling of peak rainfall intensity (P) with temperature (T) calculated as follows:

$$\log(P) = \beta_0^q + \beta_1^q T \tag{6}$$

where q is the selected quantile, β_0 and β_1 are fitted parameters. The scaling (α) of rainfall intensity with temperature as a percentage was calculated through an exponential transformation of the slope of the fitted quantile regression relationship:

$$P = e^{\beta_0^q} \left(e^{\beta_1^q}\right)^T \tag{7}$$

$$P = e^{\beta_0^q} (1 + \alpha)^T \tag{8}$$

$$\alpha = e^{\beta_1^q} - 1 \tag{9}$$

such that $\alpha = 0.07$ is equivalent to CC-like scaling of 7%/°C. The quantile regression was applied for the 0.5, 0.75, 0.95 and 0.99 quantiles.

2.2.2.3 Temperature anomalies during EPEs

For each time series, we identified the EPEs as the rainfall events with a probability lower than 95th to occur. For the three investigated seasons, for each time series, and for each rainfall accumulation period, we calculated the mean temperature ($\bar{T}$) and the temperature anomaly of the i-th event (TA_i) as the difference between the mean temperature and the temperature occurred during the EPE (T_i) as following:

$$TA_i = T_i - \bar{T} \tag{10}$$

2.3 Results

2.3.1 Rainfall Trends

Figure 2.3 reports the values of PAR calculated for each time series used in this work, and obtained from equation 1. The graphs indicate a small variability of PAR between each time series, excluding the possibility of different influences on the linear model outcomes by the input stations and a significant variability in the study area. The MAPAR of the study area is shown in Figures 2.4 – 2.7 for the four seasons. These variations of MAPAR over time are different in the four seasons. From 1950 to 1985, the DJF season was characterized by a slow rainfall reduction followed by a sudden decrease around the 90's. The first years of the 1990's presented a MAPAR reduction of 40%. Starting from 2000, the DJF MAPAR increased progressively until reaching the amount recorded before 1990 (Figure 2.4). Until the 1990s, the MAM MAPAR was characterized by an oscillation, from the 1990's to the 2010's, MAM MAPAR has the minimum values which are in the range between -10 and -20%. MAM MAPAR increased after 2008 (Figure 2.5). The JJA MAPAR started to decrease in 1965 with minimum values of -30% around 2005. The last years were marked by a weakly increase of JJA MAPAR (Figure 2.6). SON MAPAR had a certain variability over an approximate 20-year period. The maximum SON MAPAR amount was recorded around 1965 and 1995, while the minimum values were those of the period 1970-1990 (Figure 2.7).

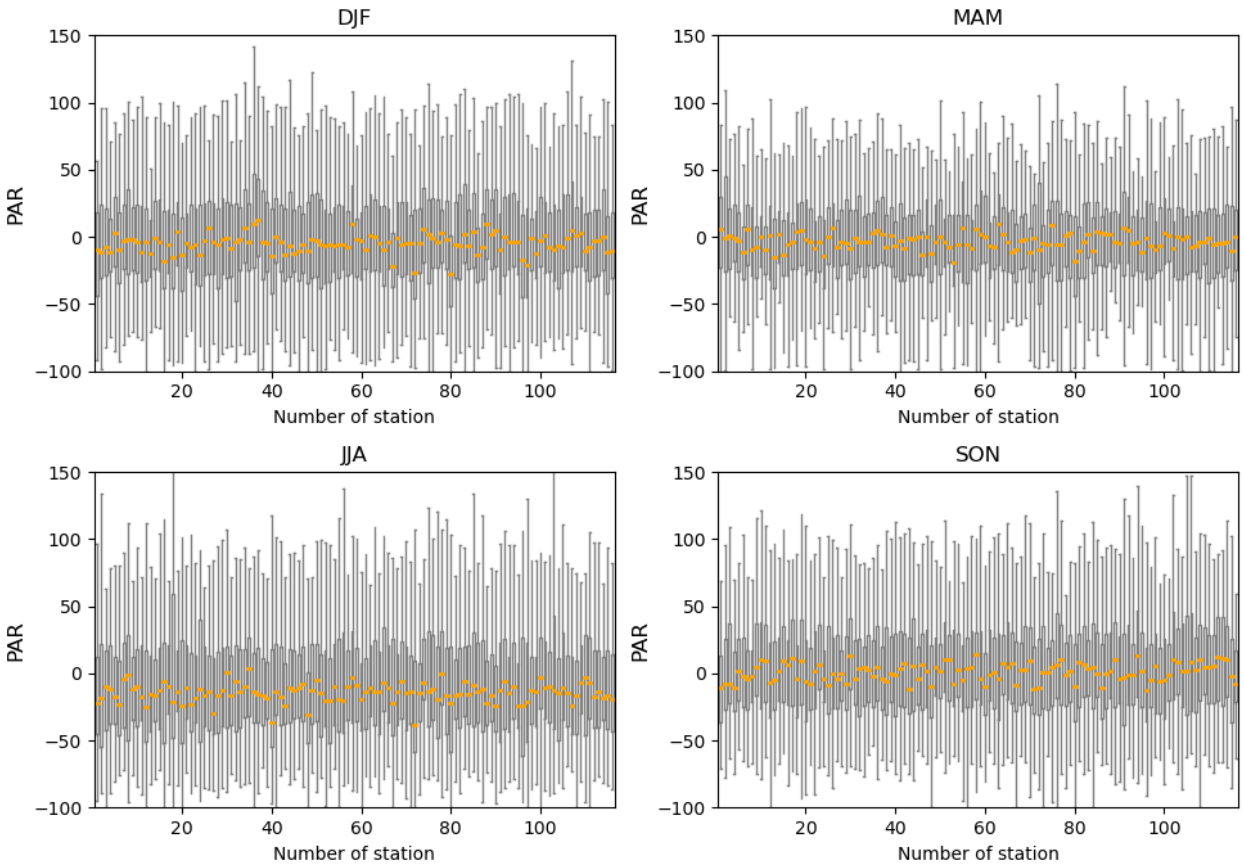

Figure 2.3. For the four seasons, Percentage Anomaly of Rainfall (PAR) of the 117 rainfall time series used in this work. Each boxplot is referred to a rainfall time series and represents the distribution of rainfall anomaly values in relation to the annual rainfall amount of the 1961-1990 period, in agreement with the equation 1 in the text. The boxes represent the interval between the 25th and 75th percentiles (Q1 and Q3). IQR is the interquartile range Q3-Q1. The upper whisker extends to the last datum lower than Q3 + 1.5×IQR. Similarly, the lower whisker reaches the first datum higher than Q1 – 1.5×IQR. The orange lines represent the medians (DJF: December-January-February; MAM: March-April-May; JJA: June-July-August; SON: September-October-November (after Luppichini et al., 2022b, modified).

2.3.2 Atmospheric Teleconnection Trends

In DJF, NAO shows by an intensification of the positive phase, the EA time series was shows an intensification of the positive phase starting from 1985 (Figure 2.4), and WeMO is characterized by a positive phase with a decrease in the 1990-2010 period.

In MAM, NAO and EA time series present a progressive increase with an intensification of the positive phase; WeMO experiences a progressive decrease from a positive phase to a negative persistence phase since 2005 (Figure 2.5).

In JJA, NAO is characterized by a positive phase until 2005, whereas the index shows a negative phase, except for some years. In this season, EA startes to increase progressively in 1995, while WeMO has a progressive decrease with a persistence positive phase since 2005 (Figure 2.6).

In SON, NAO is variable with periods characterized by negative alternated with positive phases. In this season, EA has a higher index fluctuation, with a negative phase until 1980, followed by a more positive ten-year phase and then by a negative phase until 2000. From 2000 to 2020, EA increases reaching its maximum values. WeMO shows two distinct positive phases around 1975 and 1995, but the overall trend decreases with a negative phase since 2005 (Figure 2.7).

2.3.3 Sea surface temperature trends

The variations of NASST, MSST and GGSST started to display a clear increasing trend in the 1980's in all seasons. Such increase only started around the 2010's for DJF and GGSST, while it started to increase in the 1980s in the other seasons. The increase in SST was greater in summer than in other seasons (Figures 2.4 – 2.7).

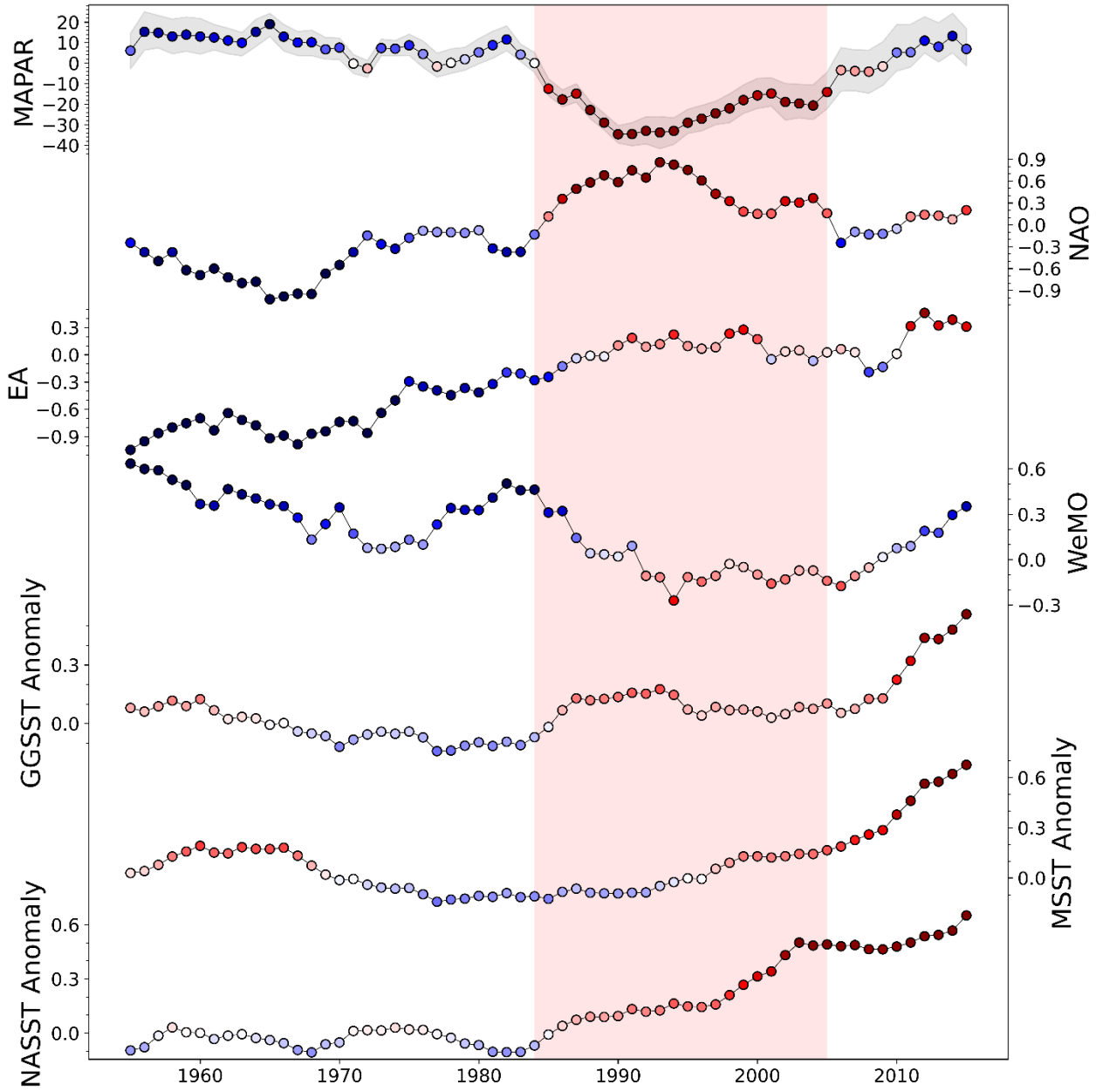

Figure 2.4. DJF season, trends of Mobile Average Percentage Anomaly Rainfall (MAPAR), NAO, WeMO, EA, North Atlantic Sea Surface Temperature (NASST), Mediterranean Sea Surface Temperature (MSST), and Genoa Gulf Sea Surface Temperature (GGSST). The colour of the points varies between blue (wet periods) and red (dry periods). The grey band on MAPAR represents the 25th and 75th percentile, the dots represent the mean value. The pink band is referred to the main dry period of the time series (after by Luppichini et al., 2022b, modified).

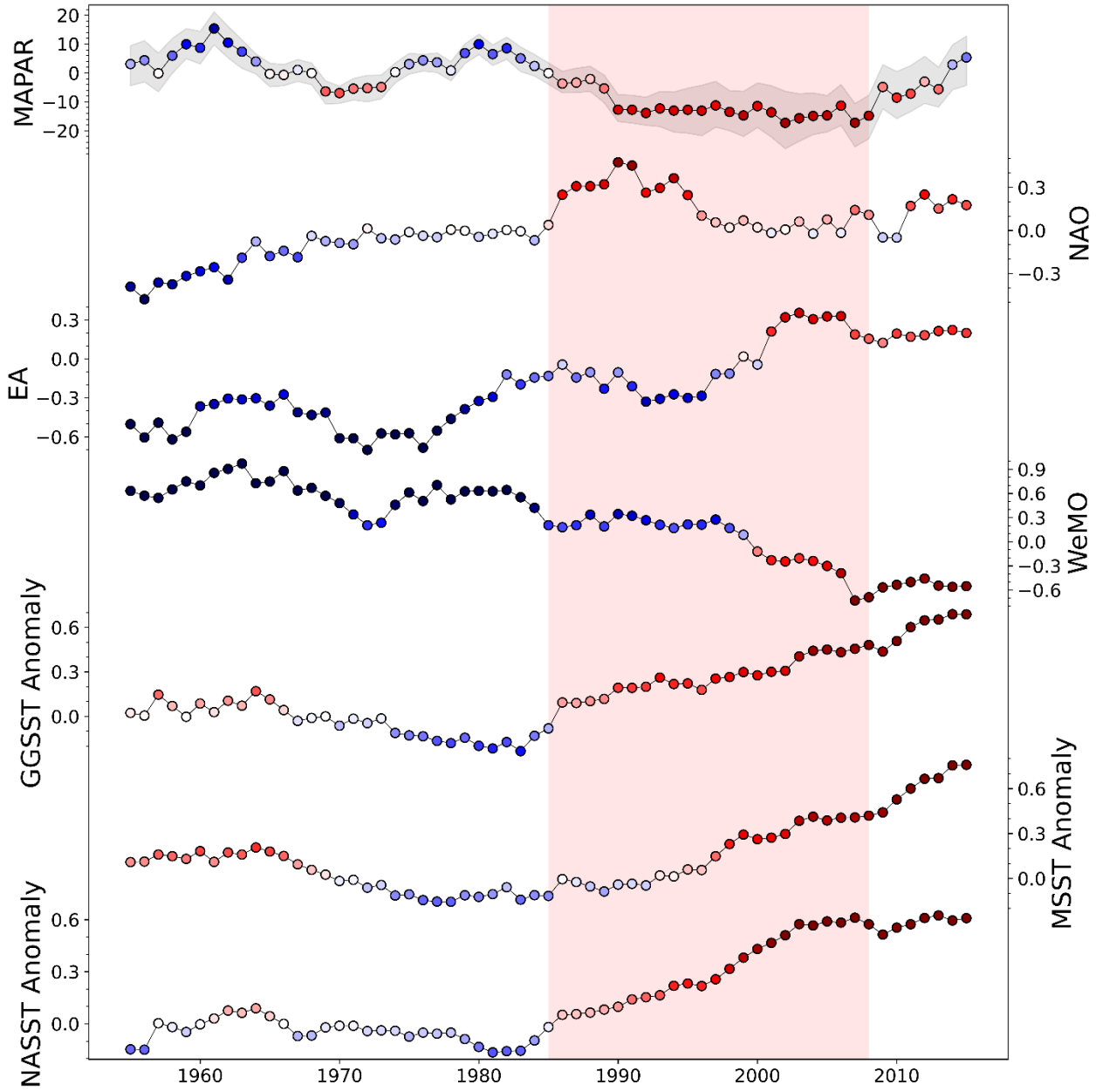

Figure 2.5. MAM season, trends of Mobile Average Percentage Anomaly Rainfall (MAPAR), NAO, WeMO, EA, North Atlantic Sea Surface Temperature (NASST), Mediterranean Sea Surface Temperature (MSST), and Genoa Gulf Sea Surface Temperature (GGSST) for the MAM season. The colour of the points varies between blue (wet periods) and red (dry periods). The grey band on MAPAR represents the 25th and 75th percentile, the dots represent the mean value. The pink band is referred to the main dry period of the time series (after by Luppichini et al., 2022b, modified).Fare clic o toccare qui per immettere il testo.

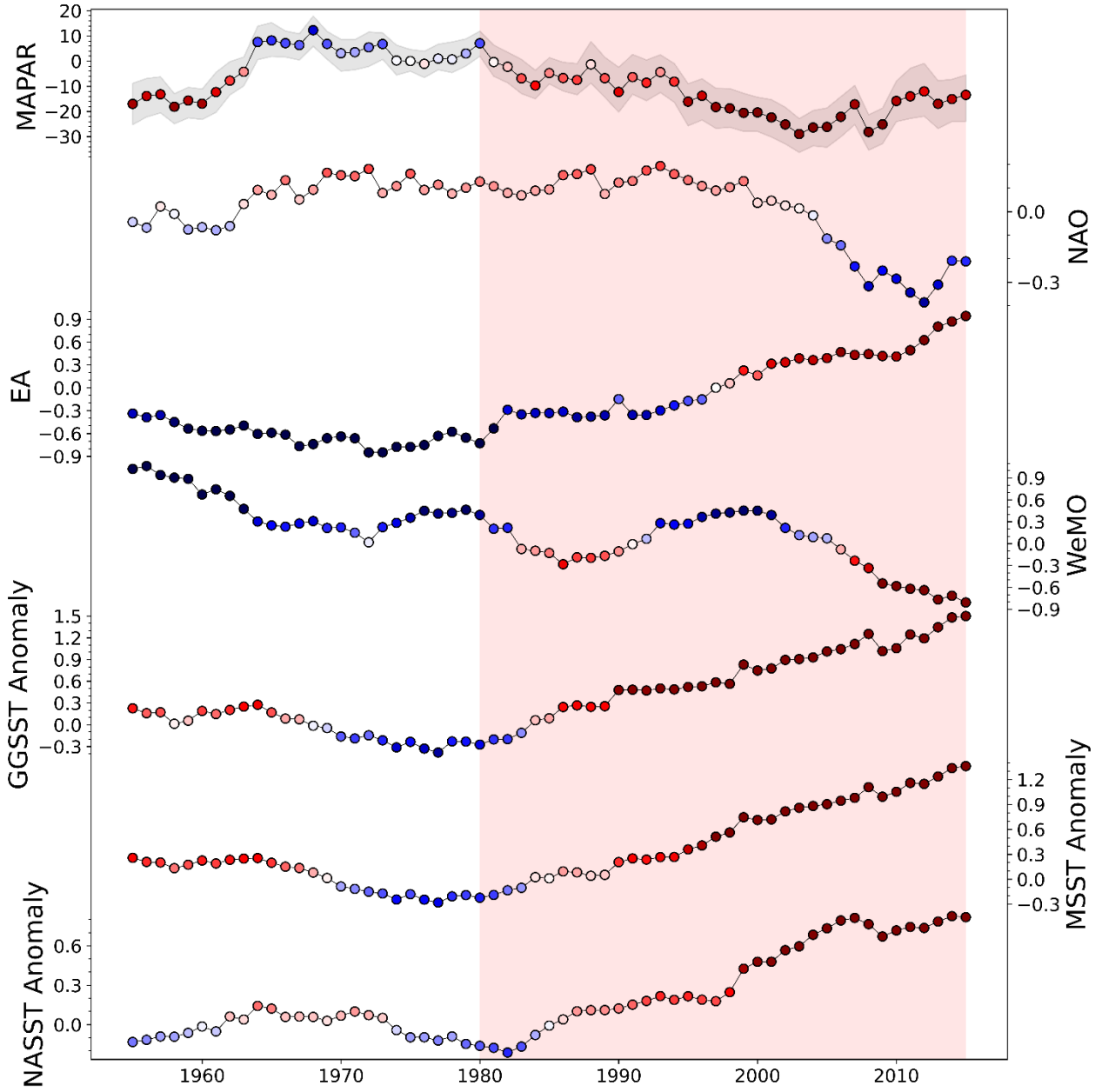

Figure 2.6. JJA, trends of Mobile Average Percentage Anomaly Rainfall (MAPAR), NAO, WeMO, EA, North Atlantic Sea Surface Temperature (NASST), Mediterranean Sea Surface Temperature (MSST), and Genoa Gulf Sea Surface Temperature (GGSST). The colour of the points varies between blue (wet periods) and red (dry periods). The grey band on MAPAR represents the 25th and 75th percentile, the dots represent the mean value. The pink band is referred to the main dry period of the time series (after by Luppichini et al., 2022b, modified).Fare clic o toccare qui per immettere il testo.

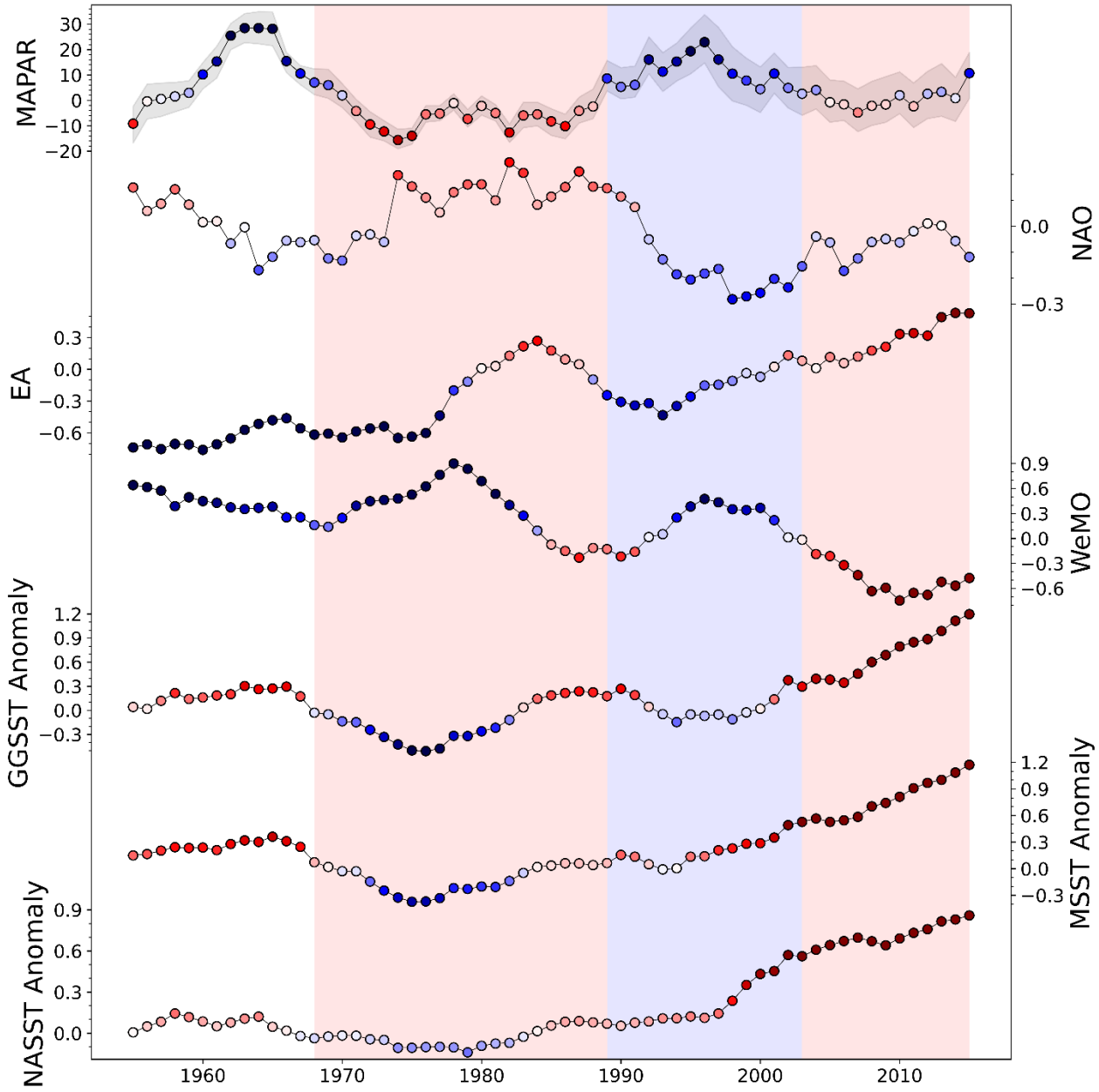

Figure 2.7 SON season, trends of Mobile Average Percentage Anomaly Rainfall (MAPAR), NAO, WeMO, EA, North Atlantic Sea Surface Temperature (NASST), Mediterranean Sea Surface Temperature (MSST), and Genoa Gulf Sea Surface Temperature (GGSST). The colour of the points varies between blue (wet periods) and red (dry periods). The grey band on MAPAR represents the 25th and 75th percentile, the dots represent the mean value. The pink band is referred to the main dry period of the time series (after by Luppichini et al., 2022b, modified).Fare clic o toccare qui per immettere il testo.

2.3.4 Statistical Correlation

Figure 2.8 and 2.9 report the results obtained and the spatial distribution of the p-values obtained, respectively. In the DJF season, rainfall is correlated with WeMO and anticorrelated with NAO and EA. Rainfall increases during a negative phase of NAO or EA and a positive phase of WeMO. During this period,

each atmospheric teleconnection has a similar effect on the rainfall amount. In the MAM season, the strongest correlation is with WeMO, and even in this case a positive phase of the index corresponds to a rainfall increase in the study area. NAO and EA are weakly anticorrelated with the rainfall amount. The strongest correlation is with EA in the JJA season, and a negative phase of this index indicates an increase in rainfall in the area, while a positive phase of EA corresponds to reduced precipitation in summer. NAO and WeMO are weakly correlated with rainfall, but do not show a clear behaviour. Even in the SON season, the strongest correlation is with EA. The correlation in this season is positive, which indicates that a positive EA phase determines increased precipitation in the area. The spatial correlation distribution is homogenous with no clear spatial pattern, especially when the correlations are strong, providing a precise indication of the relationship (Figure 2.8).

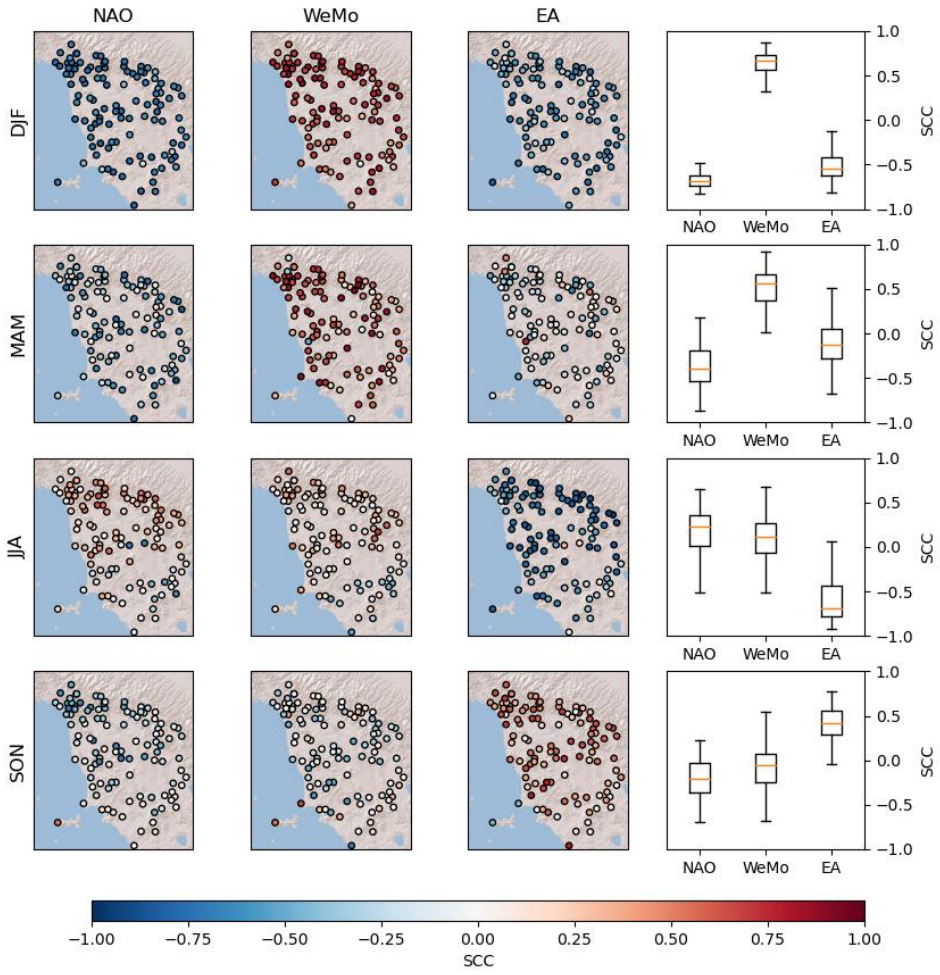

Figure 2.8. Spearman's correlation coefficients (SCC) between season rainfall and climatic patterns. For each season, we report the correlation with NAO, EA and WeMO and the relative boxplots. The boxes represent the interval between the 25th and 75th percentiles (Q1 and Q3). IQR is the interquartile range Q3-Q1. The upper whisker extend to the last datum lower than Q3 + 1.5×IQR. Similarly, the lower whisker reach the first datum higher than Q1 – 1.5×IQR. The orange lines represent the medians (after Luppichini et al., 2022b, modified).

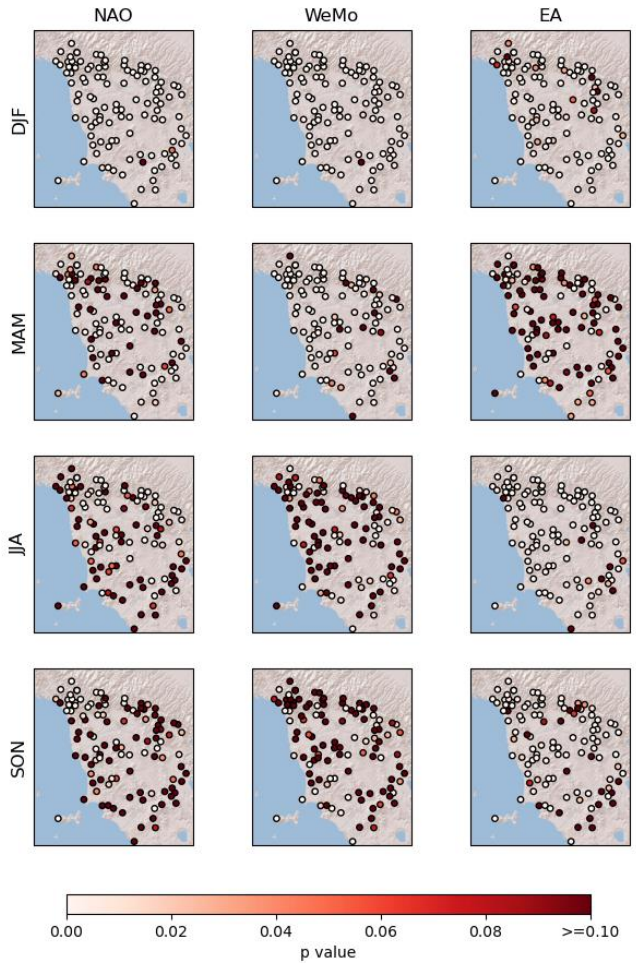

Figure 2.9. P-values of Spearman's correlation coefficients (SCC; after Luppichini et al., 2022b, modified).

2.3.5 Linear Models

Figure 2.10a-d show four examples of the MAPAR prediction by means of linear models referred to the DJF, MAM, JJA and SON periods. Indeed, they have RMSE values similar to the error medians calculated on the entire dataset (Figure 2.10e). For the case shown in Figure 9a, α, β and γ are respectively -96.56, 42.53, and 4.85; for the case reported in Figure 9b they are -21.39, -15.54 and -15.76; for the case reported in Figure 9c they are -30.71, -56.10 and -1.34; for the case reported in Figure 9c they are -48.05, 7.54 and 6.71. Figure 2.10e and 9d also report the RMSE and r of the entire dataset. SON, followed by MAM, which is the season with the highest average errors.

Figure 2.11 shows the mean values of coefficients α, β and γ for the linear models in each season (blue circles). We can observe a change in the values of the three coefficients from one season to another; the red circles show the relative weights of each coefficient. In DJF season, the coefficient with the greatest weight

is α with a mean value of about 55%, followed by β and γ. The coefficients indicate that NAO has more influence on the rainfall trend than WeMO and EA in DJF. In this season, the coefficient values indicate that an increase in rainfall is linked to a negative phase of NAO (α is negative) and a positive phase of WeMO (β is positive). In MAM season, β (WeMO) has the highest weight in the results of the models, followed by α (NAO) and γ (EA). Therefore, the coefficients denote that the amount of rainfall is correlated with a positive phase of WeMO and with a negative phase of NAO. Also in this season, EA has less influence on the model than the other two indices. In JJA season EA is the index with the greatest coefficient (γ). In particular, the coefficients suggest that the summer rainfall is linked to a negative phase of EA. Less important, the coefficients indicate that the summer rainfall is linked to a negative phase of WeMO. In SON season, NAO has the greatest weight and is followed by WeMO and EA, which have less influence on the rainfall trend. In this case, the coefficients are all negative, so that rainfall is correlated to a negative phase of these indices.

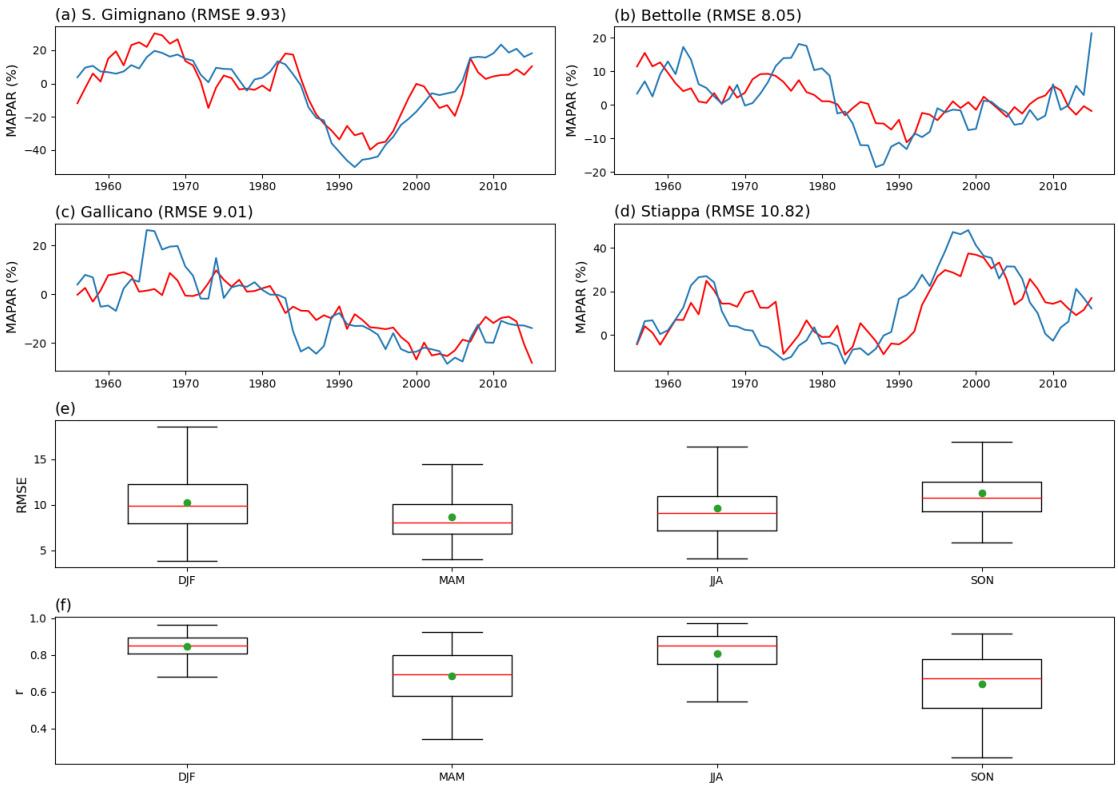

Figure 2.10. a-d) Four examples of observed MAPAR (blue line) and predicted MAPAR (red line) respectively for the seasons DJF, MAM, JJA and SON. e) the boxplots represent the Root Mean Square Error (RMSE) of the linear models for the four seasons. f) the boxplots represent the Correlation Coefficient (r) of the linear models for the four seasons. The boxes represent the interval between the 25th and 75th percentiles (Q1 and Q3). IQR is the interquartile range Q3-Q1. The upper whisker extends to the last datum lower than Q3 + 1.5×IQR. Similarly, the lower whisker reaches the first datum higher than Q1 – 1.5×IQR. The red lines represent the medians, while the green circle represent the means (after Luppichini et al., 2022b, modified).

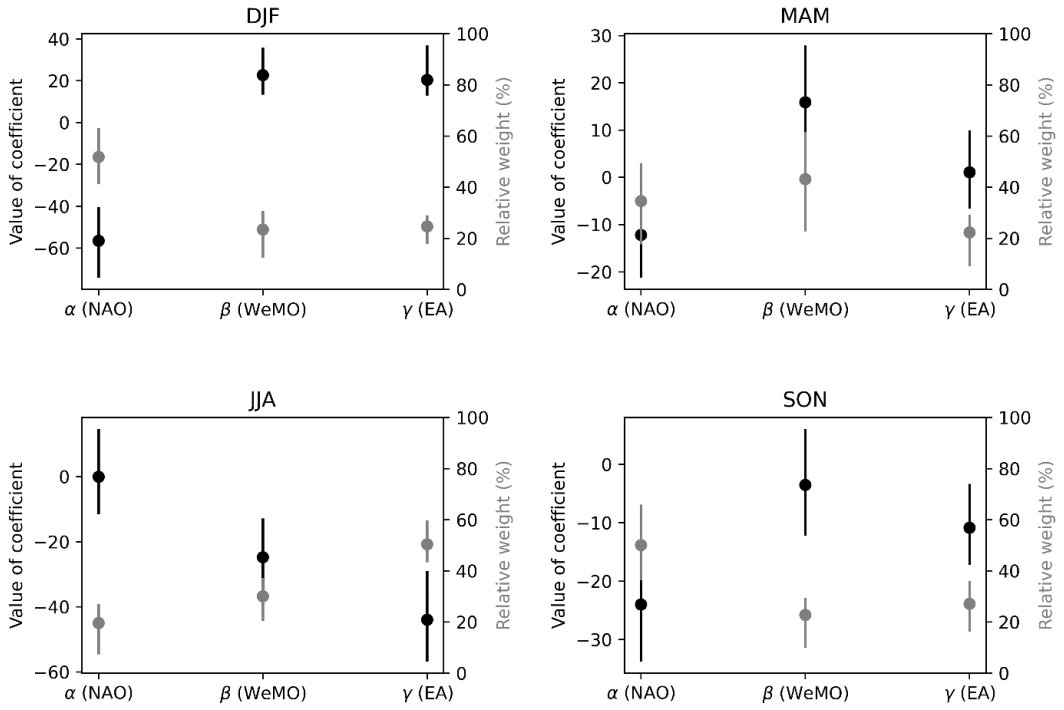

Figure 2.11. Setting of the linear model coefficients used to analyze the relationship between climate patterns and rainfall. The balck circle is the mean absolute value of the coefficient, whereas the grey circle represents the mean relative weight of the coefficient on the prediction. The results are reported for each season. The black and grey lines represent the interval between the 25th and 75th percentiles of the coefficient distributions (DJF: December-January-February; MAM: March-April-May; JJA: June-July-August; SON: September-October-November (aftet Luppichini et al., 2022b, modified).

2.3.6 Quantile regression and CC-Like scaling

The quantile regression shows a different relationship between rainfall and temperature depending by the season, quantile and rainfall accumulation period (Figure 2.12). Increasing the quantile threshold, there is a surge of the values of scaling α, while an increase of the sample rainfall accumulation period causes a reduction of the values of scaling α. In more detail, the wet season is characterized by positive scaling α values with some exceptions for the rainfall accumulation periods of 6 and 24 hours. The dry season is characterized by negative scaling α values for the lowest quantiles and for the rainfall accumulation periods of 6h and 24h. Moreover, it is characterized by positive scaling α values for the highest quantiles and rainfall accumulation periods (Figure 2.12). In summary, the lowest scaling α values are recorded in dry season for the 0.5 quantile and for the P_{24}, while the highest scaling α values are verified in wet season for the 0.99 quantile and for the $P_{0.25}$ (Figure 2.12).

Analyzing the spatial distribution of the scaling α values, we cannot identify geographical forcing that can influence the spatiality of the results. For this reason, the study area seems to have a homogenous behavior, as reported in the example images of Figure 2.13 and Figure 2.14.

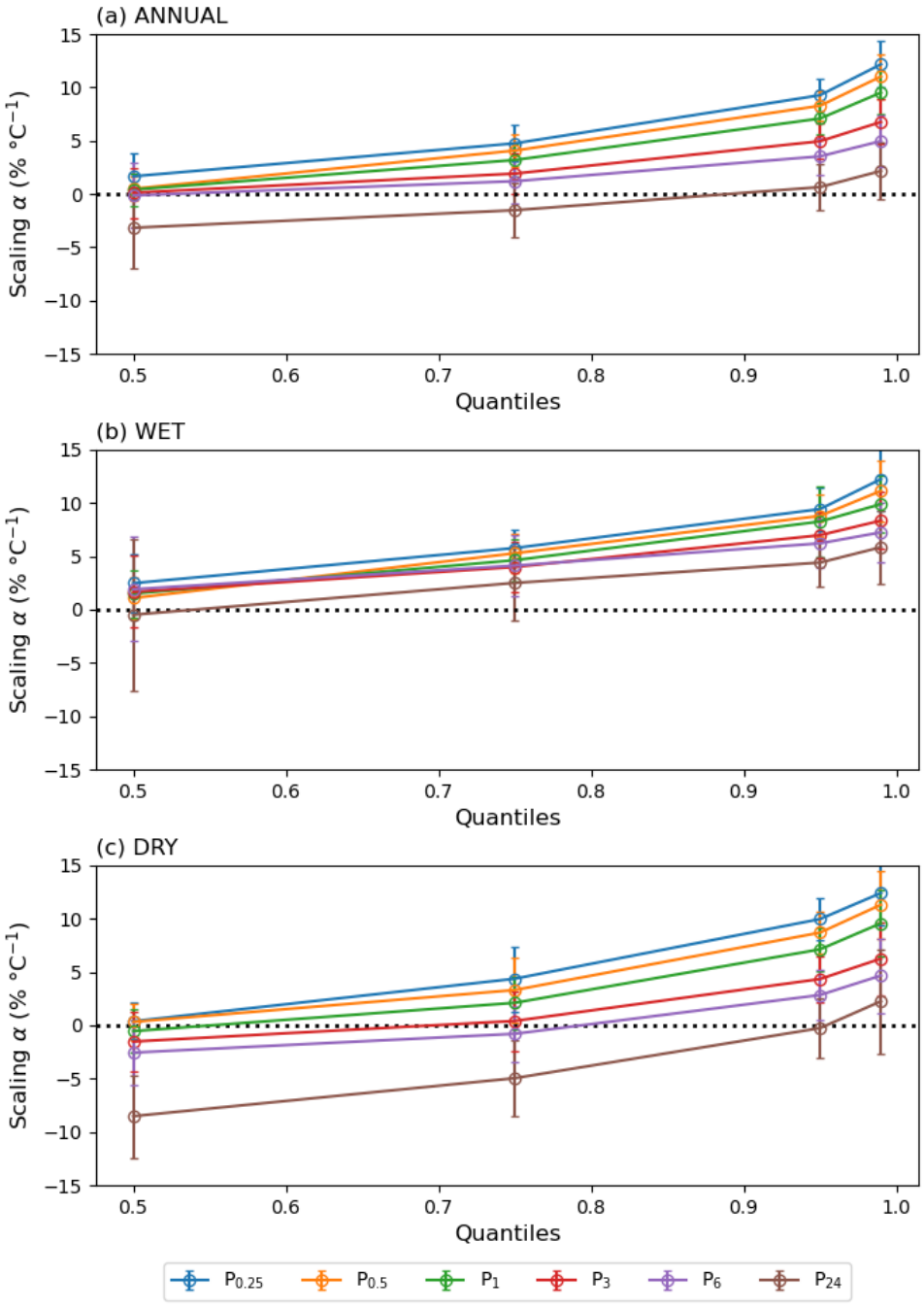

Figure 2.12 The Clausius-Clapeyron (CC) relation (scaling α) calculated with the quantile regression for the seasosn: a) annual; b) wet; c) dry. The error bars are the standard deviation. $P_{0.25}$, $P_{0.5}$, P_1, P_3, P_6 and P_{24} reffere to rain accumulation periods from 15 minutes to 24 hours.

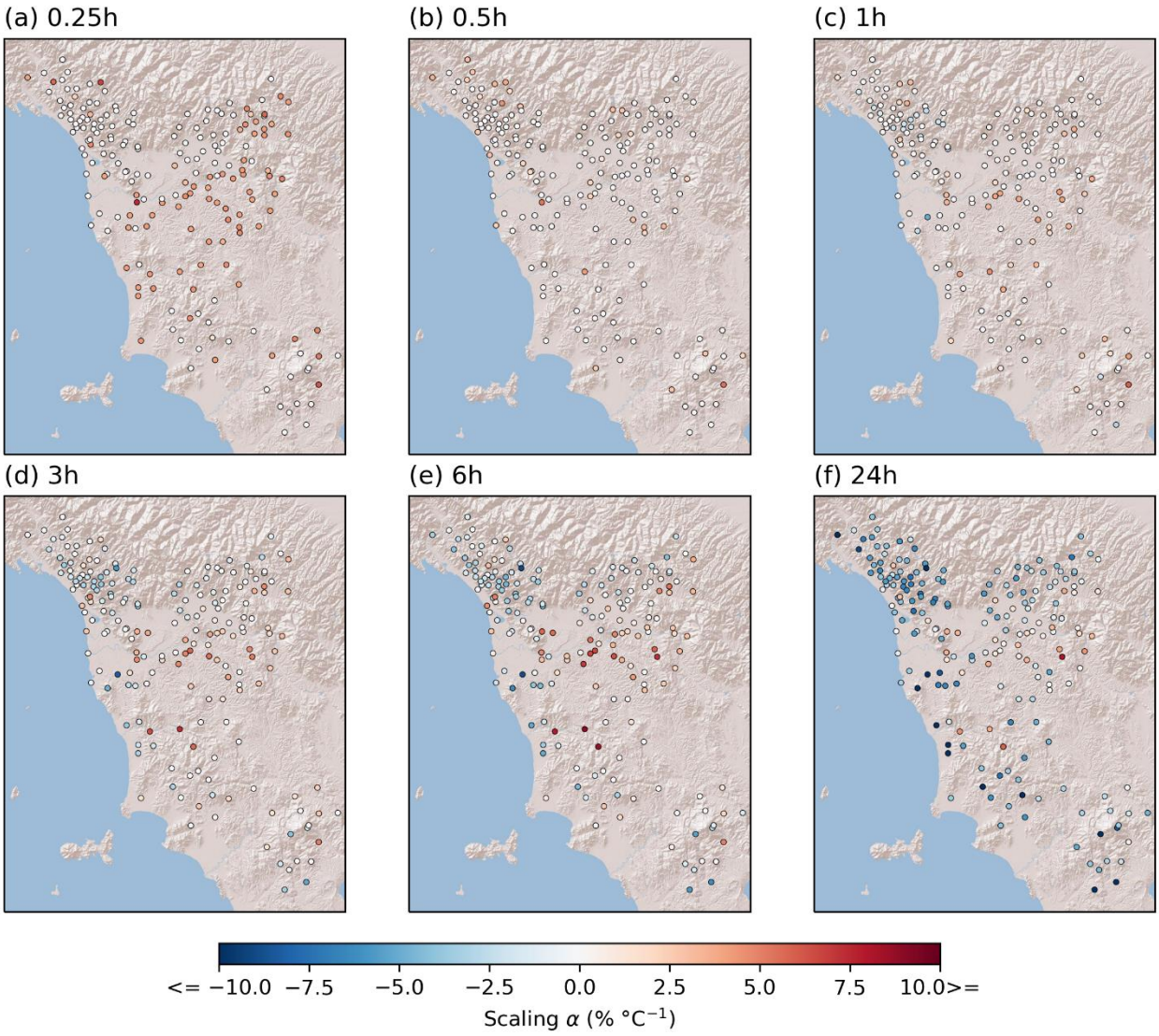

Figure 2.13 Spatial distribution of the Clausius-Clapeyron (CC) relation (scaling α) calculated by the quantile regression for the annual season and 0.5 quantile.

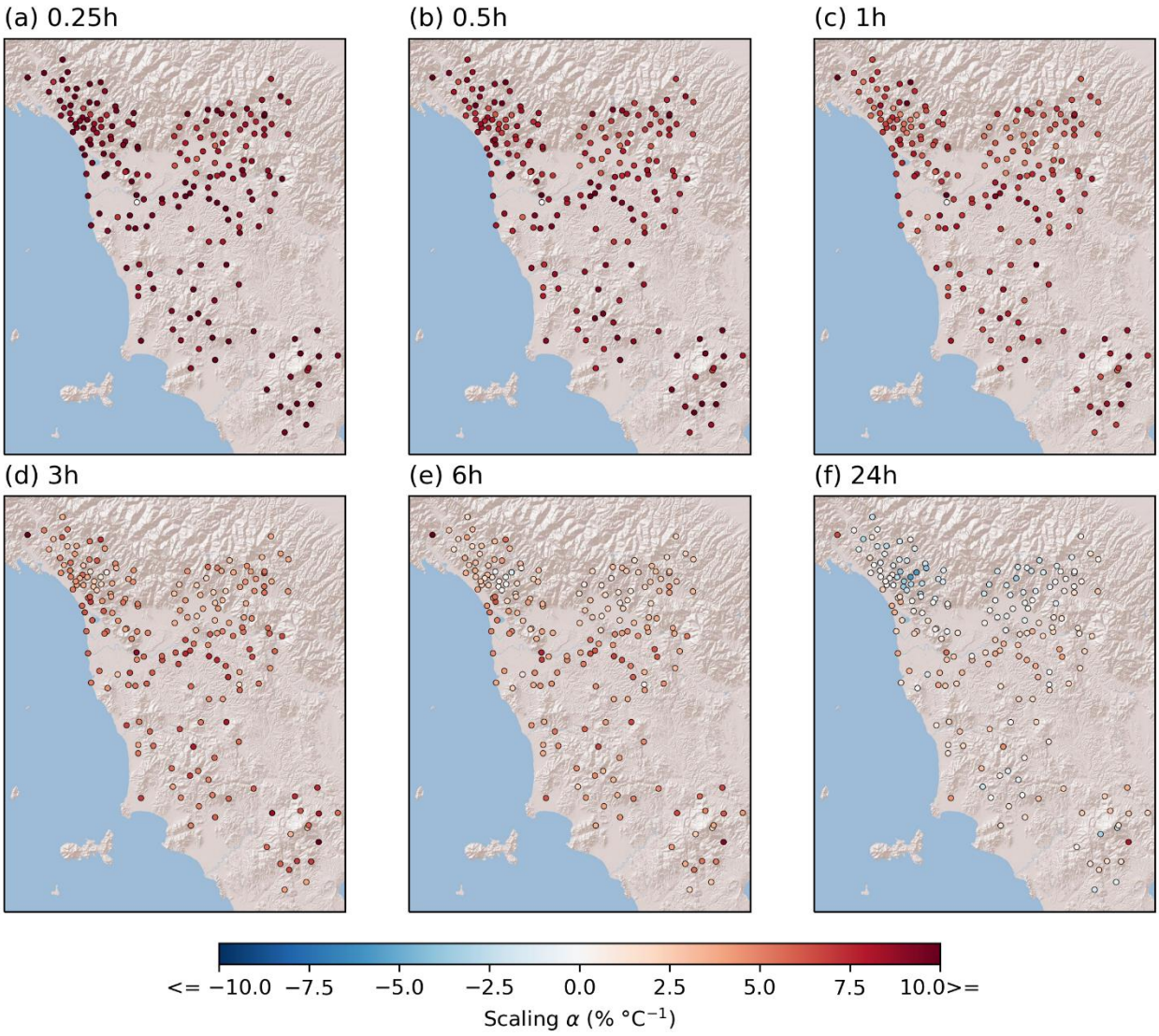

Figure 2.14 Spatial distribution of the Clausius-Clapeyron (CC) relation (scaling α) calculated with the quantile regression for the annual season and 0.95 quantile.

2.3.7 Temperature anomalies during EPEs

The analysis of the temperature anomalies occurred during the EPEs shows that there is a relationship between the temperatures and the rainfalls (Figure 2.15). The fastest EPEs (such as $P_{0.25}$) are characterized by the highest temperature anomalies with mean values also higher than 3 °C. The most lasting EPEs are instead characterized by the lowest temperature anomalies with also negative values such as in the case of P_{24} of the dry season. Wet season and dry seasons have different behaviors: the EPEs of the wet season occurred meanly during positive temperature anomalies for each rainfall accumulation period; the EPEs of the dry season are characterized by a progressive decrease of the temperature anomalies starting from $P_{0.25}$ to P_{24} where these events occurred during temperature anomalies around to 0°C (Figure 2.15).

Spatially the lower values of mean temperature anomalies are recorded in the northern and southern of the study area near the Apuan Alps and the Apennines and the Monte Amiata (Figure 2.16, Figure 2.17 and Figure 2.18).

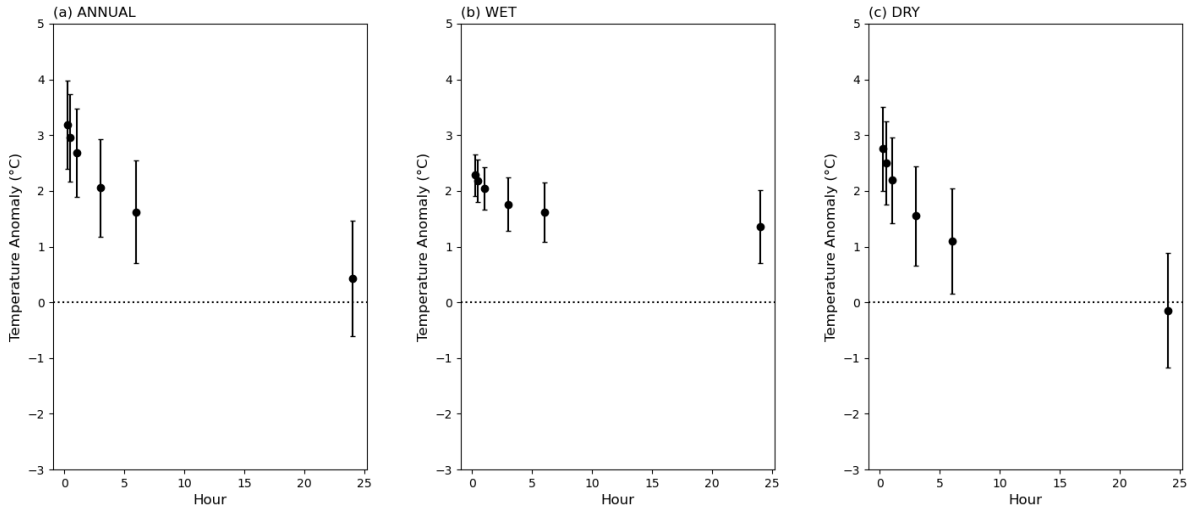

Figure 2.15 Mean temperature anomalies occurred during Extreme Precipitation Events (EPEs): a) annual; b) wet season; c) dry season. The error bars represent the standard deviation.

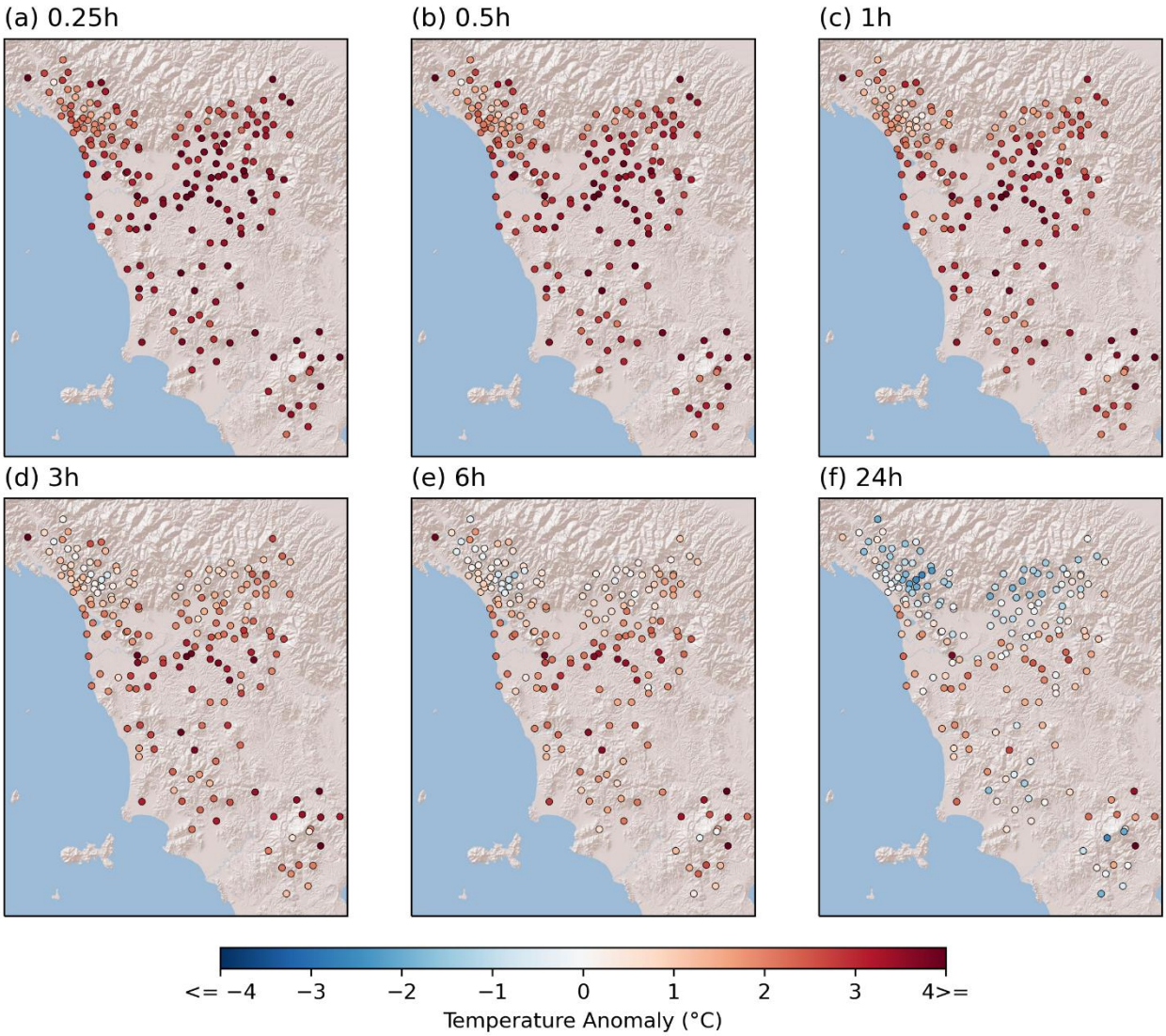

Figure 2.16 Spatial distribution of the mean temperature anomalies occurred during Extreme Precipitation Events (EPEs) for the annual period

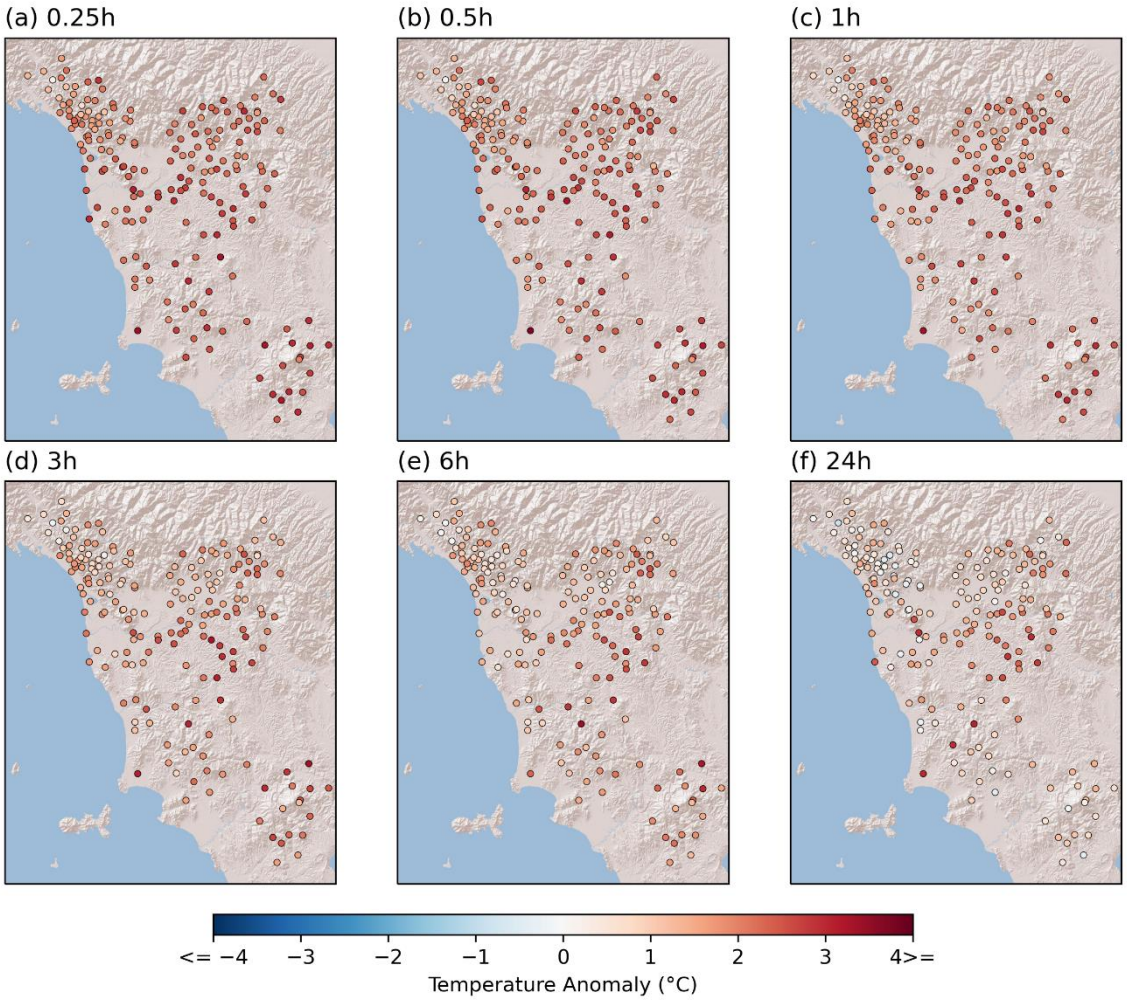

Figure 2.17 Spatial distribution of the mean temperature anomalies occurred during Extreme Precipitation Events (EPEs) for the wet season

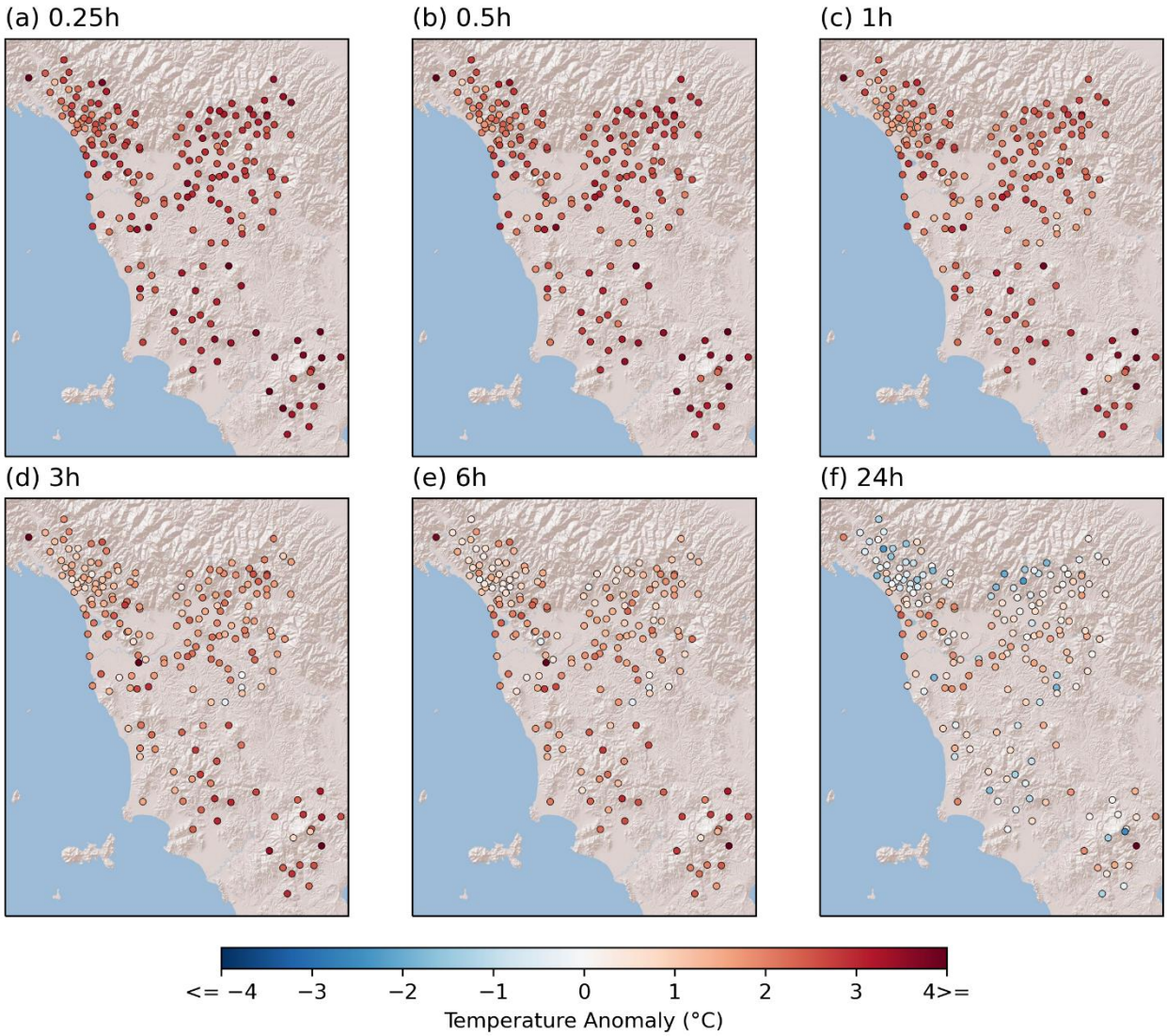

Figure 2.18 Spatial distribution of the mean temperature anomalies occurred during Extreme Precipitation Events (EPE) for the dry season

2.4 Discussion

2.4.1 Mathematical and statistical relationship between atmospheric teleconnections and rainfall

The statistical correlation calculated by Spearman's method represents a first indication of the influence of climate patterns on the local rainfall trend. In agreement with several studies (Caloiero et al., 2011; Deser et al., 2017; Ferrari et al., 2013; George et al., 2004; López-Moreno et al., 2011; Luppichini et al., 2021; Riaz et al., 2017; Vergni and Chiaudani, 2015; Vicente-Serrano and López-Moreno, 2008; West et al., 2019), NAO influence is predominant in winter, with an anticorrelation between index and rainfall amount. In agreement with the obtained SCC, an increase in the Azores High, and consequently a decrease in the

Iceland Low, determine reduced winter rainfall in the study area. The correlation between NAO and rainfall decreases during the following seasons with a minimum correlation in summer. In winter and spring, the correlation with WeMO is strong and positive. This implies the formation of the Genoa Gulf Low and its reinforcement increases the rainfall amount in the study area. This can be ascribed to the direction of the moist air masses coming from the Atlantic Ocean and directed to the north-western coast of Spain and to the Mediterranean (Degeai et al., 2020; Martín et al., 2012; Martin-Vide and Lopez-Bustins, 2006). In this dynamic state the moist air masses can reach Tuscany, enhancing local cyclogenesis and rainfall.

The SCC values indicate that the influence of the Genoa Gulf Low decreases in summer and autumn the correlation between rainfall and EA is strong in winter and summer; in summer, the correlation with rainfall is mainly with EA. In winter, the link between EA and rainfall is the same for NAO. In summer, the greater representativeness of EA than NAO on the Azores High allows a better understanding of the connection between rainfall and global climate in this season. In detail, the formation of the Azores High and of the African High results in an increase in the EA index, and this means that there is reduced precipitation in the study area. In autumn, the statistical correlations do not allow to create a link between large-scale circulation and rainfall. Indeed, we can observe a weak anticorrelation with NAO, a weak correlation with EA, and no correlation with WeMO. This method seems unsuitable to represent the autumn season with its atmospheric dynamics.

The results of the linear models are consistent with the statistical correlation results for the DJF, MAM and JJA seasons, while we observe some differences in SON. The strong correspondence between the two methods in DJF, MAM and JJA makes it possible to validate our linear model. In autumn, the analysis of the linear models identifies an important role of NAO, and therefore a link between northern Atlantic atmospheric circulation and rainfall in the study area. In autumn, the coefficients of NAO (α) are negative and this means that an increase in the index is linked to a decrease in rainfall in the study area. This mathematical result is more plausible than that obtained from the analysis of correlations based on the notions of atmospheric physics introduced previously.

Finally, the linear model-based method allow us to refine our investigations and to improve our knowledge of the dynamics in the Mediterranean over the seasons.

The use of our linear models offers the advantage of clarifying the role and influence of large-scale atmospheric circulation on rainfall over the study region in different seasons, and this may appear controversial when using only the statistical correlation. These linear methods can also be useful for rainfall prediction, although the aim of this paper is not the production of the best model for predictions. A more complex model may be better suited to reduce the overall model; however, it would have been difficult to understand the influence of each input parameter, which is the main scope of this paper.

2.4.2 Long-term rainfall trends and relation with climate patterns

This study identify a confused trend for the DJF, MAM and SON rainfall, while the JJA rainfall clearly tends to decrease, in aggrement with those of other studies based on different rainfall datasets (Caloiero et al., 2018; Deitch et al., 2017; Philandras et al., 2011). More specifically, Deitch et al. (2017) studied the seasonal trend of rainfall in the Mediterranean area, demonstrating a negative trend for summer rainfall and no trend for winter/autumnal rainfall in Tuscany.

The DJF seasons are characterized by significantly decreased precipitation between 1984 and 2005 (Figure 2.4). This period is marked by a positive phase of NAO and EA and a negative phase of WeMO. Starting around 1984, the increase in NAO and EA is due to an increase in NASST (Figure 2.4). An increase in NASST is correlated to an expansion of the Azores High and a consecutive reduction of the Iceland Low, resulting in the formation of the NAO and EA positive phases (Börgel et al., 2020; Frankignoul et al., 2003; Robertson et al., 2000; Visbeck et al., 2001). The following increase in rainfall from 2005 to 2020 seems to have been caused by an increase in the WeMO, and therefore by an increase of the Genoa Gulf Low persistence. This could indicate a change of the main climatic driver in relation to the previous period (Figure 2.4).

The MAM season presents a decrease in the amount of rainfall in the period between 1985 and 2008 (Figure 2.5). The WeMO constantly decreases with progressive intensification of the negative phase. This indicates a gradual reduced intensity of the Genoa Gulf Low. The GGSST has progressively increased since 1985. Furthermore, NAO and EA are in a persistent positive phase. Since 2008, there has been a weak increase in the precipitation trend. The JJA rainfall trends have the highest correlation with EA, while NAO and WeMO have a lower influence (Figure 2.8 and 10). The increase in NASST, MSST and GGSST induces

the NAO and EA indices to a positive phase, and WeMO to a negative phase. This process induces a progressive reduction of rainfall trends in this season. SON is characterized by rainfall trend variability with two wet periods and two dry periods (Figure 2.7). Each dry period is marked by an increase in NAO, whereas the wet period results from an increase in WeMO linked to a weak decrease in GGSST (Figure 2.7). The increase in sea surface temperature is greater in the warm periods of the year and is caused by current global warming. From these observations, we can evince that the warm periods of the year are marked by a greater decrease in precipitation resulting in less water availability in the environmental system.

2.4.3 Influence of the temperature on rainfall regime

The results of the relation between rainfall and temperature in Tuscany confirmed some evidences from previous works in the scientific literature (Hardwick Jones et al., 2010; Lenderink et al., 2017; Lenderink and van Meijgaard, 2008; Panthou et al., 2014; Pumo et al., 2019). The scaling methodology and the analysis of the temperature anomalies during EPEs show a relationship between the rainfall and temperature, which is influenced by the quantile investigated and the rainfall accumulation period. The scaling rate increases with decreasing accumulation period and, independent of the accumulation period, it increases with increasing percentile. The same behaviour is observable from the analysis of the temperature anomalies occurred during EPEs. These results are in agreement with other studies (e.g., Hardwick Jones et al., 2010; Pumo et al., 2019).

The quantiles higher than 0.9 of each season are characterized by scaling rate values higher than 7% (super-CC) for each rain accumulation period (with the highest values recorded for the lowest accumulation period). In many cases values also higher than 10% are recorded. This characterizes especially the wet season, while in dry season the highest rain accumulation periods have lower values than the respective of the wet season. This is in agreement with several works carry out in the middle latitudes, for example in United Kingdom (Blenkinsop et al., 2015), Netherlands (Lenderink et al., 2017; Lenderink and van Meijgaard, 2008), Germany (Berg et al., 2013), Austria (Formayer and Fritz, 2017), western Europe (Lenderink and van Meijgaard, 2010), Romania (Busuioc et al., 2016) and Sicily (Pumo et al., 2019, 2018).

The dry season is also characterized by negative values of scaling rate for the highest rainfall accumulation periods and for almost all quantiles. This is in agreement with the previous results of this work (see

paragraph 2.4.2), where it is observed a decrease of the rainfall amount in the dry season in Tuscany. As discussed above, this decreasing rainfall amount could be linked to an increase of the African High during the summer which is caused by the increasing temperature. Indeed, during high-pressure systems, the temperature increase cannot correspond to a humidity increase (Berg et al., 2013, 2009; Hardwick Jones et al., 2010; Pumo et al., 2019).

3 Relationship between river discharge and coastal erosion

Coastal areas are certainly the most exposed to the effects of climate change (Bini and Rossi, 2021). In this work, we study in detail an area of the Tuscan coast, particularly suited to this type of study due to the long state of erosion (Bertoni et al., 2021; Bini et al., 2008) both for the presence of a good amount of data available and for the presence of different degrees of anthropization (Bertoni et al., 2021).

3.1 Pisan coastal plain

The Pisan coastal plain has been progressively shaped by the Arno river since the Late Holocene (Bini et al., 2015; Federici and Mazzanti, 1993; Pranzini, 2001; Sarti et al., 2010) (Figure 3.1a,c–e). In this area, SW winds have the highest frequency in each velocity range, while NW winds are frequent but subordinate to the former (Cipriani et al., 2001). Major storm events come from W/SW and SW, even if high energy events can also be related to NW winds (Cipriani et al., 2001). Detailed analyses (Casarosa, 2016) show that more than 90% of storms (on average 48 events per year) originate in the 220–260° N sector, while less than three events per year generally occur in the 210–180° N sector. Finally, only less than one event per year comes from other sectors (Figure 3.1b) (Casarosa, 2016).

In the coastal sector located in the hydrographic left of the Arno River the littoral drift is mainly oriented towards the south, with the exception of the area between Calambrone and the Scolmatore Canal, where the littoral drift is N-S oriented. Conversely, in the coastal sector located in the hydrographic right, the littoral drift is N-S oriented (Anfuso et al., 2011; Pranzini, 2001) (Figure 3.1c,d). The coast experiences a microtidal regime, where the spring tide is only ca. 30 cm (Bertoni et al., 2019).

The coastal plain studied has been affected by a prolonged period of coastal erosion (Besset et al., 2019, 2017; Bini et al., 2008; Borgh, 1970; Grottoli et al., 2019; Palla, 1983; Pozzebon et al., 2018; Toniolo, 1910). This process is thought to be mainly linked to anthropogenic activities (riverbed dredging, mountain reforestation, diffused riverbed reinforcement, river barriers), which have caused a drastic decrease in the sedimentary load of the Arno River (Anfuso et al., 2011; Cipriani et al., 2001). During the Little Ice Age, some studies highlighted a high rate of Arno River solid transport processes which were probably interrupted by progressive reforestation of the watershed starting from the beginning of the XX century (Diodato, 2007; Diodato et al., 2021; Regione Toscana, 2009). Some key areas for the local touristic economy have been

particularly affected by erosion (area A in Figure 3.1 and area B in Figure 3.1d). In these two areas, separated from the mouth of the Arno River with its engineering structures built in 1926, the local authorities applied different approaches in the management of the territory. Specifically, the Area A located in the Migliarino San Rossore Massaciuccoli Natural Park and characterized by a highly natural environment and few anthropogenic structures, was allowed to evolve without the construction of coastal protection structures until 2001. The only exception was five detached breakwaters, built between 1962 and 1968 to defend the Gombo beach. Here, in 1984, after limited results, four out of five breakwaters were elevated and extended, resulting in the formation of tombolos (Pranzini et al., 2018). More recently (2001 and 2003), 10 emerged groins with submerged extensions were built between the Gombo beach and the Arno River mouth (Bertoni and Mencaroni, 2015; Casarosa, 2016; Pranzini et al., 2018). In 2009 an artificial tombolo was constructed to connect the fourth breakwater and two submerged groins. These last structures were quickly destroyed by coastal erosion (Pranzini et al., 2018).

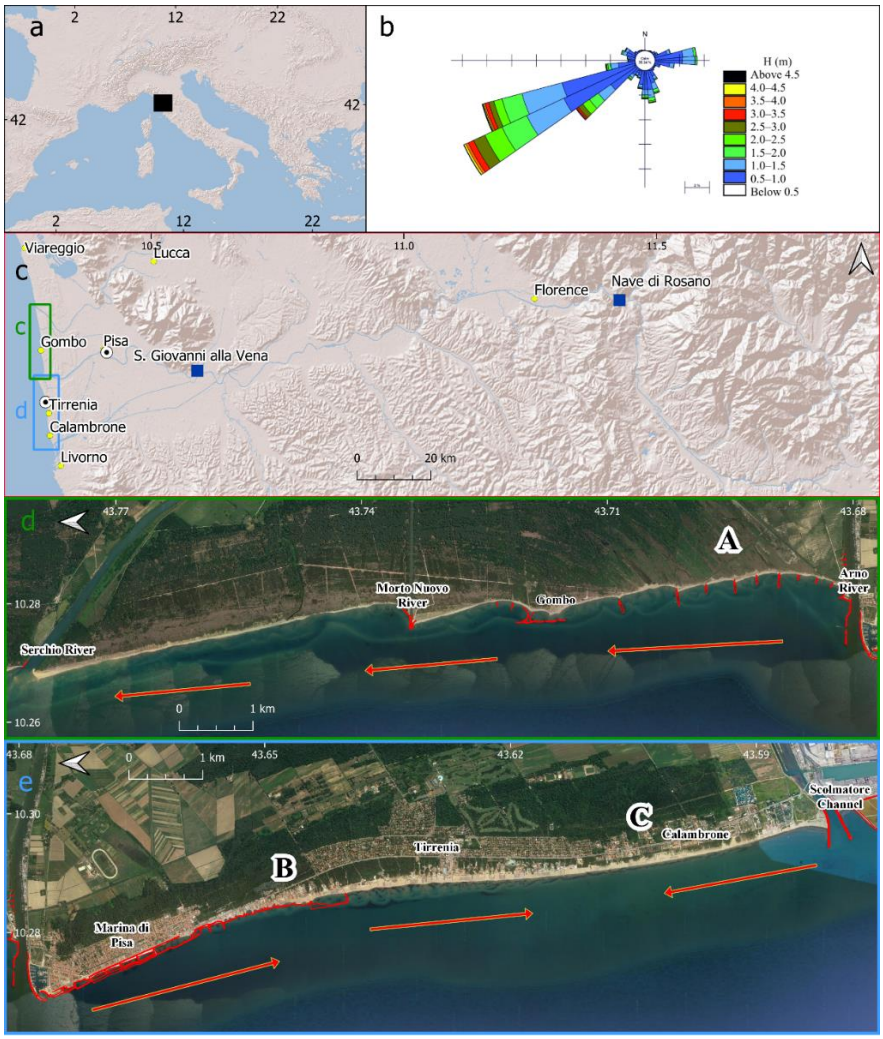

Figure 3.1 Location map of the study area (a,c,d,e); (b) directional analysis of wave data (https://www.cfr.toscana.it/index.php?IDS=42&IDSS=282) recorded at the Gorgona Buoy (43.57N; 9.95E) grouped by average direction of origin and by height wave classes, data between 1 October 2008 and 1 May 2012 (after Casarosa, 2016, modified); (c) Arno River course (blue line), hydrometers (blue squares), location of samples used for grain-size analyses (black and white dots); (d) and (e) northern and southern sectors respectively of the study area, red arrows indicate the littoral drift direction (Anfuso et al., 2011; Bini et al., 2008)), the red line indicates the coastal defense structures (after Bini et al., 2021, modified).

3.2 Material and Methods

The changes in the shoreline position of the Pisa coastal plain were studied considering period of 142 years (from 1878 to 2020) by using a heterogeneous database consisting of topographic maps, airborne images and DGPS (Differential Global Position System) measurements (Table 3.1). The data were managed using the open source QGIS 3.x software. A linear vector with the position of the shoreline (derived by manual operator delimitation and digitalization) was created for each analyzed year until 2008. The data of the last 12 years were derived from dedicated DGPS surveys performed following the methods proposed by

(Pranzini and Simonetti, 2008). The differences in the area between the shorelines acquired in different years were calculated in terms of annual gains and losses.

All the data available were processed using GIS tools in order to identify the coastal areas characterized by the advancing shoreline (gain of territory) and those characterized by the retreating shoreline (loss of territory) for the entire period considered. Specifically, a comparison of the shoreline in the successive years made it possible to identify coastal sectors that had never experienced erosion and others that had never experienced advancement in the last 142 years. The areas were classified in four categories: i) area constantly in advancement; ii) area constantly in erosion; iii) areas mainly in erosion; iv) areas mainly in advancement.

One of the longest and most complete sets of daily discharge data of the Arno River was also analyzed. The daily discharge data were recorded at the S. Giovanni alla Vena gauge (data from 1924 to 2020; https://www.sir.toscana.it/consistenza-rete), 35 km inland from the river mouth (Figure 3.1b). The discharge value measured at this gauge is significant because it could be considered close to the discharge value at the river mouth, considering that there are no important tributaries downstream from the gauge.

The trend of the daily discharge data since 1924 has been analyzed to identify the main variations of that period. The return times for flood events were calculated as opposites of probability:

$$p = \frac{1}{T}, \tag{11}$$

where p is the probability and T the return time. This equation can be applied for frequent events, but it can be difficult to determine the return time of an extreme event if the occurrence of these events is too small in the series history (van den Brink et al., 2005). For this statistical reason, we investigated the role of flow events with a maximum return time less than ten years.

In order to identify possible correlations, the set of discharge data were analyzed and compared with the erosion trends, as documented by the study of the shoreline positions. Since a rigorous statistical treatment of the data was not possible because of the low number of shoreline measurements (despite the long period considered), a qualitative comparison was made between the trend of erosion and the trend of discharge.

The trend of the selected flow range was compared with erosion over time by using a moving average calculated over ten years. The use of the moving average to understand the trend of river discharge is a

validated method, as demonstrated by several authors (e.g., Merabtene et al., 2016; Pulido-Velazquez et al., 2015; Zhang et al., 2020). To support the analyses, we investigated Sentinel-2 images acquired during two recent flood events occurred on 3 February 2019 and on 3 December 2019, in the most frequent wind and sea condition (winds and waves from NW and SW, respectively; Figure 3.1b) in order to identify the presence of sediments and their longshore and offshore dispersion. The selected images were analyzed by means of the tone mapping technique using Photomatix software, a software that allows the user to choose among different HDR profiles. After numerous tests, the use of the profile called "Painterly" was chosen. This profile gives the image a very photographic look and a well-exposed dynamic range. The image acquires an aspect that is very similar to the one perceived by the human eye and is often referred to "as the eye sees" in the photography field. After the application of this profile, the parameters of gamma, luminance and contrast varied, so as to make more readable all the information contained in the images. This method makes it possible to qualitatively identify the area subject to solid transport (according to the different shades and gradations of color). Moreover, the method allows the identification of flow lines of solid transport direction that show the dispersion of sediments out of the mouth towards the coast.

In addition to the study of these two recent events, in order to extend the analyses of the plumes generated by the Arno River, we considered 151 frames from Landsat (5, 7 and 8) and Sentinel-2 satellites. All the images were filtered at a threshold of less than 20% cloudiness during the download procedures and were then checked manually. Specifically, 50 Sentinel-2 frames were chosen from 2015 to 2020 and 101 Landsat frames from 1984 to 2020. In particular, in this second case 68 frames were from Landsat 5, 14 from Landsat 7, and 19 from Landsat 8. The red band was analyzed for both satellites, corresponding to bands number 4 for Sentinel-2 and Landsat 8 and to number 3 for Landsat 5 and 7. A good correlation was found between the red band (630–690 nm) reflectance values and low-to-moderate turbidity (Dogliotti et al., 2015). The images were resampled on the same matrix. Two grids were extracted: the first one provides the maximum value recorded in the analyzed images for each pixel, while the second one provides the mean value calculated using the analyzed images for each pixel.

In an attempt to understand whether the types of sediment transported by the river were suitable to counter coastal erosion, we performed grain size analyses on sediments sampled on the riverbed near the city of Pisa (where the sediments left by the river were easy to sample) and on the beach (area C, Figure 3.1)

immediately after a flooding event occurred on 3 December 2019, which was one of most representatives in this area, in terms of both wave direction and river flow. The samples were dried in an oven at 40 °C for 48 h. Each sample was then weighed and analyzed by means of standard sieving with mesh size 1 mm, 0.5 mm, 0.315 mm, 0.250 mm, 0.125 mm and 0.063 mm. After weighing the fraction left in each sieve a grain size curve was constructed using GRADISTAT (Blott and Pye, 2001). Finally, to check the effective ability of solid load to counter coastal erosion, we undertook a dedicated DGPS survey in a small stretch of coast in the southern sector (part of area C) about one month after the flood event of 3 February 2019.

Table 3.1**.** Census of shoreline data used in this study.

Year	Ownership Organization	Data type	Properties	Source
1878	I.G.M	Cartography	Scale 1:25000	Bini et al., 2021
1907	I.G.M	Cartography	Scale 1:25000	Bini et al., 2021
1928	I.G.M	Cartography	Scale 1:25000	Bini et al., 2021
1944	R.A.F.	Aerial photographs	Black and white film	Bini et al., 2008
1954	Tuscany Region	Aerial photographs	Black and white film	Bini et al., 2008
1965	I.G.M	Aerial photographs	Black and white film	Bini et al., 2008
1975	Tuscany Region	Aerial photographs	Black and white film	Bini et al., 2008
1978	Tuscany Region	Aerial photographs	Color film	Bini et al., 2008
1982	Tuscany Region	Aerial photographs	Color film	Bini et al., 2008
1982	I.G.M	Aerial photographs	Black and white film	Bini et al., 2008
1986	I.G.M	Aerial photographs	Black and white film	Bini et al., 2008
1990	I.G.M	Aerial photographs	Infrared	Bini et al., 2008
1996	Tuscany Region	Aerial photographs	Black and white film	Bini et al., 2008
2003	Orthophoto	Aerial photographs	Black and white film	Bini et al., 2008
2004	Pisa Province	Aerial photographs	Color film	Bini et al., 2008
2008		DGPS measurements		Casarosa, 2016
2009		DGPS measurements		Casarosa, 2016
2010		DGPS measurements		Casarosa, 2016
2011		DGPS measurements		Casarosa, 2016
2012		DGPS measurements		Casarosa, 2016
2013		DGPS measurements		Casarosa, 2016
2014		DGPS measurements		Casarosa, 2016
2015		DGPS measurements		Bini et al., 2021
2020		DGPS measurements		Bini et al., 2021

3.3 Results

3.3.1 Shoreline GIS Analysis

The analysis of shoreline positions (Figure 3.2) shows that more than 2.5 km^2 of the studied area experienced constant erosion, while only 0.5 km^2 show constant advances (Figure 3.3). The areas most affected by erosion are located in the hydrographic right of the Arno River (Area A, Figure 3.2c and the area northward of the Morto Nuovo River, Figure 3.2a). In the hydrographic left (where erosion was countered by

several engineering interventions such as groins and breakwaters (Bertoni and Mencaroni, 2015; Bini et al., 2008; Cappucci et al., 2020; Pranzini et al., 2018)) the total area eroded is less in extent compared with Area A, but the erosion is persistent in the area marked B in Figure 3.2c. Coastal progradation has been documented mainly in the C area of the southern sector (Figure 3.2d), while minor local advances have also been identified in the northern sector immediately south of the mouth of the Morto Nuovo River (Figure 3.2b). From a chronological point of view, the highest values of erosion are documented around the years 1954, 1978 and 2012 (Figure 3.4), while the lowest values of erosion are reported for the periods 1881–1944, 1965–1975, and 2013–2020. It is worth noting that the erosion rates for the period before 1944 are similar to those recorded in the last 10 years (Figure 3.4).

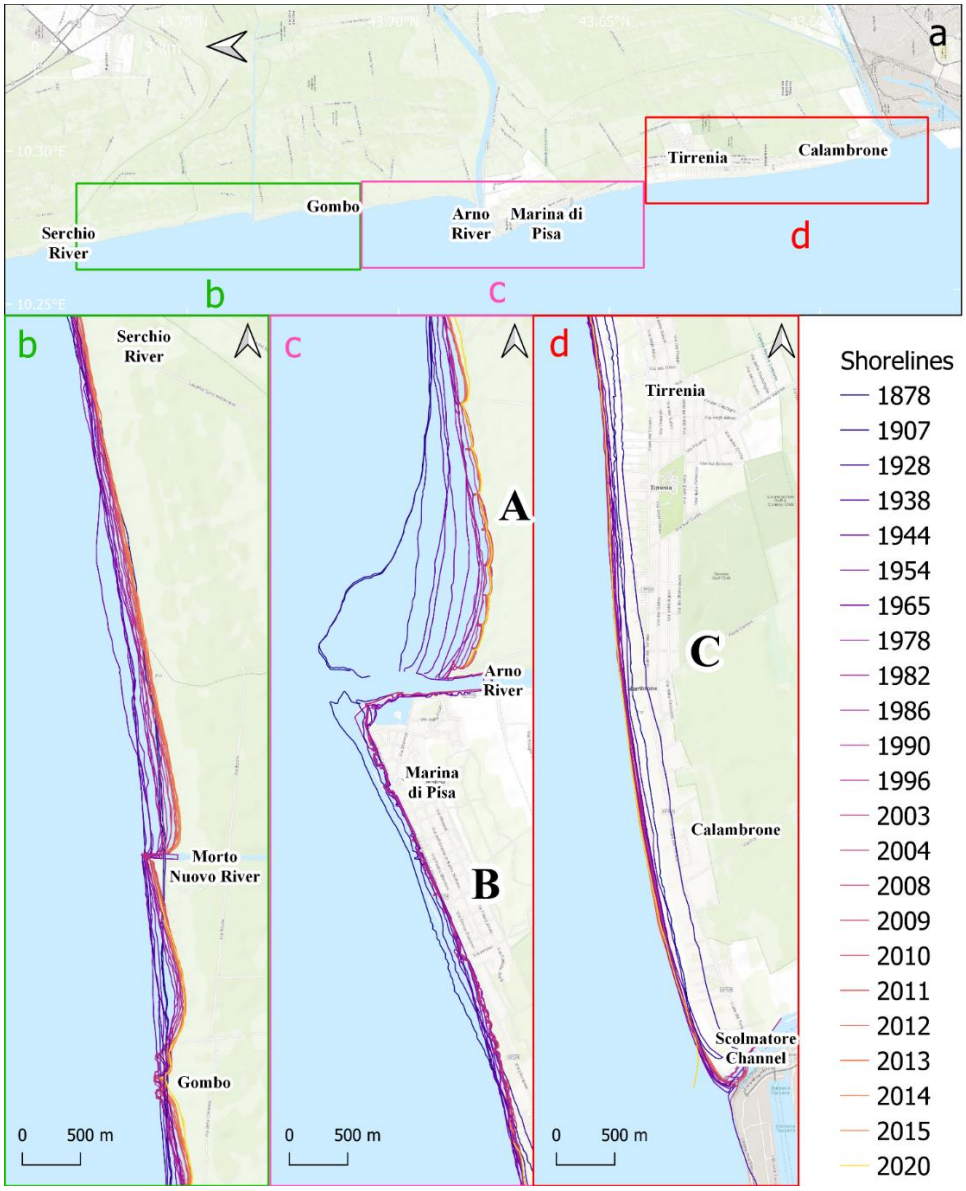

Figure 3.2 Location of the analysed coastal sectors (a, b, c, d). Shorelines extracted from the various sources reported in Table 1 (after Bini et al., 2021, modified).

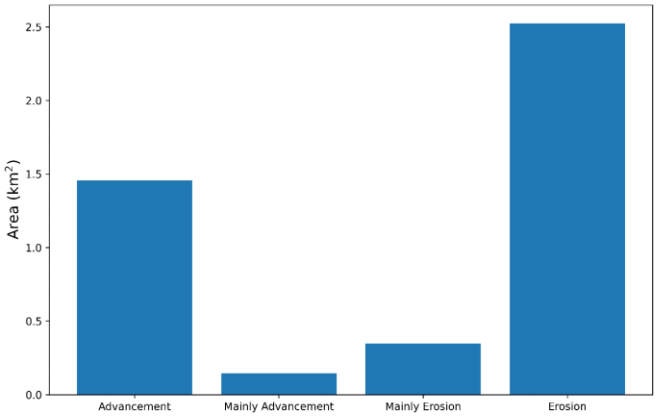

Figure 3.3 Spatial variation of the investigated coastal area. Analysis of the shorelines in the last 142 years allows identification of the sectors in constant advancement (progradation), in constant erosion, mainly advancement and mainly erosion (after Bini et al., 2021, modified).

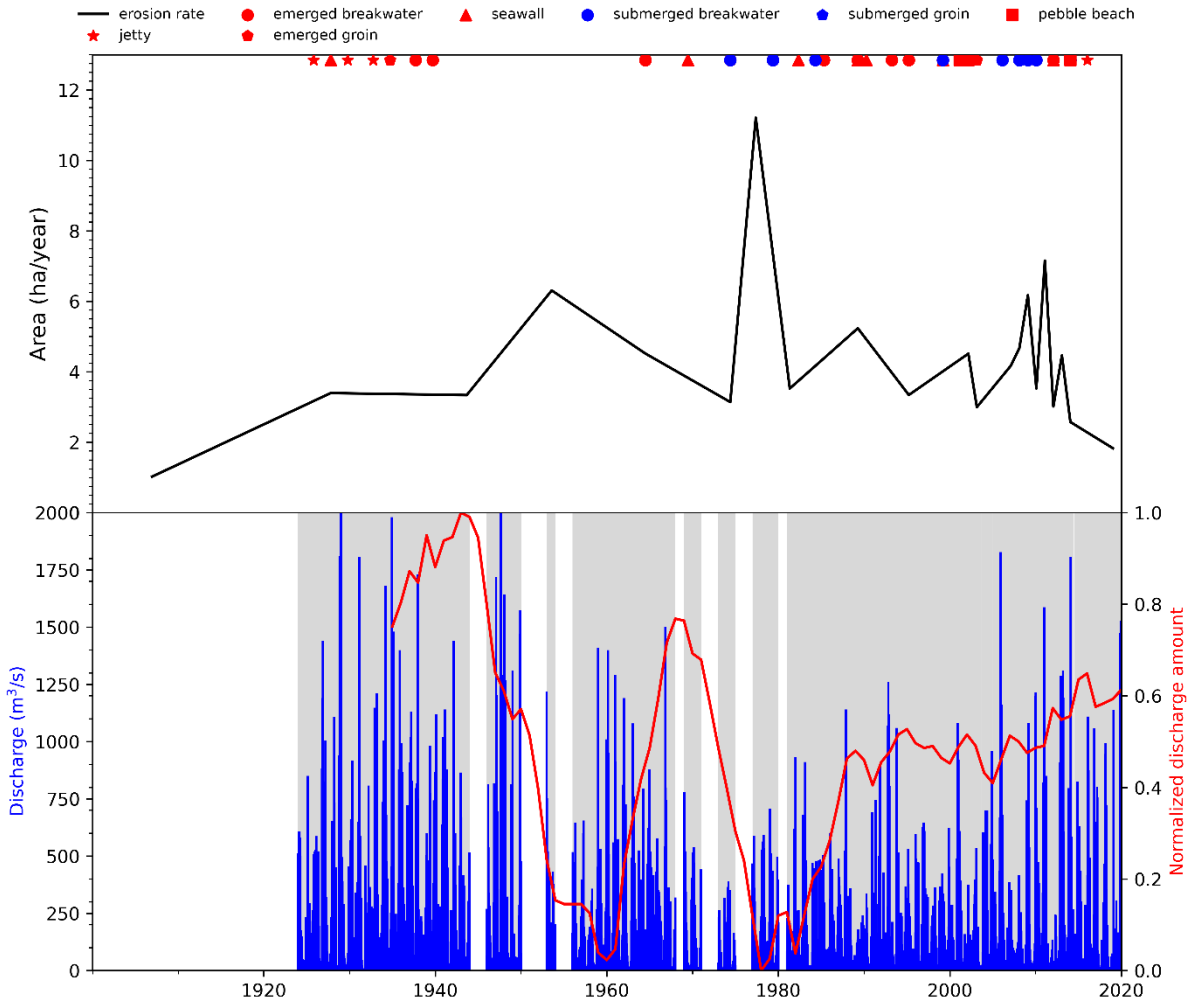

Figure 3.4 Trend of erosion from 1881 to 2020 of the investigated area (black line). Top: engineering structures built in the area over time. Daily discharge time series of the S. Giovanni alla Vena gauge data from https://www.sir.toscana.it/consistenza-rete (blue bars). The white bars indicate missing data. The red line shows the amount of normalized discharge using a moving window of 10 years (after by Bini et al., 2021, modified).

3.3.2 Discharge Data Analysis

Discharge analysis (Figure 3.5) shows the highest values until 1944, followed by a reduction in the period at the end of the 1950s and around the year 1980. These two periods are separated by a peak in the values of discharge. An increase in discharge values, which are still well below the values recorded before 1944, is documented from the end of the 1980s to the year 2005. Even if with some fluctuations, a further increase in the trend is documented after this year. We are aware that the lack of data in the 1950s and 1970s may affect the results, even if a clear decreasing trend, probably not so marked, can be identified from the available data. Return time analysis of the historical series of S. Giovanni alla Vena (Figure 3.5) with a 100 m^3/s discretization shows an exponential trend with a one-year return time corresponding to a flow rate of 700/800 m^3/s.

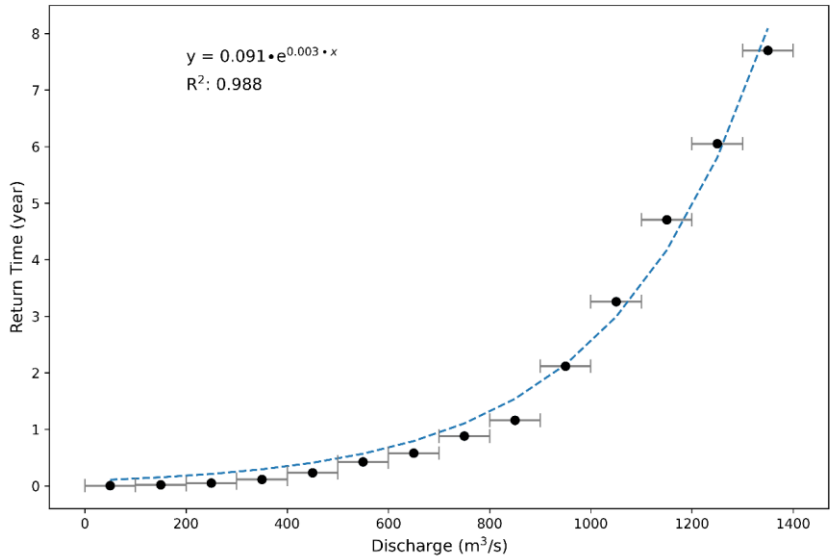

Figure 3.5 Return times for discharge intervals of the S. Giovanni alla Vena time series. Discretization of the discharge range in 100 m^3/s. The return times show an exponential trend (after Bini et al., 2021, modified).

3.3.3 Remote Sensing Analysis

The Sentinel-2 image recorded at 10:24 a.m. on 3 December 2019 shows the Arno River sediments dispersion along the coast during a flood event characterized by a peak discharge of 902.81 m^3/s at the S. Giovanni alla Vena section (return time of 1.5 years, Figure 3.5). This event occurred with a much more frequent wave direction varying from 240°N to 180°N (Tuscany Region, wave buoy of Gorgona: https://www.cfr.toscana.it/index.php?IDS=42&IDSS=282). The image processed by tone mapping (Figure

3.6) shows a wide plume formed by sediments transported by the river during this event and dispersed at the river mouth. Plume n. 1 in Figure 3.7 covers a total area of about 100 km^2. A minor plume (identified as 1A in Figure 3.6) covering a total area of about 10 km^2 is also well visible in the image. The dispersion of sediments shows that a large amount of transported sediment was dispersed offshore. In agreement with the wind and wave directions, the plume shows a deviation towards NNW, together with the other minor plumes of the Scolmatore Channel located further south. The reconstruction of the flow line allows the identification of two shadow areas in sediment dispersion: one located in the northern sector between the *Lame della Gelosia* and *il Gombo* (area A in Figure 3.6), and the other one situated in the southern sector in front of the village of Marina di Pisa (area B in Figure 3.6).

The Sentinel-2 image recorded at 10:22 a.m. on 6 February 2019 shows the final phase of the flood event of February 3, characterized by a wave direction from 300°N (which is the second in occurrence), and a fluvial discharge of 1131 m^3/s at the S. Giovanni alla Vena gauge (return time of 3 years, Figure 3.7). In this case a significant volume of sediments was dispersed offshore, while the entire solid longshore transport faced south (Figure 3.7). Apart from the first kilometer to the north of the river mouth, the northern sector does not receive any sediments. In the southern sector, the shadow area in front of Marina di Pisa is still visible; instead, according to wave direction analyses, a part of the solid load reaches the southernmost area in correspondence to the village of Tirrenia and the borough of Calambrone (area C, Figure 3.1d).

A more generalized analysis of sediment dispersion of the Arno River along the coast was performed considering several images for the period 1984–2020 (Landsat and Sentinel-2). Specifically, Figure 3.8 shows the result of processing the 50 Sentinel-2 and the 101 Landsat 5, 7 and eight images. The analysis was performed using the red band. In the first data processing the final images (Figure 3.8a,c) were obtained considering in each pixel the mean value recorded in all the analyzed images. Specifically, the mean value on the red band of the 50 analyzed Sentinel-2 images is recorded in each pixel of Figure 3.8a, while the mean value of the 101 analyzed Landsat images is recorded in each pixel of Figure 3.8c. In the second processing data the final images are obtained considering in each pixel the maximum value recorded on the red band in all the analyzed images (Figure 3.8b for the Sentinel-2 Images and 8d for the Landsat images.). All the images obtained show that the area to the north of the river mouth is characterized by a greater reflection on the red band than the southern area. This suggests a different distribution of the sediment between the

northern part and the southern part. In particular, the southern area near the mouth of the river has the lowest reflection values for the entire stretch of coast studied. Moreover, the shadow areas described (Figure 3.6 and Figure 3.7) in the northern and southern sectors are confirmed also in Figure 3.8b,d, which consider the maximum pixel value. The images based on the mean values (Figure 3.8a, c) allow identification of the main distribution of the sediment in the period studied (considering only the mean value of the differences among the various sectors are minimized). The images based on the maximum values (Figure 3.8b) accentuate the differences between the areas that received a greater supply of sediment and those with the opposite behavior.

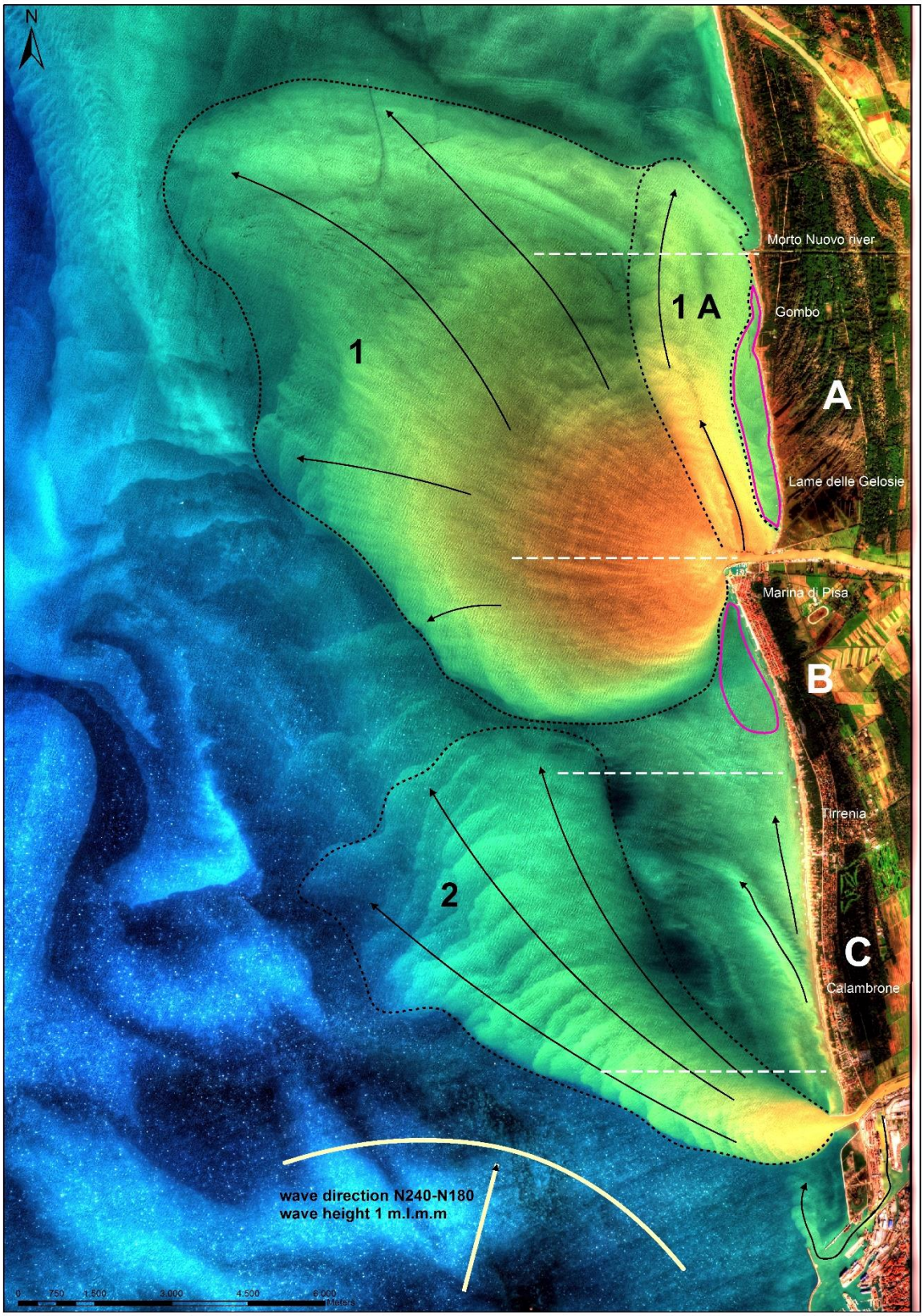

Figure 3.6 Sentinel-2 image showing the Arno flood event of 3 December 2019 characterized by a fluvial discharge of 902 m^3/s at the S. Giovanni alla Vena gauge and wave direction N 240–180. Black arrows show the sediment flow directions derived from a qualitative analysis of the image using the tone mapping method to emphasize the contrast. Dashed lines highlight the main plumes at the different river mouths. Purple lines enclose the shadow areas (after Bini et al., 2021, modified).

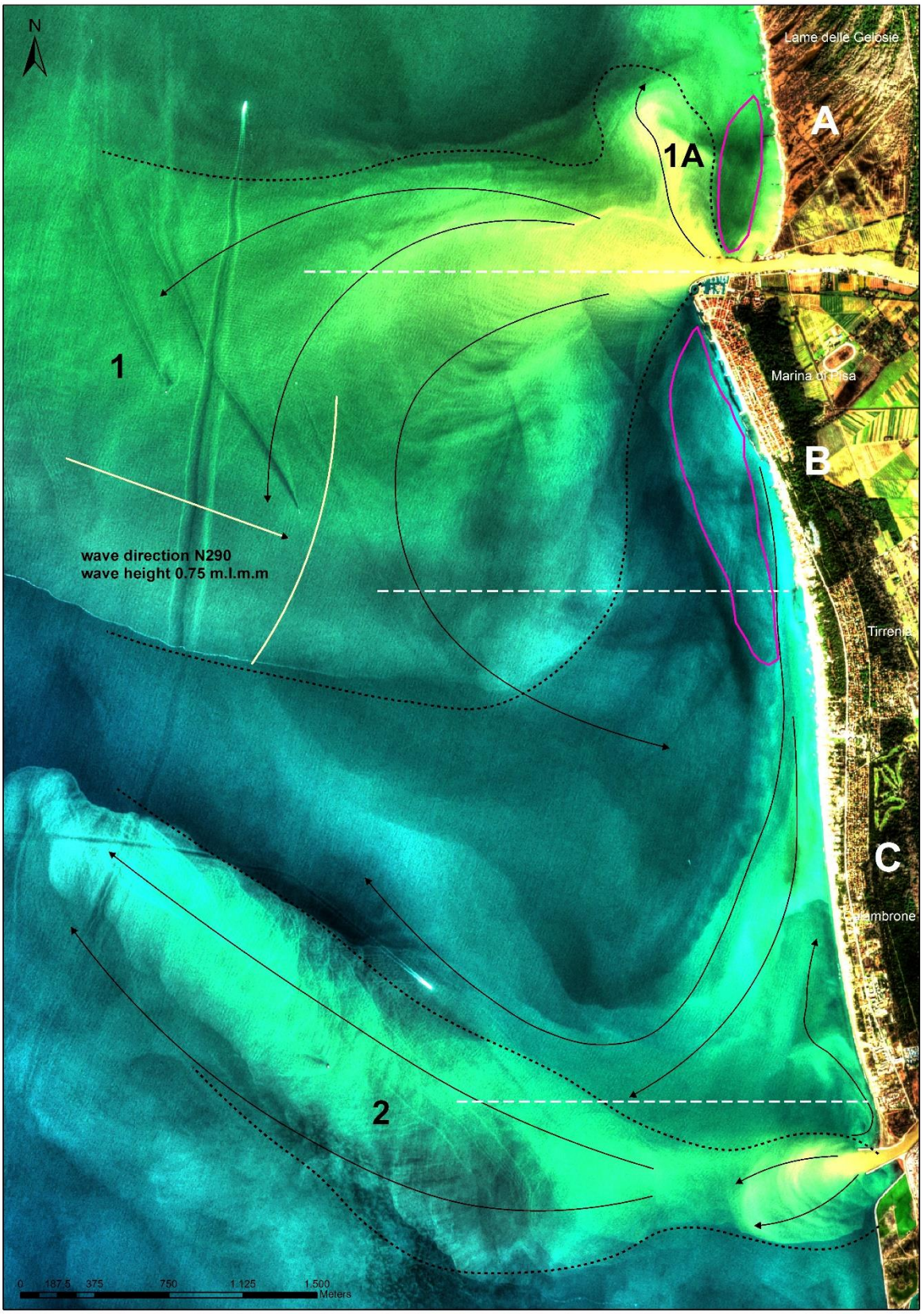

Figure 3.7 Sentinel-2 image of 6 February 2019 showing the end of the Arno flood event of 3 February 2019 characterized by a fluvial discharge of 1131m^3/s at the S. Giovanni alla Vena gauge and wave direction N 290. Black arrows show the sediment flow directions reconstructed after qualitative analysis of the image using the tone mapping method to emphasize the contrast. Dashed lines highlight the main plumes at the different river mouths. Purple lines enclose the shadow areas (after Bini et al., 2021, modified).

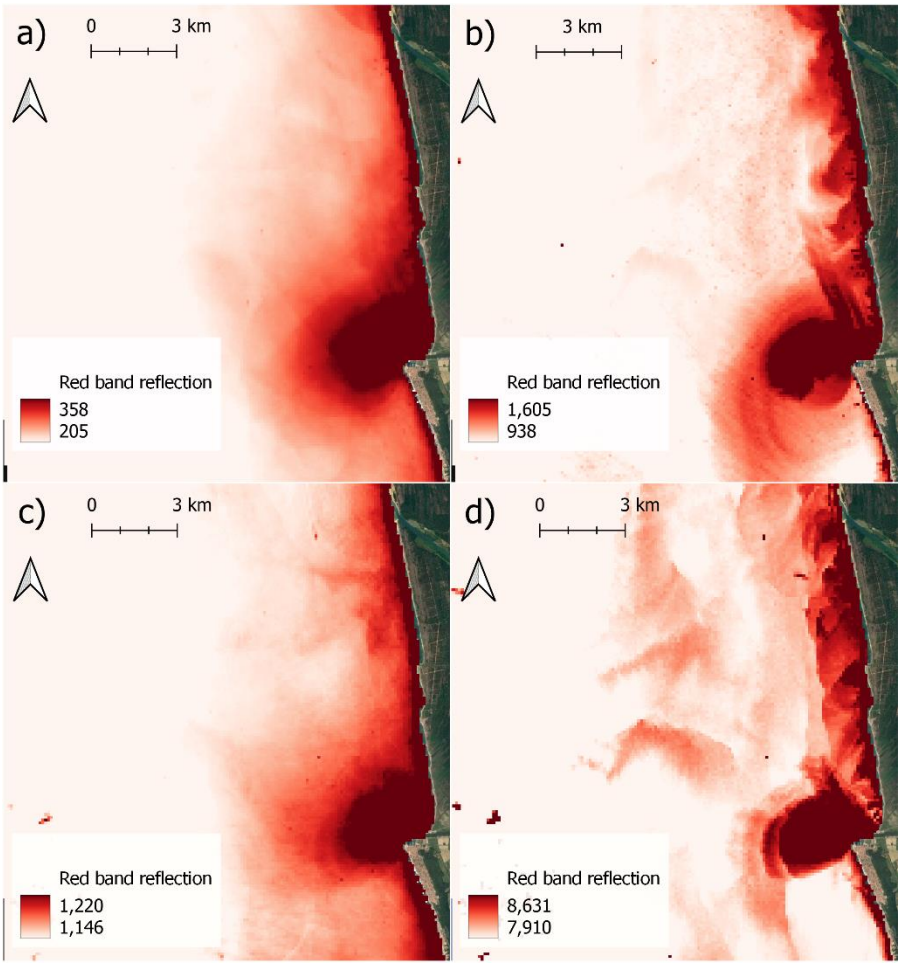

Figure 3.8 Analyses of the red band of 50 Sentinel-2 images and 101 Landsat images, acquired during the period 1984-2020. In each pixel the mean value recorded in the Sentinel-2 images (**a**) and Landsat images (**c**) respectively, are shown. In each pixel the maximum value recorded in the Sentinel-2 images (**b**) and Landsat Images (**d**), respectively, are shown (after Bini et al., 2021, modified).

3.3.4 Post-Flood Field Investigations

In the C area between the little village of Tirrenia and Calambrone, new DGPS shoreline measurements acquired before and about one month after the flood of 3 February 2019 document an advance of the coastline (Figure 3.9). More precisely, on a linear stretch of coast of about 6.5 km, there was an increase of the land of about 16,400 m^2 following this event, which occurred under more favorable conditions of the wind and sea states (wind and wave directions from NW) for nourishment of the southern sector. Grain size distribution of sediment collected in two sites (the first one on the sediments left by the river on the city center embankment and the second one on the beach of the C area: Figure 3.1b) shows an evident analogy between the samples and a predominance of coarse (50% ca) and medium sand (45%) in both the cases

(Figure 3.10), excluding the plumes identified by remote sensing that were formed by fine material unsuitable for beach nourishment.

Figure 3.9 (a) Coastline monitoring in the area C, 23 days after the event of 3 February 2019. Red line DGPS measurements acquired on 1 October 2018, and yellow line DGPS measurements acquired on 26 February 2019. The numbers in figures 9 (b) and (c) represent the areal changes (in m^2) between the two acquisitions (after Bini et al., 2021, modified).

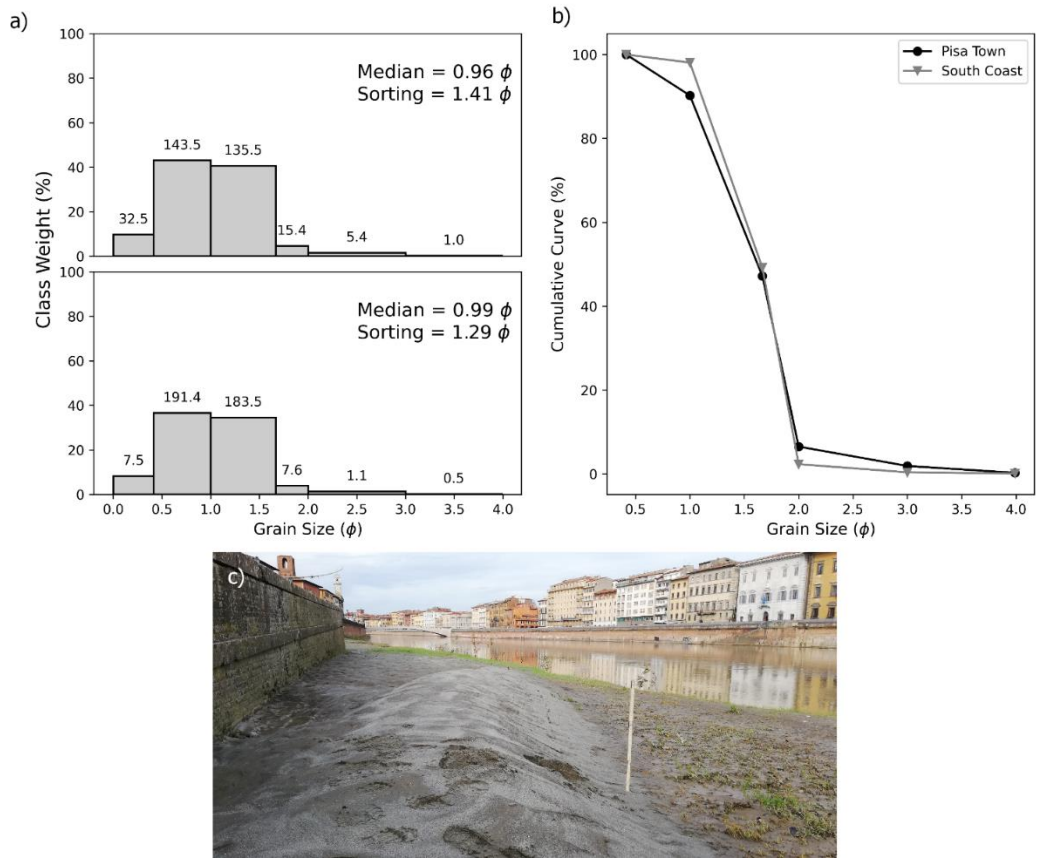

Figure 3.10 Grain size analysis of sediment samples in the city of Pisa and along the South Coast. (a) Histogram of grain size (ϕ) of samples in Pisa (top) and along the South Coast (bottom); (b) cumulative curve of two samples; (c) photograph showing sampling site (after Bini et al., 2021, modified).

3.4 Discussion

The analysis of the coastline position during the last 142 years represents the most comprehensive study ever performed on the history of coastline evolution of the Pisa coastal plain. Our results actually expand the work of Besset et al. (2019), both in terms of time (Besset et al., 2019 consider only the period between 1944 and 2015) and resolution, since they mainly consider satellite images. Analysis of the data shows a predominance of areas permanently affected by erosion, corresponding to 60% of the total area investigated. Following a period of progradation due to the phases of Arno delta construction beginning at about 3000 ka BP (Bini et al., 2015; Mazzanti, 1994; Pranzini, 2001; Sarti et al., 2015, 2010), different parts of the Pisa plain experienced marked coastal erosion, which started at the end of the 19th century and increased after the construction of the river mouth jetty, especially on the hydrographic right (Bini et al., 2008; Casarosa, 2016; Pranzini et al., 2018; A R Toniolo, 1910; Toniolo, 1927).

However, with the exception of A area (Figure 3.1), which was particularly affected by erosion, the overall value of erosion remained low until the 1950s when there was a rapid documented increase of the process. Erosion was particularly severe at the end of the 1980s, probably caused, among other things, by the effects of dredging/damming (Autorità di bacino del Fiume Arno, 2000; Billi and Rinaldi, 1997). The following period was characterized by an increase in erosion around 2010, while a reduction in the erosion rate was documented in the last eight years (since 2012). The period most affected by erosion was around the 1980s, particularly the area northwards of the Morto Nuovo River, A area where the Arno mouth jetty limits sediment flow that evolved naturally until 2001, and B area, where several human interventions designed to mitigate the erosion effects have been constructed since the beginning of the twentieth century (Aminti et al., 2004; Pranzini et al., 2018).

In the absence of precise modern measures of solid load, Cavazza, (1984) and Paris and Becchi (1989) provide an estimate of 1.5 t/yrs. In addition, only eight sporadic measurements were made far from the river mouth by (Paris et al., 2012). It is possible to indirectly define the role of solid load in countering erosion, in an attempt to create a correlation with fluvial discharge (Besset et al., 2019; Billi and Fazzini, 2017). The sporadic data obtained by Paris et al. (2012) highlighted the presence of sand in the suspended sediments transported by the river, starting from the discharge value of about 500 m^3/s at the Nave di Rosano gauge (Figure 3.1). Figure 3.11a shows the sections of S. Giovanni alla Vena and of Nave di Rosano, while Figure 3.11b shows the relationship between the discharges of these two stations. The linear regression of the two datasets is represented by the following equation:

$$y = 0.60x - 1.86, \quad (12)$$

where y is the discharge of Nave di Rosano and x the discharge of the S. Giovanni alla Vena. The equation highlights that the discharge at Nave di Rosano is about 60% the discharge at S. Giovanni alla Vena. R^2 of the linear regression is 0.79 and RMSE (Root Mean Square Error) is 40.25 m^3/s. By using the outflow scale provided by the Regional Hydrologic Service of the two investigated stations, we can derive the velocity as a function of discharge (Figure 3.11c). A discharge of 500 m^3/s at Nave di Rosano corresponds to a flow velocity of ca 1 m/s. The same flow rate at S. Giovanni alla Vena corresponds to a little less than 700 m^3/s discharge.

For this reason, it may be hypothesized that values of discharge starting from 700 m^3/s at *S.* Giovanni alla Vena are the most suitable to counter coastal erosion transported by suspended sand. These data are consistent with those observed in the Tiber River (Bellotti et al., 2011) in a climatic and environmental setting not very different from the Arno River catchment.

The role of solid load in countering the coastal erosion of this territory is documented by the qualitative anticorrelation between fluvial discharge and erosion rate (Figure 3.12). In particular, Figure 3.12 shows a minimum of fluvial discharge during the years 1954, 1978, 2012 corresponding to a peak of erosion, while in the years 1928–1944, 1954–1975, and after 2012 the erosion rate (despite some fluctuations) diminished, and the fluvial discharge increased. In the period 1960–2012 the river discharge was significantly low. This was particularly true for events >700 m^3/s (purple bars in Figure 3.12). It is logical to presume that the same occurred with the transported sediment load. It is perhaps for this reason that several authors (e.g., Anfuso et al., 2011; Bini et al., 2008; Pranzini, 1989), on the basis of the data available until 2010, considered the Pisa coastal plain to have evolved as a relict beach. However, this general trend seems to have changed over the last decade, with a slight decrease in erosion possibly caused by a slight increase of the solid load related to an increase in events greater than 700 m^3/s. In more recent years the data concerning the solid transport of sand in suspension starting from 700 m^3/s have been more reliable, and large environmental changes (in sections of the riverbed, availability of sediments resulting from different soil use in the catchment basin, etc.) can be excluded. Moreover, the quality of the shoreline data in the last 12 years (through high frequency DGPS acquisition) allowed to better understand the relationship between river discharge and the trend of erosion.

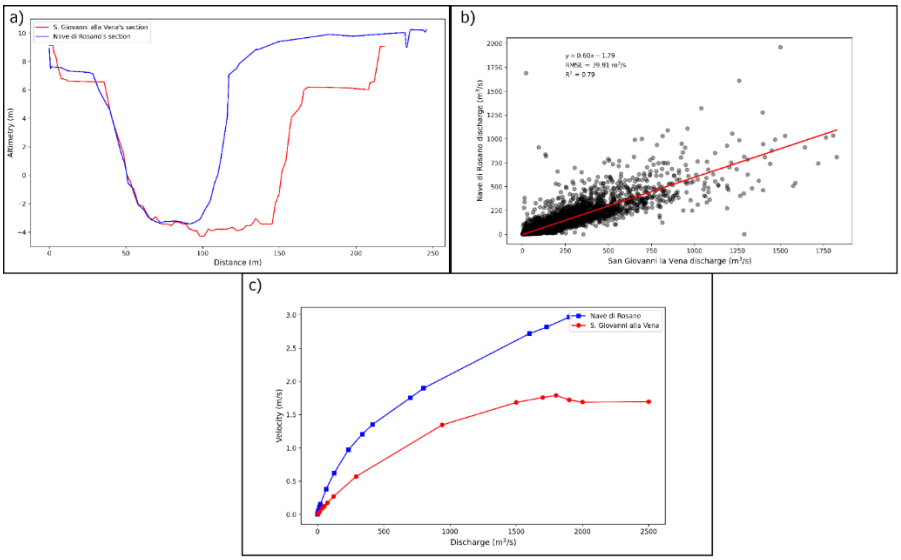

Figure 3.11 (**a**) River cross-section at S. Giovanni alla Vena gauge (red line) and Nave di Rosano (black line); (**b**) relation between discharges of the Arno River at S. Giovanni alla Vena and at Nave di Rosano; (**c**) relation between discharge and flow velocity resulting from the outflow scale at S. Giovanni alla Vena (red curve) and Nave di Rosano (black line). The location of the two gauges is highlighted in Figure 3.1c (after Bini et al., 2021, modified).

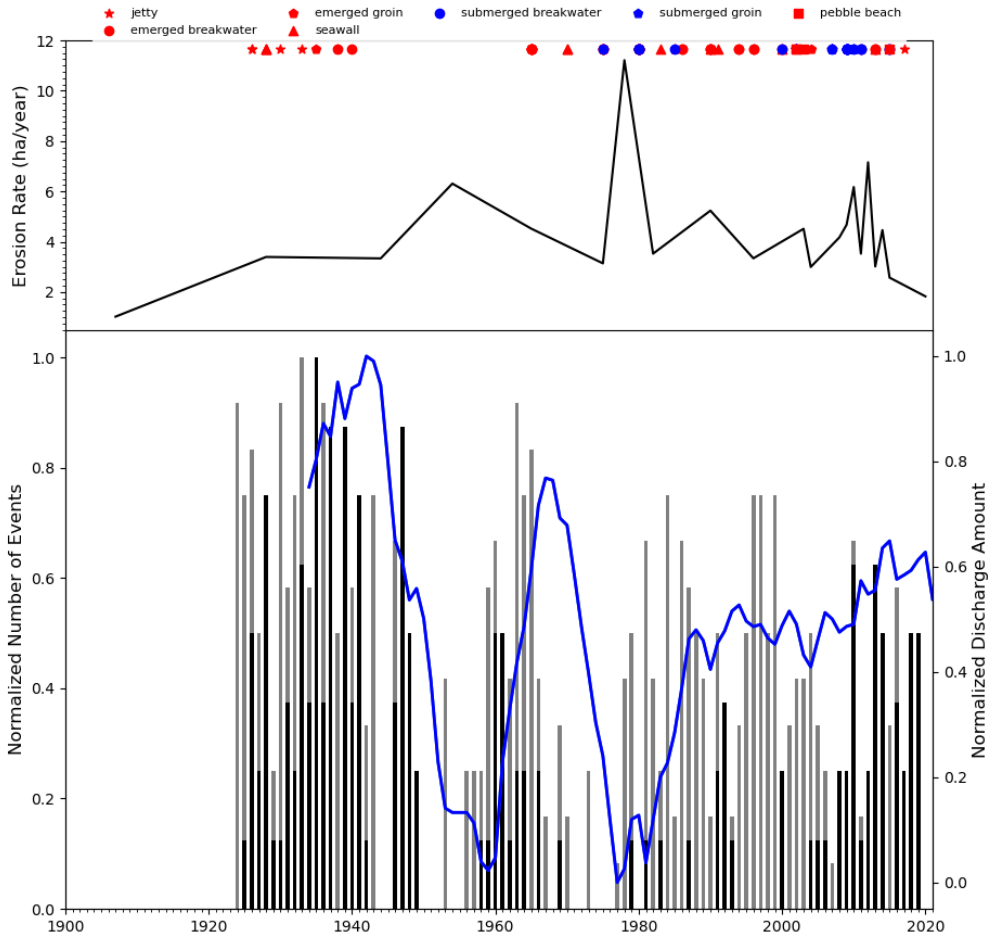

Figure 3.12 Relation between erosion rate of the coast (black line) and discharge of the Arno River over time. Number of flood events lower than 700 m^3/s recorded per year (grey bars) and the number of flood events higher than 700 m^3/s recorded per year (black bars). Data on number of events from Table S1. Normalized discharge amount with a 10 year mobile window of whole time series (blue line) (after Bini et al., 2021, modified).

The study of Sentinel-2 images related to the flood event of 3 December 2019 with fluvial discharge of ca 900 m^3/s (a little higher than the threshold of 700 m^3/s identified for the transport of sand), allowed us to identify the presence of a large plume of sediments in front of the mouth of the Arno River. Moreover, grain size analysis of the transported sediments highlighted the presence of well-sorted medium sand (>0.315 mm), perfectly consistent with the sediments characterizing different parts of the Pisa coastal plain (Pranzini and Simonetti, 2008) and suitable for coast nourishment. However, the sediments forming the plume were largely dispersed offshore.

Analysis of the images presented in Figure 3.6, Figure 3.7 and Figure 3.8 also made it possible to infer that strong erosion still characterizing some sectors of the Pisa coastal plain is related to the mode of longshore dispersion of the sediments that reached the coastline. Indeed, the analyzed flood event can be considered representative of most of the floods characterizing the Pisa coastal plain, which took place under the most common wind and sea state (more than 90% of events occurred with wind and wave directions from W/SW). The reconstruction of the flow lines (Figure 3.6) shows that areas A and B were not enhanced by the dispersion of sediments transported during the floods that occurred under these wind and sea state conditions.

The study of the events of 3 February (higher in discharge: ca 1100 m^3/s), which arose in less frequency but had more suitable sea state conditions in the southern sector (wind and wave directions from NW) underlines the presence of the same shadow areas. The most favorable condition for nourishing the northern beaches is the occurrence of floods with winds blowing and waves coming from SW, while the most favorable condition for nourishing the southern sector is the occurrence of floods with waves from the W and/or NW (Figure 3.6). Thanks to these studies it is possible to hypothesize that coastal sectors that are not fed by sediments during these events generally lack sedimentary supply. These interpretations have been also confirmed by analyses on several Landsat and Sentinel-2 images showing the process of sediment dispersion over the chronological interval 1984–2020. In all the cases analyzed, many Arno River sediments do not reach the coastline but are dispersed offshore. This aspect is likely to have more relevant effects on coastal erosion than the decrease in the solid load of sediments transported by the Arno River, as hypothesized by several authors (Anfuso et al., 2011; Bini et al., 2008; Pranzini, 2001). However, our work also suggests that sediment load may have had an opposite trend in the last decade, as shown by the analysis of fluvial

discharge analysis, with a slight increase in the number of events higher than 700 m^3/s, suitable for sand transport.

As highlighted by Sentinel-2 analyses, the shape of the jetty at the river mouth also played a key role in the dispersion of sediments offshore and in the creation of shadow areas longshore. As documented in Figure 3.6 and Figure 3.7, some sediments reach the northern sector passing through an opening in the jetty (see plume 1a, Figure 3.6), but this intervention is still insufficient to limit the formation of the shadow zone in the northern sector. In this respect, it may be useful to seriously consider the maintenance/change of shape of this engineering structure, built at the beginning of the 1900s, which was supposed to avoid the silting up of the river mouth and to reduce the flood hazard that is creating significant coastal erosion problems. In more recent years, a similar crucial role has been played by the jetty at the Morto Nuovo River. It is important to reflect on the extensive use of expensive and impacting engineering defenses in this area, which do not always give the expected protection results. In some cases, the defenses have been destroyed by coastal erosion as documented by Pranzini et al. (2018), and in other cases the defenses have shifted the coastal erosion from one coastal sector to another (e.g., areas of the village of Marina di Pisa, where erosion and coastal defenses are moving southwards and seaward acting on the submerged profile) (Casarosa, 2016; Pranzini et al., 2018).

The possibility for the solid load to reach the coastline to counter erosion was confirmed by using a DGPS to measure a small stretch of coast in the southern sector in front of the village of Tirrenia (area C, which exhibits a general trend of stability, reached by sediments during the described events). We documented an advance by comparing the shoreline position obtained by DGPS before the event of 3 February 2019 with the shoreline measured about one month after this event. Since grain size analysis of the sediments of the riverbed and of the southern coastal area are consistent and correspond to medium sand, we can deduce that part of the southern coast receives sediments from the Arno River. Furthermore, the grain size range of the transported sediments is useful to counter erosion. On the contrary, areas A and B are affected by erosion because they are not influenced by the dispersion of the sediments of the plume under different marine weather conditions.

4 Shoreline identification method

Currently, drones are used in monitoring of many different environments and the coasts are no exception. Morphology is a very important data that is extracted from RGB images sampled with a drone and through the application of photogrammetry techniques. A very important parameter of coastal morphology is the shoreline which allows to creation chronological series of changes and an easy comparison with the data of the past. However, as far as the author knows, an objective method for extracting the shoreline position from drone-derived data has not yet been defined. In the following paragraph the methodology, the results, and the discussions about the method that this thesis wants to propose will be illustrated.

4.1 Study area

For the realization and validation of the shoreline position identification method, the UAV and Differential GPS (DGPS) surveys are executed in a littoral area of 4.5km located on the right bank of the Arno River (Figure 4.1).

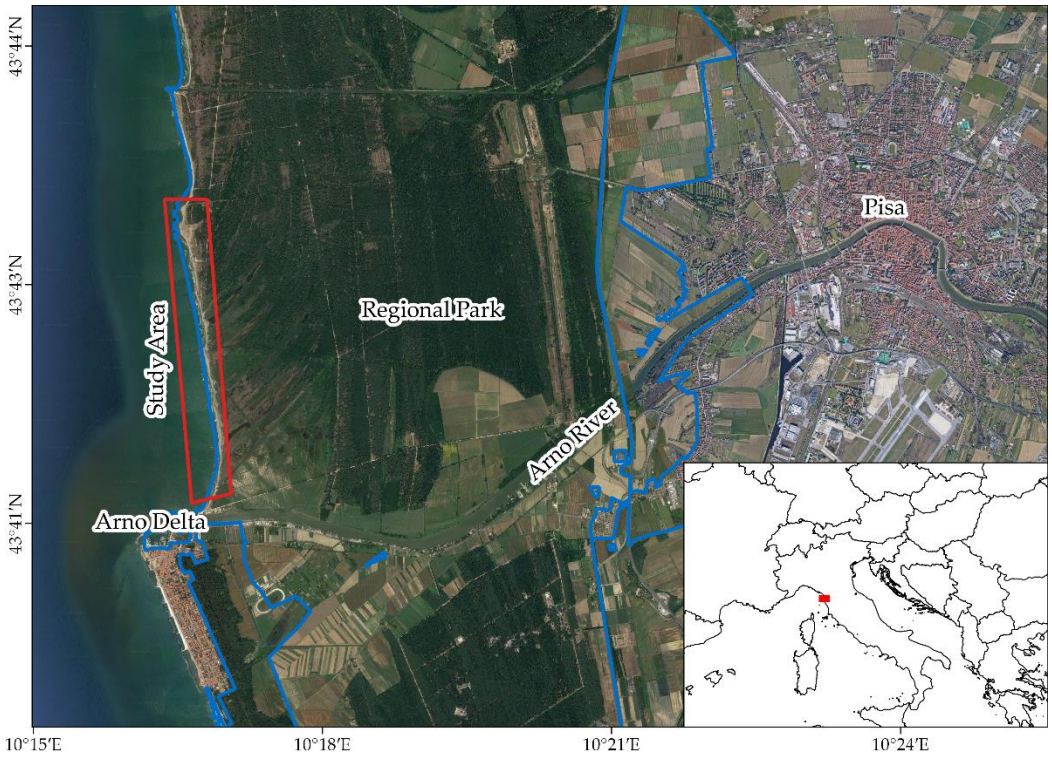

Figure 4.1 Study area

4.2 Material and Methods

4.2.1 DGPS Survay

We have sampled 224 points with a R8s Trimble real-time kinematic (RTK) DGPS. The 224 points were divided into 112 pairs, so that the shoreline was sampled by taking a point in the water and a point on the land where the waves ended (Pranzini and Simonetti, 2008). Sampling took place in calm waters. We built the shoreline starting from DGPS points and we designed an appropriate algorithm able to automatically place the shoreline between the two points (one towards land and the other towards sea). The operations of this algorithm are illustrated in Figure 4.2. Positioning of the shoreline depends on the elevation of the two investigated DGPS points. In case one point has a negative elevation and the other point has a positive one, the algorithm makes a linear interpolation between the two acquired points. It selects the point with 0 m of elevation (coordinate z) among the interpolate points and it derives the x and y (latitude and longitude) coordinates of the shoreline from this point. In case both points have positive (or negative) elevations, the only difference is that the algorithm selects along the topography profile the point (latitude and longitude) with the coordinate z equal to the mean altimetry of two DGPS points investigated from this point (Figure 4.2). With this algorithm, we assume AMSL using the elevation of the DGPS points. When the 0 m AMSL is included in the topography profile, we consider this altimetry as the most representative of the interface between water and land. When the 0m AMSL is not included in the topography profile, we must choose another AMSL altimetry. In such case, we believe that the best representative altimetry is the mean elevation between the two extremes of the profile (one towards land and the other towards sea).

After the identification of all the 112, points of shoreline, we drew the polyline representing the boundary between water and land.

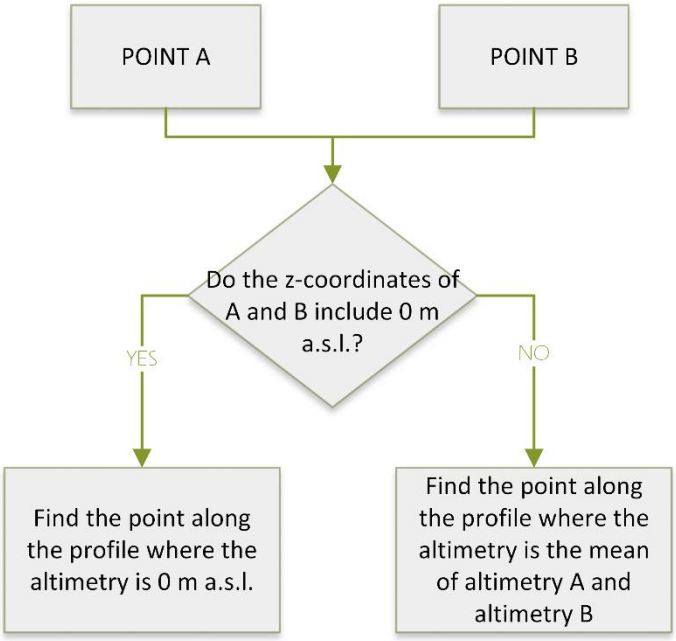

Figure 4.2 Flowchart of the algorithm designed for identification of the shoreline using differential GPS (DGPS) points

4.2.2 UAV Survey

SfM is a photogrammetric technique which allows to reconstruct 3D models starting from a collection of photos of the same elements obtained from different viewpoints (Favalli et al., 2012; Lowe, 2004; Westoby et al., 2012). The frames are sampled by means of an Unmanned Aerial Vehicle (UAV) equipped with a consumer-grade camera. In particular, we used DJI Phantom 4 Pro V2, which is a quadcopter with a flight autonomy of 30 minutes. The FC6310S camera was able to take photos of 5472 × 3648 pixels (in a 3:2 aspect ratio setting). All acquisitions were obtained with a 24 mm focal length and camera oriented in orthogonal mode with respect to the ground.

The flights were in automatic mode and reached a maximum distance of 500 m from the pilot (as required by the Italian regulatory system), making it possible to perform 1 km sections for each flight.

All flight plans were created using the Desktop UgCS (Universal Ground Control Station) software and were performed using the UgCS application for Android OS. The "Area scan" function allowed us to set the parameters so as to obtain a flight height of 50 m above ground level (AGL) and an overlap of the acquired photos equal to 75% for each side. By using this flight height, we were able to scan a 75 × 50-meters area for each photo. Image acquisition was directly controlled by the flight execution software, UgCS for DJI (Android version); the shooting interval was set to 2 seconds, the manual focus to infinity, while disabling

the autoexposure, and storage format was JPG. Four parallel transects were performed for each flight, to obtain a mapping of 1000 × 70 m with the yaw of the drone constantly set at the same angle with respect to the Earth's North. Georeferencing of the 3D model obtained through SfM requires the identification of the ground control points (GCPs) which coordinates are sampled using DGPS. We positioned 45 GCPs in the 4.5km of the investigate area.

The investigated coastline (area A1 in Figure 3.1) of about 4.2 km was divided into four flights of UAV. We chose to divide the area into four flights for two technical reasons: the first one is the autonomy of UAV of about 15 minutes; the second reason was linked to the size of the DEM and of the orthophotos resulted. Very large grids are difficult to manage and process.

4.2.3 Data Processing

We processed the photos and GCPs by using Metashape Professional software (Agisoft LLC, St. Petersburg, Russia), which implements SfM and multi-view stereo matching algorithms.

The first step in the standard workflow by Metashape Professional is to upload a set of images and to evaluate their quality. Metashape Professional finds correspondence points between overlapping images. It estimates the camera position for each photo and creates a scattered point cloud model. When available, the GCPs are identified in the images, and their coordinates are entered. GCPs are typically used as control points to optimize camera position and orientation data, making it possible to obtain better model reference results. The next step is to create a dense point cloud based on the estimated positions and parameters for each camera. Finally, a DEM and an orthomosaic are calculated with pixel dimensions that depend on the average resolution of original image terrain sampling.

4.2.4 Shoreline Identification algorithm

To extract the shoreline from DEMs and orthomosaics, we identified a new semi-automatic method based on the beach profile by the SfM technique. The method is based on the principle that SfM performs poorly on uniform or reflecting surfaces like the sea (Kohv et al., 2017). The beach profiles obtained with SfM are more irregular and unrealistic on sea, becoming regular and realistic when the points are referred to the land. By exploiting this principle, we used an algorithm that sought the transition point between an irregular profile (sea surface) and a more regular profile (beach). The algorithm is based on the use of transects along

the beach. The transects must have an orientation from the sea to land. The profile of the transect, which includes the surface of the sea, will be characterized by a low coefficient of determination (R^2; Figure 4.3), moving from the sea towards the beach and gradually discarding part of the transect profile, which will be regularized until it includes only and exclusively the beach profile. When the profile has an R^2 greater than or equal to a determined threshold, the algorithm stops and identifies the point of coordinates closest to the sea (Figure 4.3).

We developed a QGIS v3.x plugin in Python 3 to make the algorithm available to the scientific community working in the field. The plugin can be downloaded using the official repository of QGIS and is called *"Shoreline Identifier"*

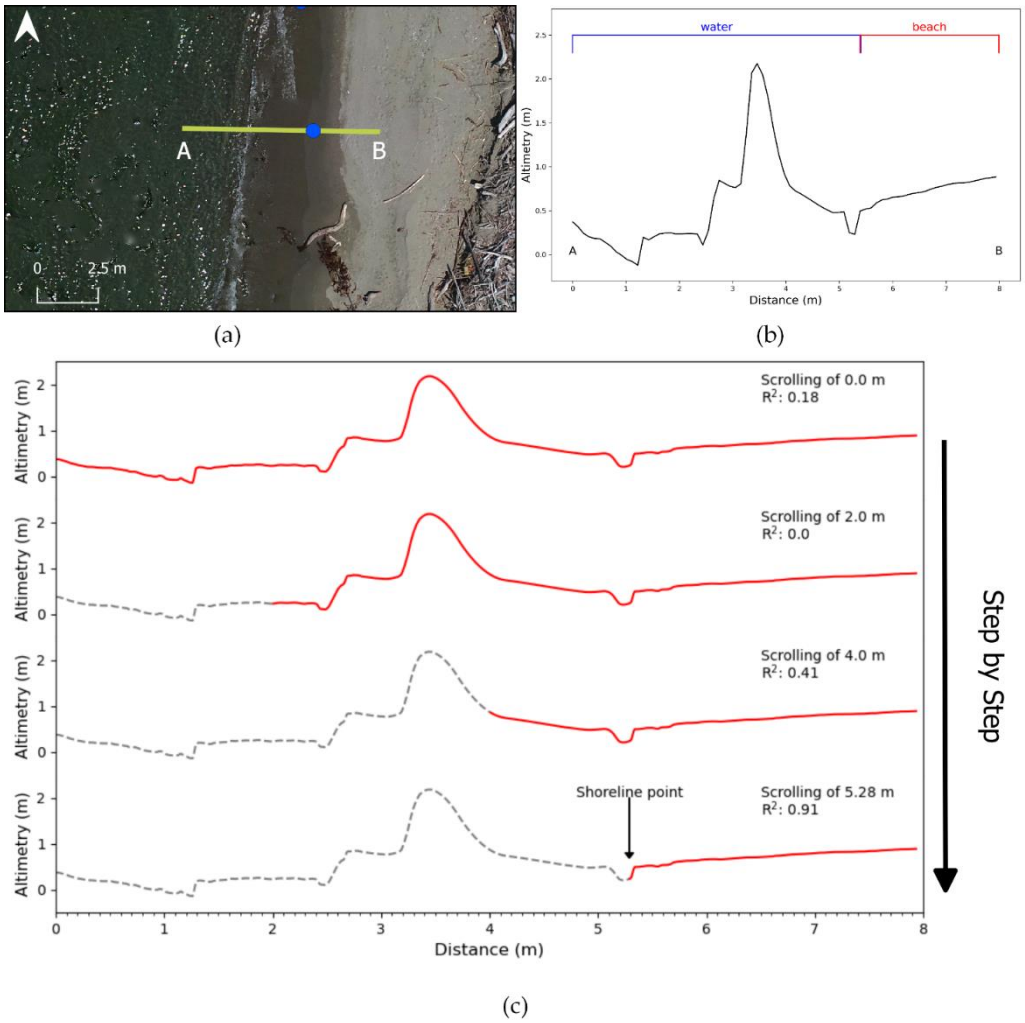

Figure 4.3 Description of shoreline identification from the Unmanned Aerial Vehicle (UAV) orthomosaic and Digital Elevation Model (DEM). (**a**) The location is a typical transect oriented from sea to land (yellow line). The blue point represents the local attribution of the shoreline by an algorithm; (**b**) profile on DEM from SfM of the investigated transect; (**c**) four illustrative steps of the algorithm to find the shoreline point. R^2 is calculated only on the part of the profile coloured in red. The grey dashed line represents the progressive part of the profile discarded by the algorithm (after Luppichini et al., 2020, modified).

4.3 Results

The main parameters of the four UAV surveys are reported in Table 4.1. The RMSE between the coordinates of the GCPs and their calculated position in the Metashape models appears in Table 4.2. The model with the highest error is model 1 with 15 GCPs on a coverage area of 0.15 km^2. The model with the least number of GCPs is the model 4, which is the smallest in terms of coverage area. The DEM resolution is of 2.79 cm/pix for model 1; 2.56 cm/pix for model 2; 2.72 cm/pix for model 3, and 2.67 cm/pix for model 4.

Table 4.1 Main parameters of the four UAV surveys.

Model	Number of Images	Flying Altitude (m)	Ground Resolution (cm/pix)	Coverage Area (km^2)
1	361	45.3	2.79	0.15
2	341	42.3	1.28	0.128
3	367	38.3	1.36	0.111
4	561	29.3	3.48	0.060

Table 4.2 Root-mean-square error (RMSE) between the coordinates of the GPS control points and their calculated position in the Metashape models.

Model	Number of GCPs	X RMSE (cm)	Y RMSE (cm)	Z RMSE (cm)	XY RMSE (cm)	Total RMSE (cm)
1	15	1.25	0.91	5.65	1.55	5.86
2	15	0.96	0.82	4.61	1.26	4.78
3	9	1.73	0.60	3.35	2.83	3.82
4	6	0.61	0.19	3.33	0.64	3.39

The development of the algorithm for identification of the shorelines on the basis of topography led to the use of an R^2 threshold above which there is a transition from a profile containing the sea to an exclusive land. During each step, the algorithm makes a shift along with the coast profile of 0.001 m.

Figure 4.4 shows three frames of the shorelines obtained with DGPS points and UAV image processing. The two shorelines are different, but it is difficult to claim whether one is better than the other. The DGPS-derived shoreline in Figure 4.4a approximates the real shoreline better than the UAV-derived shoreline. However, in Figure 4.4c, the behaviour is opposite, and in Figure 4b the two shorelines approximate the real shoreline better alternating.

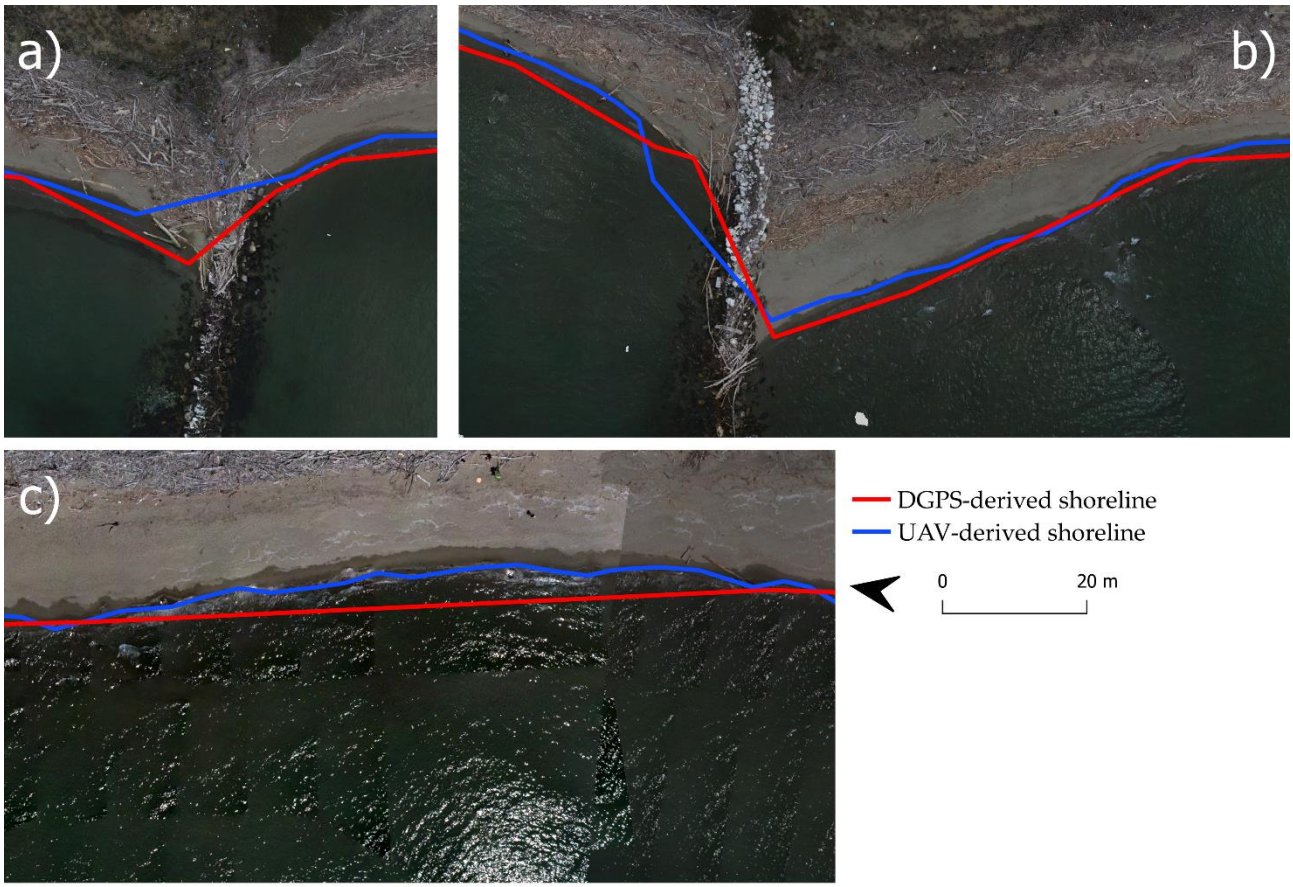

Figure 4.4 Shorelines derived from DGPS (red line) and from UAV image processing (blue line). a) The DGPS-derived shoreline (red line) approximates the real shoreline better than the UAV-derived shoreline (blue line); b) the two shorelines approximate the real shoreline better alternating; c) the UAV-derived shoreline (blue line) approximates the real shoreline better than the DGPS-derived shoreline (red line; after Luppichini et al., 2020, modified).

4.4 Discussion

We evaluated a new method to extract UAV-derived shorelines by comparing the location distance of coastline points along the 112 transects derived from the DGPS points used to realize the coastline that we considered the most flawlessly obtainable. To apply the method, we had to locate transects orthogonal to the beach. Figure 4.4 shows the distances between the relative points of shoreline derived from DGPS and those derived from UAV images. We needed about 8 transects every 100 meters to obtain a minimal error between the two types of shorelines (Figure 4.5). The minimal mean error with more than 12 transects/100 m is 1.58 m. The number of transects necessary to obtain a precise shoreline is also influenced by the coastline profile; for example, a more irregular coastline needs a greater number of transects. The use of UAV images to extract a shoreline allows you to decide the number and position of transects after the survey. This is not possible when we build the shoreline by using DGPS points: We have to decide the number and the location of point pairs during the sampling phases.

Figure 4.6 shows the differences in terms of areas by comparing the DGPS-derived with the UAV-derived shoreline. The orange polygons represent the total area when the DGPS-derived shoreline is less seaward than the other shoreline. The blue polygons show the total area, when the DGPS-derived shoreline is more seaward than the other shoreline. The shoreline derived from the UAV images is closer to the beach than the shoreline derived from the DGPS points (Figure 4.6b). In other words, the UAV-derived shorelines overestimate the mainland compared to the DGPS-derived shorelines. In some cases, equal to about 30% of the total investigated area, the UAV-derived shorelines underestimate the mainland compared to the shoreline derived from DGPS (Figure 4.6b).

The RMSE between the DGPS shoreline and the UAV-derived shoreline using 12.8 transects/100 m is 1.69 m, much lower than the methods involving the analysis of satellite images, whose order fluctuates between 6 and 12 m depending on the techniques and images used (García-Rubio et al., 2015; Sánchez-García et al., 2015; Vos et al., 2019a).

Figure 4.4c shows the main errors that occur when using DGPS points to build the shoreline. The samplers misinterpolated this stretch of beach by taking an insufficient number of points. The result is a too simplified shoreline, which is a typical error when using DGPS to create a topography profile. Once data have been sampled, there is unfortunately no possibility of correcting this simplification. On the contrary, in the case of UAV-derived shorelines, we can improve the approximation of the real shoreline by increasing the number of transects. This operation is not linked with the sampling phase of the data, and therefore, it can be applied at any time.

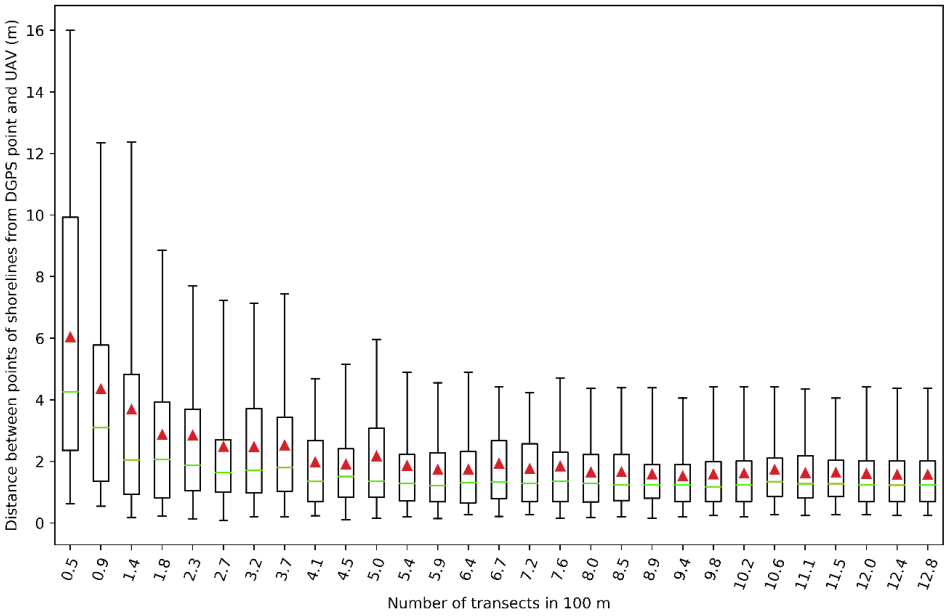

Figure 4.5 Analysis of errors between shoreline points derived from DGPS points and those derived from DEM by Structure from Motion (SfM) processing. The errors are the distance between two relative points of shorelines along 112 transects derived from DGPS points. The box represents the 25th and 95th percentiles, the green line the median, the red triangle the mean, and the whiskers the 5th and 95th percentiles (after Luppichini et al., 2020, modified).

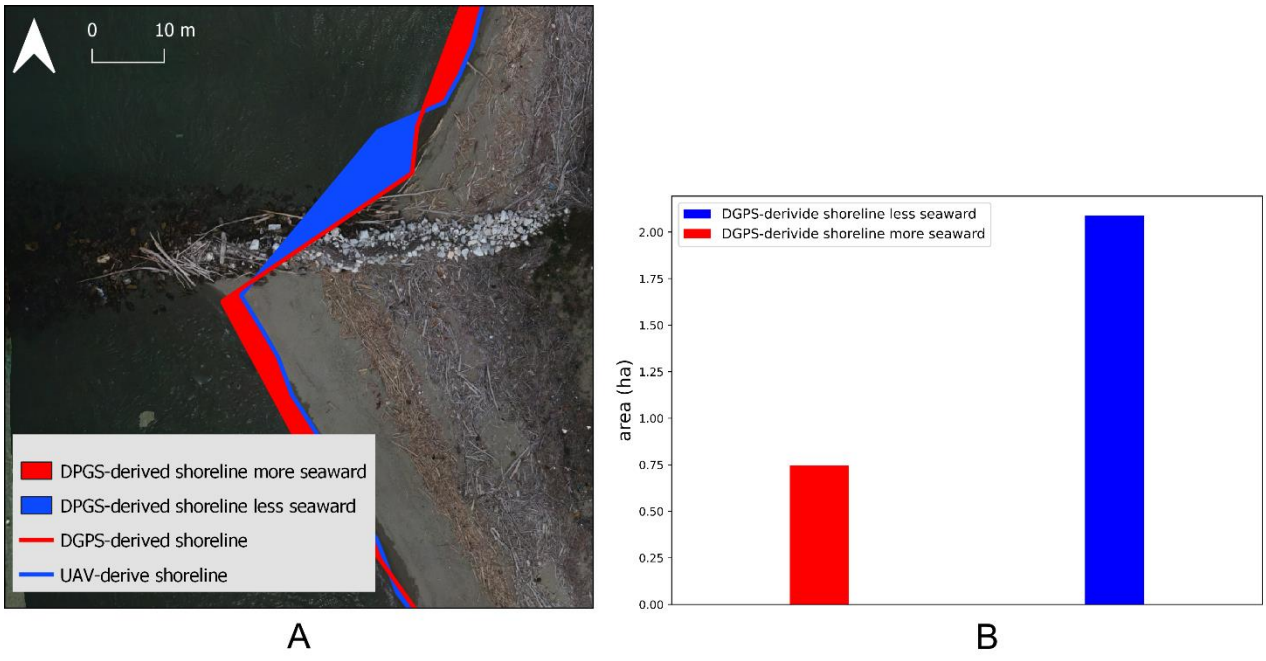

Figure 4.6 Analysis of the differences between DGPS-derived shorelines and UAV-derived shorelines. (**a**) Example of the differences in the areas between DGPS-derived shorelines and UAV-derived shorelines; (**b**) bar plot of the different areas of the beach comparing the two types of shorelines. The blue and the orange rectangles show the total area when the DGPS-derived shoreline is more or less seaward compared to the other shoreline obtained from UAV images (after Luppichini et al., 2020, modified).

5 Deep learning models to predict flood events

Flood events are one of the main hydrogeological phenomena closely linked to global warming due to their ability to modify the rainfall regime, especially in extreme events. This entails the need to have models capable of predicting flood events, also increasing their warning time. In recent years, artificial intelligence techniques have been applied in various contexts of geosciences including also in the prediction of river flow regimes. This study aims to apply these methods in a context characterized by short run-off times. The study is conducted in the Arno River basin, the main hydrographic basin of Tuscany.

5.1 Material and methods

5.1.1 Arno River Basin

The Arno River basin (Figure 5.1) is approximately 8300 km^2 wide, the fifth in extension in Italy, and is bordered by the Apennine chain from north to east. The average and maximum elevations are about 350 and 1600 m a.s.l., respectively. The Arno is the main river in Tuscany and one of the longest (240 km) in Italy. Thus, flood forecasting is strategic in the Arno River basin, since the river crosses the two main Tuscan cities of Florence and Pisa, as well as many production centers. Figure 5.1 also shows the location of the hydrometric stations used in this study, whereas Figure 5.2 shows the digital terrain model (DTM) and the slope of the basin.

Owing to its geological, geomorphological and morphometric features, the Arno River basin is characterized by a general relatively short run-off time. However, different sectors of the river characterized by different run-off times can be recognized: in the mountainous hilly area, the run-off times range from 4 to 6 hours, whereas in the lowland areas the run-off time is ca 20-24 hours approximately (Autorità di Bacino del Fiume Arno, 1989). This behaviour is interesting to understand whether the applied methodology has limitations when the basin run-off times are short.

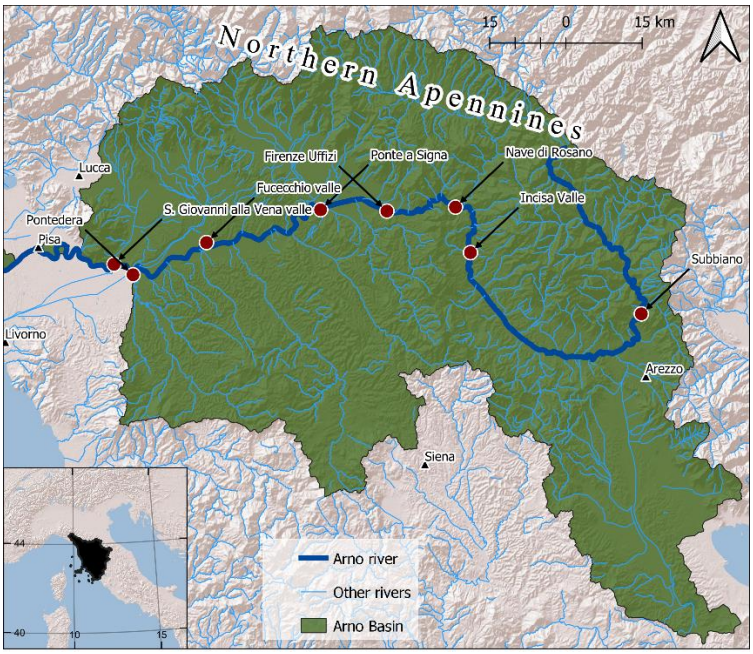

Figure 5.1. The Arno River basin and its main drainage network.

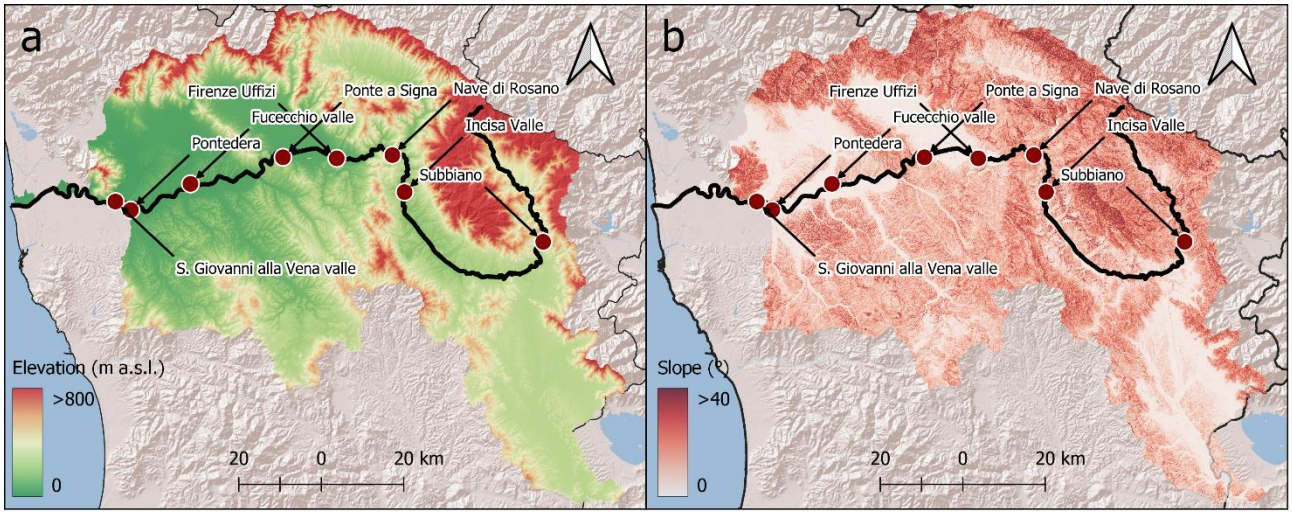

Figure 5.2. Morphological characteristics of the Arno River Basin: a) 10×10m DEM provided by the Tuscany Region (https://www.regione.toscana.it/-/geoscopio); b) grid of the slope obtained from DEM. The red dots identify the eight hydrometric stations used in this work (after Luppichini et al., 2022, modified).

5.1.2 Database and data input pre-processing

The dataset used (provided by the Regional Hydrologic Service, hereafter SIR), comes from a very rich monitoring network that includes 487 raingauges and 193 hydrometers (Figure 5.3), with a sampling time of 15 minutes. For our models, we selected the most complete time series using 48 raingauges and 35 hydrometric stations for the decade 2010-2020. The 15-minute sampling time allowed us to better describe the phenomena that develop over a short time span. Indeed, a low sampling frequency could lead to run-off

and rainfall curves that do not adequately represent the natural phenomenon. From this point of view, deep learning models are capable of reproducing these curves, resulting to be precise but not very accurate. On the other hand, the high frequency of sampling involves an increase of the noise in the data that could create errors in the models. In our case, we have no noise signal in the data, and for this reason we have chosen to use the maximum resolution available for the study area. In our study, we wanted to get as close as possible to the real phenomenon by limiting simplifications in the flow or in the rainfall curves.

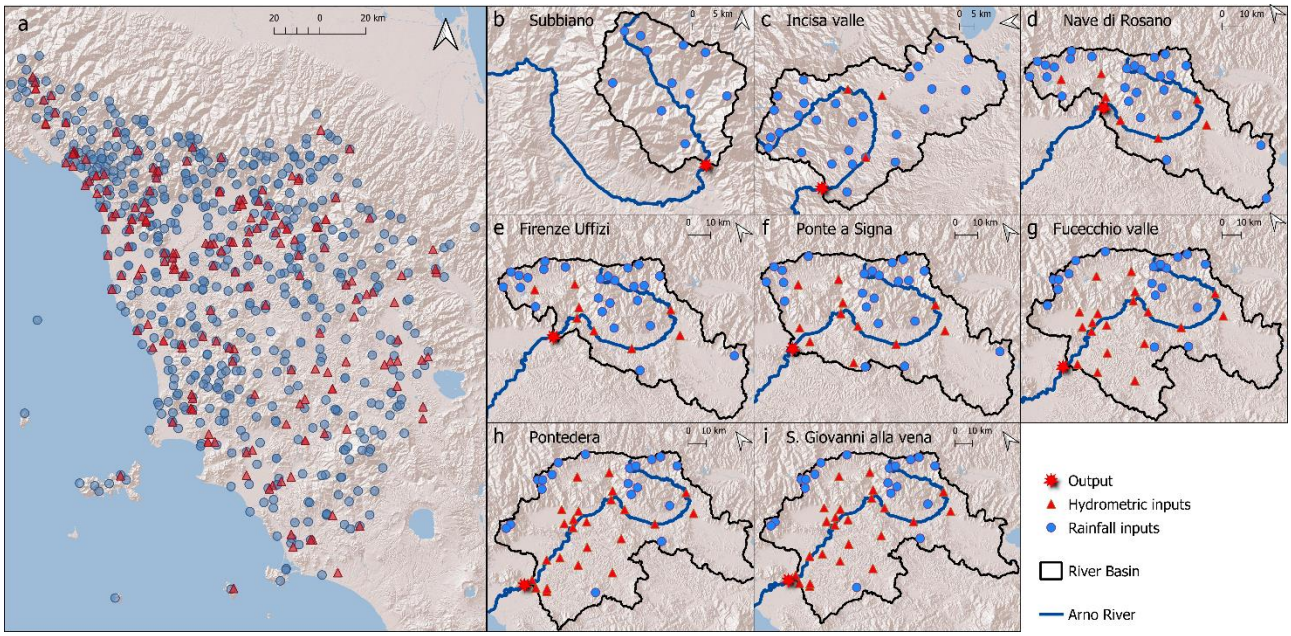

Figure 5.3. a) Monitoring network of SIR (15-minute sampling frequency; source: https://www.sir.toscana.it/consistenza-rete). The blue circles represent the rainfallgauges and the red triangles represents the hydrometers. b-i) Distribution of output hydrometers (red stars), input hydrometers (red triangle) and raingauges (blue circle) in the 8 sub-basins simulated in this work (after Luppichini et al., 2022, modified).

For our purposes, the Arno River basin was divided into eight sub-basins closed at specific hydrometric stations, which were used as model outputs. From upstream to downstream, we selected the following hydrometric stations: Subbiano, Incisa valle, Nave di Rosano, Firenze Uffizi, Ponte a Signa, Fucecchio valle, Pontedera and S. Giovanni alla Vena (see Figure 5.2). They were chosen for having almost complete time series with a small number of missing values, and for being in strategic positions for monitoring of the river. The stations of Subbiano, Incisa Valle, and Nave di Rosano are positioned upstream of the city of Florence, thus allowing to predict flood events upstream of the city of Florence. Firenze Uffizi station is a key to understanding the hydraulic behaviour of the river in the most important city of Tuscany. Ponte a Signa station is near a large flood reservoir, whereas the Fucecchio valle station provides information on the

hydraulic behaviour of the river in a completely flat area. Pontedera station is near the Scolmatore Canal, an artificial canal built after the 1966 flood in order to protect Pisa (the second main Tuscan city crossed by the Arno River) from flooding. The Scolmatore Canal drains the waters of the Arno River directing them towards the sea. S. Giovanni alla Vena station is the nearest one upstream to Pisa. Figure 5.4 shows the hydrometric and rainfall stations used for each sub-basin model. We chose the input stations according to their datasets and geographical positions. This choice was made to obtain a homogenous distribution of station in each sub-basin. Table 1 lists the characteristics of each modelled sub-basin and the relative stations considered. For each sub-basin, Mean Annual Precipitation (MAP) and Mean Annual Temperature (MAT) were computed by using the 1920-2020 data on the basis of the meteorological stations indicated.

Table 5.1. Features of each modelled sub-basin and of the stations used (MAP: Mean Annual Precipitation; MAT: Mean Annual Temperature and relative standard deviation - Data from 1920 to 2020).

Output Hydrometric Station	Sub-basin area (km^2)	Sub-basin average elevation (m a.s.l.)	n. input raingauges	n. input hydrometers
Subbiano	750	750	11	0
Incisa Valle	2,840	580	28	3
Nave di Rosano	3,840	460	26	8
Firenze Uffizi	3,970	450	25	9
Ponte a Signa	4,540	430	22	12
Fucecchio	6,600	370	19	20
Pontedera	7,850	340	14	30
S. Giovanni alla Vena	8,030	320	19	25

For each output hydrometer, we built a deep learning model to predict its 15-minute measurements (H_t). The mathematical expression of the model, representative of all the investigated sub-basins, can be defined as follows:

$$\widehat{H} = f(X_t) = f(H_{t-1}, H_{t-2}, \dots, H_{t-n}, R_{t-1}, R_{t-2}, \dots, R_{t-m}) \quad (13)$$

where $\widehat{H}$ stands for the predicted hydrometric height at time *t*; $H_{t-1}, H_{t-2}, \dots, H_{t-n}$ are the antecedent hydrometric heights (up to *t*–1, *t*–2, …, *t*–*n* time steps); $R_{t-1}, R_{t-2}, R_{t-m}$ are the antecedent rainfall (*t*–1, *t*–2, …, *t*–*m* time steps).

Some tests and trials highlighted the need to create an input dataset with *t* up to 96 steps. To decrease the noise contained by many steps and close measurements, we provided every *t* for the first previous hour and then one every 4 steps (e.g., *t*-0, *t*-1, *t*-2, *t*-3, *t*-4, *t*-8, *t*-12, *t*-16, ..., *t*-96) up to the 24th hour.

The evolution of the riverbed influences the hydrometric measurements. Since a hydrometer measures the flow heights relative to a fixed point over time, sediment deposits near the hydrometer cause the measured value to be higher than the correct value (systematic error). On the contrary, the riverbed erosion causes a measurement lower than the correct one. For this reason, we could observe negative values of hydrometer measures or a progressive movement of the minimum annual level of the river. Furthermore, measurement errors could occur, inducing inconsistencies and incoherence in the dataset. These problems of hydrometric measurements are summarized in Figure 5.4 (grey line), which shows that the past year presents the highest minimum flow of the river and that there are some errors when measurements are equal to 0. For this reason, we normalized the hydrometric measurements for each time series used by removing the incorrect data and standardizing the measurements and then comparing the minimum measured each year with the last one (Figure 5.4, blue line).

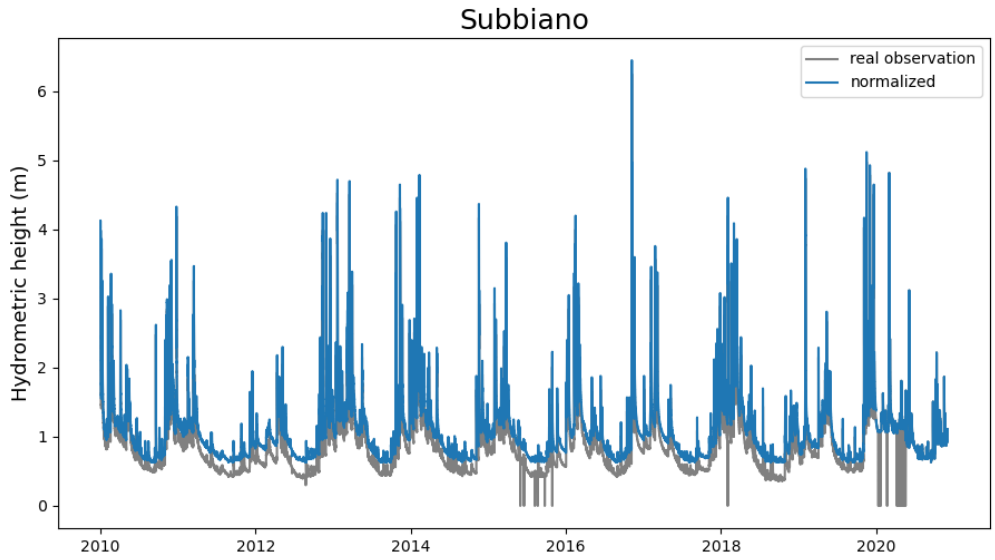

Figure 5.4. Standardization of a hydrometric height time series (the example is refered to the Subbiano station). We removed all fake data and calculated the minimum river level value that was stationary over time each year (after by Luppichini et al., 2022, modified).

5.1.3 Model development

To accomplish the deep learning models of this study, we mainly used the open-source framework Tensorflow (Abadi et al., 2015) and the libraries Numpy, Pandas, Scikit-Learn and Keras (Chollet, 2015) in Python language v 3.7 (van Rossum and Drake, 2009). The architecture of the developed models is based on an encoder-decoder LSTM, formed by two pairs of LSTM nodes (Figure 5.5). This architecture allows usage of an LSTM to read the input sequence, one step at a time, in order to obtain a fixed-size vector representation in a data structure that occupies a large amount of memory. We then introduced another LSTM to extract the output sequence from that vector (Sutskever et al., 2014). The encoder is composed of two sequence layers (LSTM) of 32 and 16 units, respectively, followed by a repeat vector node. The repeat vector layer repeats the incoming inputs for a specific number of times. The decoder is composed of two LSTM layers of 16 and 32 units respectively, followed by a time-distributed dense node as output of our model. To evaluate the discrepancy between the predicted and the measured values, we used a loss function for each observation, which allowed us to calculate the cost function. We needed to minimize the cost function by identifying the optimized values for each weight. Thanks to multiple iterations, the optimization algorithm computes the weights that minimize the cost function. In our implementation, we used the Adam optimizer (Kingma and Ba, 2014). Adam is an adaptive learning speed method, meaning that it computes individual learning rates for several parameters (Kingma and Ba, 2014). To stop the training, we used the specific API of Keras and, in particular, the early stopping method. This method allows the training procedure to stop when the monitored metric, namely the value of the cost function, has ceased to improve. Therefore, given all the possible hypotheses, we wanted to find the best one (called “optimal”). This hypothesis would make it possible for us to make more accurate estimates, still based on the data available. We split the dataset into three parts: training, validation, and test dataset (Figure 5.5). The training dataset includes the 2010-2017 data, and represents the input in the learning step. The validation dataset is composed of the 2017-2019 data and is used to calculate and optimize the loss function in the learning phase. Finally, we used the test dataset (2019-2021) to evaluate the final model: the prediction step allowed us to forecast the hydrometric heights of the river because these data are unknown to the model. This partition of 60% - 20% - 20% for training, validation and test dataset is used by several studies (e.g., Hu et al., 2020; Li et al., 2020; Nguyen and Bae, 2020) and permits to have sufficient data for the training and the evaluation of the

model. In detail, Li et al. (2020) use a similar subdivision of the dataset considering only one year for validation and for the test dataset.

The cost function used was the mean square error (MSE) calculated on the validation dataset. The partition of the whole dataset permitted to minimize the overfitting effect on the training set. We built a model for each hydrometric station and 25 forecasting steps for a total of 200 models considering the eight sub-basins modelled. The forecasting steps are one every hour from 0 to 24 hours.

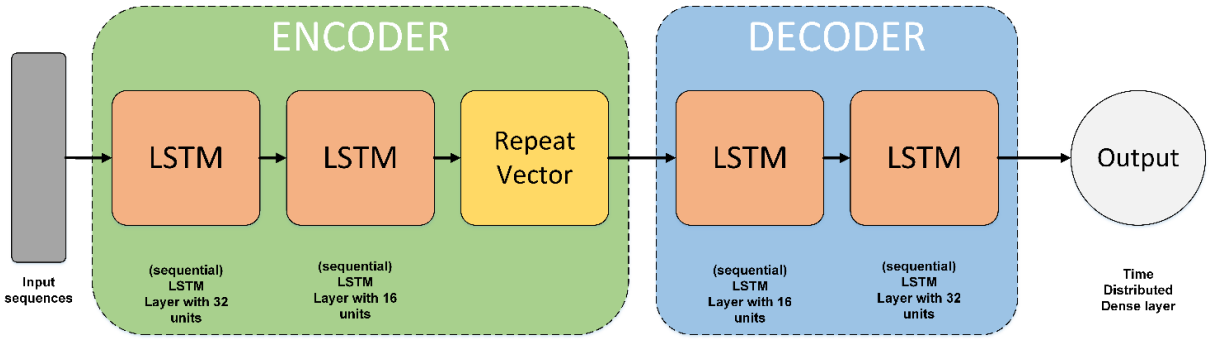

Figure 5.5. Architecture of the deep learning model used in this study, based on the use of the LSTM node.

5.2 Results

We evaluated the accuracy and precision of the models by analyzing the model errors when predicting the maximum effects. For each station, Figure 5.6 shows the prediction accuracy of the 30 highest events occurred in 2019 and 2020, highlighting the absolute error, i.e., the difference between the predicted value and the observed value. We also computed the relative error by dividing the absolute error by the measured value. We partitioned the results into four groups: 0-6 h, 7-12 h, 13-18 h and 19-24 h. In all cases, we can observe that the longer the forecast time, the greater were the errors. Furthermore, the percentage errors were higher for the upstream than for the downstream stations (Figure 5.6).

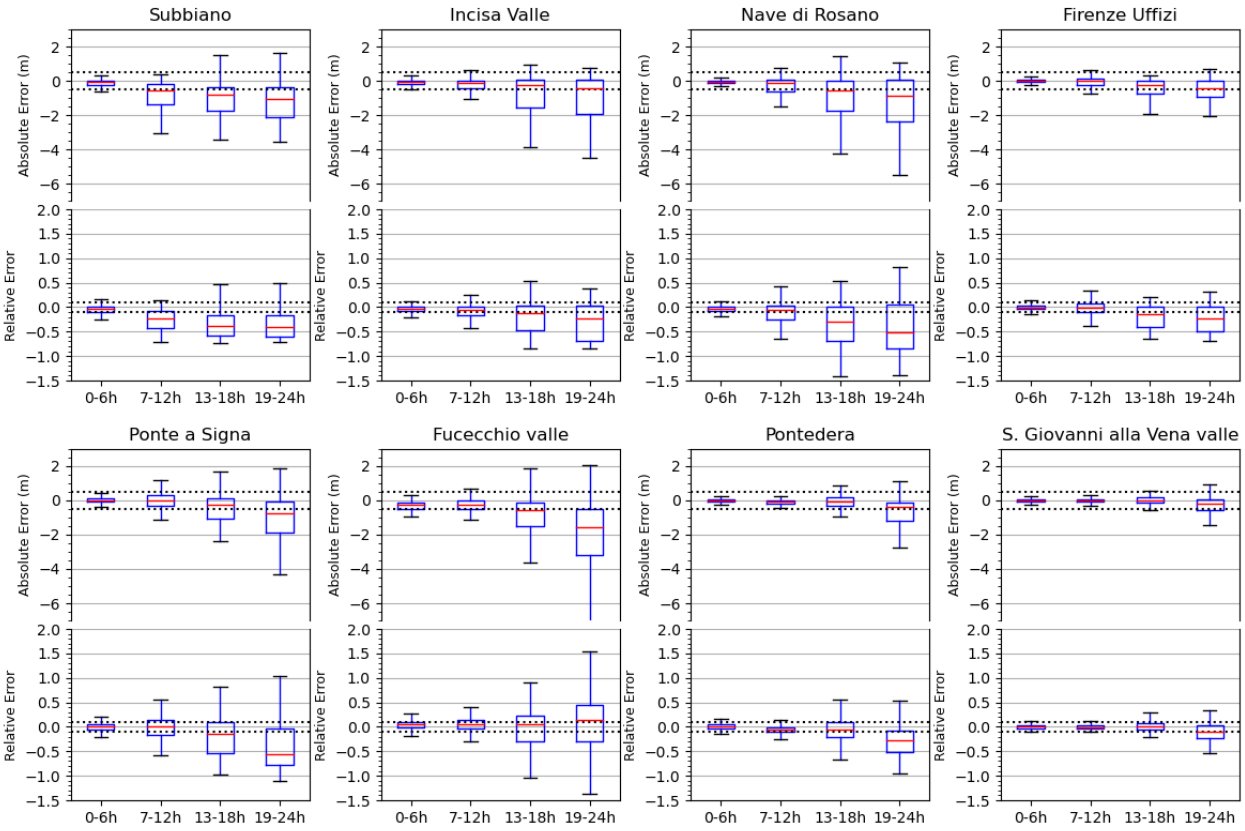

Figure 5.6. Absolute and relative model errors for the 30 most severe events occurred between 2019 and 2020 (test dataset). In absolute error graphs, the dotted lines mark the range between -0.5 and +0.5m. In relative error graphs, the dotted lines mark the range between -0.1 and +0.1. The boxes represent the interval between the 25th and the 75th percentiles (Q1 and Q3). IQR is the interquartile range Q3-Q1. The upper whisker will extend to the last datum lower than Q3 + 1.5*IQR. Similarly, the lower whisker will reach the first datum higher than Q1 – 1.5*IQR. The green lines represent the medians (after Luppichini et al., 2022, modified).

Figure 5.7 and Figure 5.8 show two events occurred on 3rd March 2020 and 17th November 2019, respectively, and representing examples of the behaviour of the Arno River during flooding episodes. Both events triggered a flood warning and the exceeding of the alert thresholds for the whole course of the river. Specifically, the event of 17th November 2019 is of considerable importance: in the 10-year time series used to train the model, there is only one other case similar to that of 17th November 2019 (see Figure 5.8). The rainfall (ca 40 mm) fell from 2020-03-02 06:00 to 2020-03-04 00:00 on the basin of San Giovanni alla Vena. Instead, the event of 17th November 2019 was characterized by ca 65 mm of rainfall that fell on the same basin from 2019-11-16 12:00 to 2019-11-17 12:00. For this reason, we can consider the two cases as representative of an ordinary alert event (3rd March 2020, Figure 5.7) and an exceptional alert event (17th November 2019, Figure 5.8).

The figures show a first prediction (blue line), which started when the rainfall over the entire Arno River basin began to increase. The subsequent forecasts were temporally spaced 6 hours from each other. Each prevision lasted for 24 hours after the start. Prediction errors mainly depend on two factors: the location of the hydrometric stations, and the time interval between the start of the forecast and the instant of time when the level reaches its maximum value. The simulations carried out just before the onset of the rainfall event (blue line) or before the maximum values of cumulative rainfall on the river basin are characterized by the higher errors, with an impossibility for the model to simulate the flow event (Figure 5.7 and Figure 5.8). The errors are lower for the simulation temporally close to the maximum flow event. When comparing Figure 5.7 and Figure 5.8, the errors are higher in the second case, when the hydrometric heights of the river are greater.

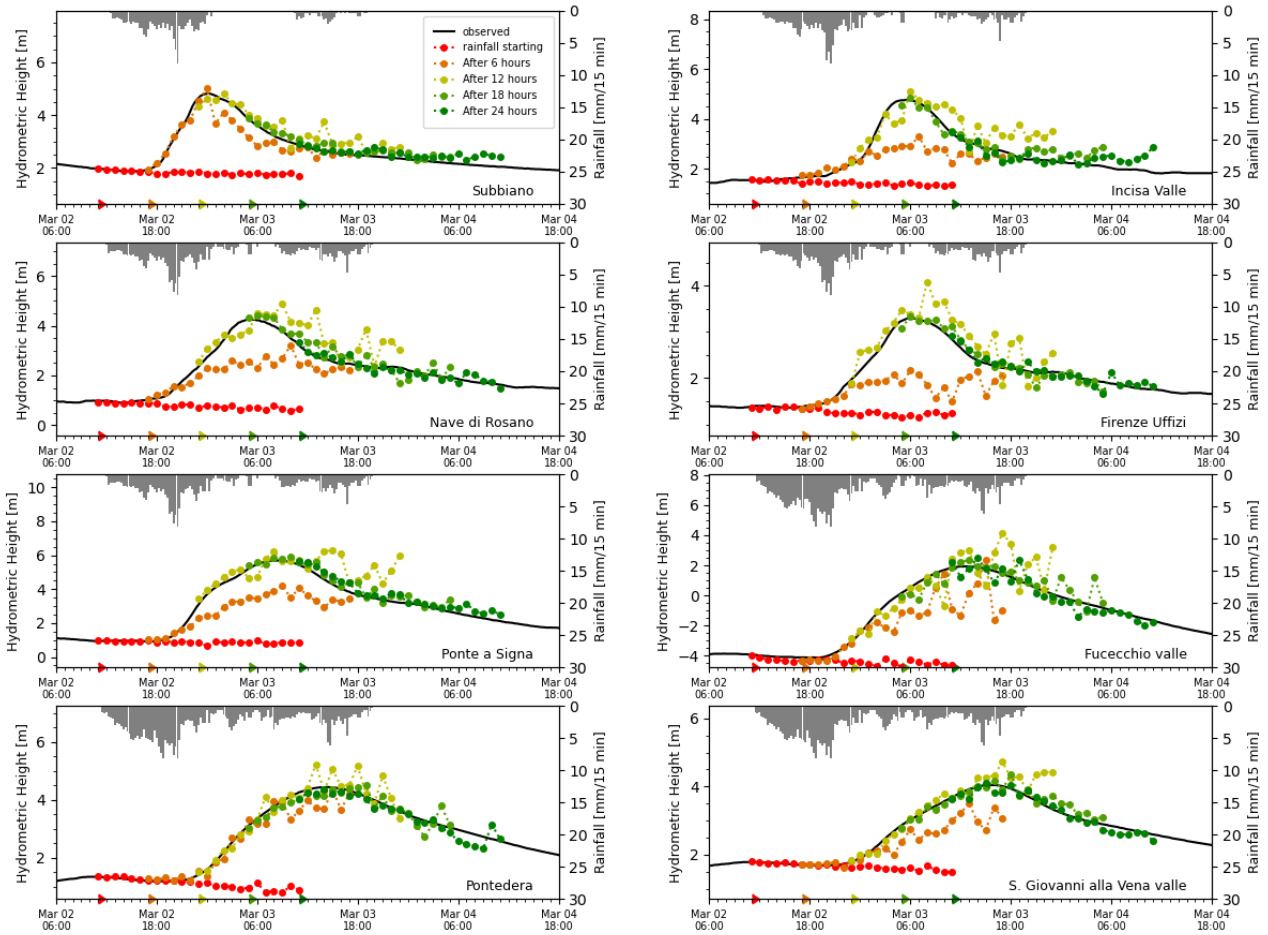

Figure 5.7. Simulation of the 3rd March 2020 event, where the hydrometric level exceeded the alert threshold in all stations. The first forecast (red line) begins when the rainfall on the Arno river basin increases. Subsequent predictions are temporally spaced 6 hours one from the other, each lasting 24 hours. The coloured triangles on the time axis indicate the start of each prediction. The grey bars indicate rainfall (after Luppichini et al., 2022, modified).

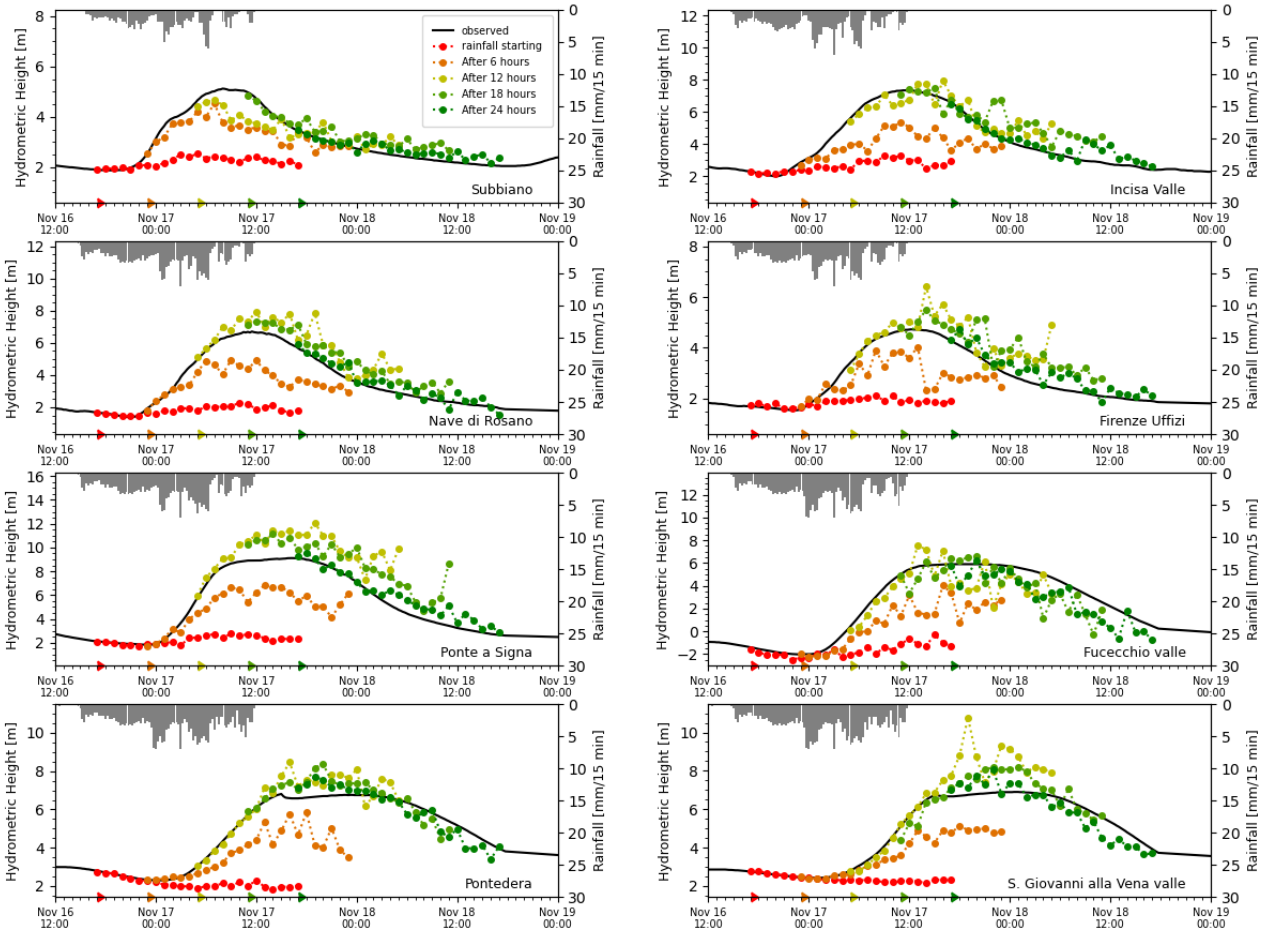

Figure 5.8. Simulation of the 17th November 2019 severe event, where the hydrometric level exceeded the alert threshold in all stations. The first forecast (red line) begins when the rainfall on the Arno river basin increases. Subsequent predictions are temporally spaced 6 hours from each other, each lasting for 24 hours. The coloured triangles on the time axis indicate the start of each prediction. The grey bars indicate rainfall (after Luppichini et al., 2022, modified).

5.3 Discussion

As a result of the high frequency of data sampling (15 minutes), we obtained a large amount of data, which allowed for efficient model learning. Model errors are influenced by the forecasting time and by the location of the hydrometric stations. The forecasts for the hydrometric stations located at higher mean elevation exhibit the highest errors. Prediction with more than 7-12 hours for this type of basin is difficult, and is characterized by high errors. The problem is reasonably due to the shorter run-off time typical of these basins. The time interval between maximum rainfall event and maximum hydrometric height is obviously variable for the analyzed stations and it characterizes the different sub-basins. The shortest interval is

associated with Subbiano (average of 13 hrs), the longest is attributable to S. Giovanni alla Vena (average of 23 hrs). Run-off times influence the capacity of the model to achieve a good prediction of the flow events.

Deep learning models are the simplest ones relatively to the data to be used and they show large flexibility at different basin scales. Their main advantage is the dynamics simplification of a run-off process by using only rainfall and hydrometric data. On the other hand, physically-based models require large amounts of different data that are sometimes very difficult to find or do not have a sufficient resolution and need specific assumptions. For example, a very low topographic resolution can cause a high error when applying a physical model (Luppichini et al., 2019) so that specific surveys are necessary. The few types of data necessary to create a deep learning model allowed us to apply it in different environmental situations. These flow forecasts are valid for the entire Arno River, from its origin to the position just before its mouth. Therefore, we think these models could be applied to watercourses with different hydraulic behaviour. For these basins, it would be useful to compare our errors with those obtained by Ercolani and Castelli (2017) which used the hydrological model MOBIDIC (*MOdello di Bilancio Idrologico DIstribuito e Continuo*). MOBIDIC is a physically-based model used by the Tuscany Region authorities for the analysis of flood alarms (Ercolani and Castelli, 2017). Even in the case of the physical model, errors are higher in basins with shorter run-off times (e.g., Subbiano and Nave di Rosano stations) and they diminish for larger basins. In that specific case, the model tends to overestimate the water flow when the warning time is several hours (greater than about 12 hours from the maximum event) (Ercolani and Castelli, 2017). Instead, the deep learning models underestimate the hydrometric heights even with high errors when the simulation is performed before the rain falls on the basin. These models do not provide any specific information helping to understand when rainfall will start and before this time, the rain is constantly equal to 0. Once the rainfall starts, our model can predict the hyetograph and understand how the hydraulic regime will evolve. The rainfall onset is a critical point in a flood warning system based on deep learning techniques. The forecast rainfall data can be made useful by implementing the classical techniques (physical models, analysis of satellite images, etc.), which can help these models overcome the current limits of these methods.

The deep run-off learning models need to use all the input stations for prediction, and this could be one of the main drawbacks of these techniques. In real conditions, one (or more) stations might not be working during a specific flood event, making a good prediction of the future flow height impossible. In cases like

those of our study area, where the monitoring network is quite dense, this drawback is overcome by creating several models based on the use of different stations. We could apply the naivest procedure by inserting the missing values of an unworking station with 0 mm (rainfall) or 0 m (hydrometric height). However, in theory, this procedure might introduce greater errors in the flood events simulation, and we could test this by changing the input data of random groups of stations with values all equal to 0, simulating the case of the missing values for the event of S. Giovanni alla Vena station. We made a simulation as if 5, 50 and 95% of the rainfall and hydrometric stations used in the model for San Giovanni alla Vena were missing. These percentages correspond to 2 non-working stations, 22 non-working stations and 42 non-working stations respectively. For each of the three tests, we simulated the predictions from 0 to 24 hrs with a step of 1 h. We repeated these simulations 10 times changing the random group of stations each time.

We calculated these errors on the 30 highest events that occurred in 2019 and 2020 (test dataset). The 30 events used to calculate the variations had a hydrometric height between 1.40 and 6.90 m. We computed the percentage variation as follows:

$$Percentage\ Variation = \frac{\overline{y_i} - y_i}{m_i} \cdot 100 \tag{14}$$

where y_i is the absolute error calculated on the difference between the measured hydrometric heights (m_i) and the predicted hydrometric heights estimated by using the real dataset; $\overline{y_i}$ is the absolute error computed by using the dataset with the simulation of missing values. The absolute errors ($\overline{y_i}$ and y_i) are calculated as follows:

$$absolute\ error = m_{sim} - m_{ob} \tag{15}$$

where m_{sim} is the result of the model and m_{ob} is the observed measure. By merging equation 1 and equation 2, we can write the percentage variation as follows:

$$Percentage\ Variation = \frac{\overline{m_i^s} - m_i^s}{m_i} \cdot 100 \tag{16}$$

where $\overline{m_i^s}$ is the result of the model with the dataset modified with the missing value and m_i^s is the result of the model with the original dataset. A reduction in percentage variation indicates a greater underestimation of the flow level compared to models with the data available. The percentage variation is influenced by the number of non-working stations (Figure 5.9). With 5% of non-working stations, the model errors increase by less than 5% for each time of prediction. A 5% underestimation corresponds to a variation

of the estimated hydrometric height of about 0.07 – 0.35 m. When the number of non-working stations is 95%, the model errors increase with an underestimation of the flow level that varies with the forecast time. The worst cases are for the greater forecast times with errors even higher than 20% (Figure 5.9). A variation of 20% corresponds to a variation of the estimated hydrometric height of about 0.28 – 1.48 m. This test allows us to observe how models can experience small increases in error when the number of non-working stations is small, but also that these errors increase greatly when the number of non-functioning stations increases significantly. In physical models, a precipitation estimate can be given by one group of stations rather than another, with results that in most cases are not significantly different. In deep learning models, which are data-driven, each station acquires greater importance and its correct management and maintenance ha~~v~~e a greater influence on the final results of the models. For the applicability of these models in alert systems for territorial management bodies, proper maintenance and management of the monitoring stations are necessary for correct flow modeling.

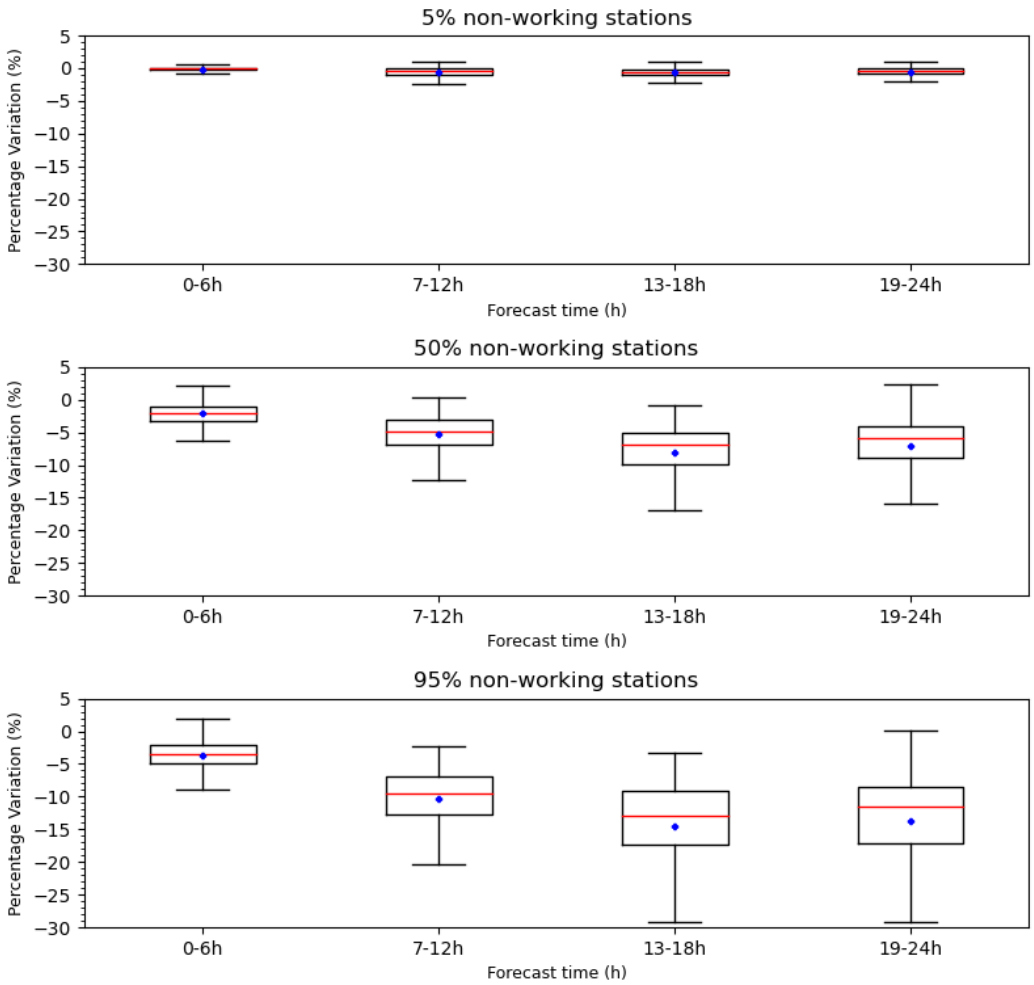

Figure 5.9. Percentage variation in the absolute error estimate of the San Giovanni alla Vena station if we consider the 30 most serious events of 2019 and 2020 by simulating a variable number of non-working stations. The box indicates the range between the 25^{th} and 75^{th} percentiles (Q1 and Q3). IQR is the Q3-Q1 interquartile range. The upper whisker will extend to the last data lower than Q3 + 1.5 IQR. Likewise, the lower whisker will reach the first datum greater than Q1 - 1.5 IQR. The red lines represent the medians and the blue points represent the means (after Luppichini et al., 2022, modified).

6 Conclusions

This study allows us to understand the effects of the current global warming on the rainfall regime in an important area of the Mediterranean. The work permits us to understand the influences of the climate changes on two important different environments in the study area: the coastal environment and the fluvial environment.

Climatologically, this study helps to gain a better knowledge of the rainfall trends of the last 70 years in Tuscany, a key area of the Mediterranean Basin strongly influenced by the cyclogenetic activity related to the Genoa Gulf Low. These trends are analyzed on the basis of the trend of the main atmospheric drivers of the northern hemisphere. The location of the study area allows to understand the influences of Atlantic atmospheric circulation and of the Mediterranean atmospheric circulation on rainfall. The rainfall amount is influenced by Northern Atlantic atmospheric circulation and by the Genoa Gulf Low. The influences of the two atmospheric systems vary during the year: in winter, rainfall is strongly correlated to the three indices; in spring, the main influence is represented by WeMO, indicating an important role played by the Genoa Gulf Low; in summer, the main driver is EA, which better represents the influence of the Azores High in this season than NAO; in autumn, the strongest correlation is with NAO.

The amount of rainfall in the study area is influenced by the SSTs which induce a variation in the Northern Atlantic and Mediterranean atmospheric circulations (Börgel et al., 2020; Frankignoul et al., 2003; Robertson et al., 2000; Visbeck et al., 2001). Current global warming determines an increase in the SSTs and this increase is higher in the warm seasons of the year (James et al., 2006). The results of this study show that in these seasons there is the greatest reduction of water availability, on account of a direct decrease in precipitation. For this reason, current global warming could be responsible for less rainfall in this area, and this occurs mainly in the warm seasons when temperature increase is highest.

On the other hand, this work investigates the relationship between temperature and rainfall highlighting global warming does not influence only the long-term rainfall regime but also the frequency of EPEs on the study area in agreement with several works (e.g., Busuioc et al., 2016; Chernokulsky et al., 2019; Formayer and Fritz, 2017; Lenderink and van Meijgaard, 2010; Pumo et al., 2018). An increase in temperature can also induce an increase in the extreme rainfall during the wet and dry seasons and considering different rain accumulation periods. Furthermore, the dry season seems to be subjected to an extremization of the rainfall

regimes with a decrease in the most frequent, the lowest rainfall events especially for the highest accumulation periods, and with an increase in the fastest and most intense rain events. This climatological study highlights the necessary to induce a variation of the territory management to mitigate the most intensive rainfall events and the drought periods.

The results on a possible increase of the EPEs linked to the global warming induce to investigate on new and efficient methods for the river flow prediction. This study demonstrates that deep learning models can be a practicable alternative to physically-based models for the forecast of flood events in basins characterized by short run-off times. The study developed deep learning models based on the LSTM network for the Arno River, one of the most important and critical Italian rivers, by using eight hydrometric stations. Unlike physically-based models, these approaches offer the advantage of using only few types of data. This feature reduces model influences resulting from the accessibility of required information, which for some watersheds can be very difficult to obtain. This advantage makes it possible to create flood warning systems in situations where hydrographic and hydrogeological knowledge is very poor, making it very difficult to obtain additional information. Conversely, these methodologies can be applied in very complex geological and geomorphological situations (i.e., karst systems, steep slopes) where, despite the considerable knowledge of the territory, it is still impossible to build satisfactory physical models. Our case study falls precisely in this case. The Arno River basin was much studied in the past, and, in Italy, it is probably one of the most studied together with the Po, Tiber, and Serchio rivers. The alert model we devised can be applied to different watercourses without having to deal with the study of the physics of the process. This makes possible to create a monitoring network for the simulation of the secondary channels as well.

However, this advantage can become a disadvantage if the time series is unreliable on account to the poor management of the station. Variations in the river section or a displacement of the measuring station can cause an inconsistency within the data that prevents these models from functioning correctly. This method allowed to obtain good results by exploiting an LSTM-based architecture. The errors in notification times found in this study are fully comparable with those obtained by other authors who used established physical models (Ercolani and Castelli, 2017). This comparison proved that our models are a valid tool compatible with others already used for flood forecasting. The greatest limit of our model is certainly the lack of information on precipitation falling on the basin until the time of the forecast. If the forecast is issued before

it starts raining in the basin, the model cannot predict the flood event. We think that future studies will improve these models by using precipitation forecast information extracted through artificial intelligence or physics-based techniques (physic-mathematical models, satellite image analysis). The inclusion of these techniques in the development of deep learning models can improve the prediction of a flood event.

Global warming can influence the evolution of the territory and the coastal areas are particularly sensitive to it. In the Pisa coastal plain, coastal erosion at the end of the nineteenth century increased according to this study, in particular after the 1950s, at the end of the 1970s and around 2012. After 2012 there is a slight decrease in the erosion rate, which reaches the same values observed at the beginning of the nineteenth century. On the basis of the erosion rate and the remote sensing analyses on sediment dispersion, we can state that the particular shape of the jetty and of other engineering defenses at the mouth of the Arno River favors the dispersion offshore of the sediments carried by the watercourse and determines the formation of shaded areas in longshore sediment distribution. Despite the construction of several engineering defenses, particularly active erosional trends still appear in two coastal areas (in front of the small town of Marina di Pisa in the southern sector and between the locations of Lame della Gelosia and il Gombo in the northern sector). Erosion is particularly evident in the first location, while it has been countered by numerous, repeated, impacting and expensive engineering interventions for coastal protection in the second one. The fluvial discharge data of the Arno River highlight a discharge decrease that roughly matches the periods that correspond to an increase in erosion. On the other hand, the increase in the flow rate recorded in the last decade can be considered a key element for a reduction in the overall erosion rate recorded in this last period. This correlation is particularly true if we take into account flood events with a value of discharge greater than 700 m^3/s, which are those able to transport suspended sand. The amount of sediment transported by the watercourse has increased in recent years and could certainly counter erosion more effectively if it was possible to reduce the amount of sediment dispersed offshore. Furthermore, it would be important that the sediments were distributed more uniformly longshore, so as to avoid the formation of shadow areas in the distribution of the sedimentary load transported by the watercourse. Although modest, the changes of the erosive trend that have been observed in the last eight years represent an important signal for the development of this territory. It will be necessary to monitor this coastal stretch with DGPS at high temporal resolution in order to understand whether this documented decrease will continue over time.

Future sporadic measurements of the solid load conducted near the river mouth during flood events could allow to calibrate the satellite observations (plume amplitude versus measured solid load data) to derive the solid load data directly from the study of satellite images, with considerable saving of time and money. A similar integrated approach could be easily used in other contexts affected by coastal erosion, where a holistic approach of this type could help identify unclear causes of erosion and support future development of these sensitive areas. Given this need, this work wanted to propose a new method of shoreline identification based on the use of drones. The method is a valid alternative to the classical methods of shoreline identification based on topography. This method makes it possible to obtain shorelines using the topography obtained from UAV images; it is a novelty compared to other uses of DEMs obtained from UAV images present in literature. This approach is innovative and could also be a valid alternative to the methods based on manual identification or on remote-sensing image colors. In this respect, it is very difficult to compare differently-derived shorelines when the errors are about 1–2 m. When we compare the use of satellite images and DGPS, identification of the error between the two methods is simpler than when we compare the DGPS-derived shoreline with UAV-derived images. This happens because the error of DGPS points to extract the shoreline is negligible compared to the errors that occur when using satellite images with a pixel size of about 10 meters. However, when we compare DGPS-derived shorelines with UAV-derived images, all the errors are of the same order of magnitude. This work has shown that in some cases the DGPS-derived shoreline is better than the UAV-derived shoreline, but in the same number of cases, the roles are reversed. Therefore, it is very difficult to determine the best method by a simple comparison of the errors. However, this new method has two main advantages regarding the use of DGPS points. The first one is the time needed to obtain a stretch of coast: a UAV takes less than a DGPS. To sample 4.5 km of coastline with UAV, we took about 3 hours while with the DPGS, we took about 6 hours. The second advantage is that the position of the transects used to reconstruct the shoreline can be decided after sampling and not during acquisition of the DGPS points.

In conclusion, this PhD work demonstrates that a multidisciplinary approach is essential to face the future challenges that global warming will reserve for us both in terms of scientific research and correct and effective territorial management. This PhD work did not want to highlight any repercussions of global warming on the territory but wanted, above all, to tackle the next step of the research, trying to provide valid

tools useful for territorial management. Public administrations and research institutions will be able to use, and even improve, the tools developed in this thesis and this may have a close social and scientific impact.

For example, the shoreline sampling tool can be used by public administrations which, having a guided and standardized procedure, will be able to carry out more objective and scientifically based measurements.

On the other hand, the tool based on artificial intelligence models for forecasting flood events could be the object of an application for the territorial entities of the study area of this thesis but also a basis on which to develop future algorithms for other territorial realities.

The future use of the tools will be able to highlight potential and critical issues leading to the future development of them and new scientific investigations.

References

Abadi, M., Agarwal, A., Barham, P., Brevdo, E., Chen, Z., Citro, C., Corrado, G.S., Davis, A., Dean, J., Devin, M., Ghemawat, S., Goodfellow, I., Harp, A., Irving, G., Isard, M., Jia, Y., Jozefowicz, R., Kaiser, L., Kudlur, M., Levenberg, J., Mané, D., Monga, R., Moore, S., Murray, D., Olah, C., Schuster, M., Shlens, J., Steiner, B., Sutskever, I., Talwar, K., Tucker, P., Vanhoucke, V., Vasudevan, V., Viégas, F., Vinyals, O., Warden, P., Wattenberg, M., Wicke, M., Yu, Y., Zheng, X., 2015. TensorFlow: Large-Scale Machine Learning on Heterogeneous Systems.

Ali, H., Fowler, H.J., Mishra, V., 2018. Global observational evidence of strong linkage between dew point temperature and precipitation extremes. Geophys Res Lett 45, 12–320.

Allan, R.P., 2011. Human influence on rainfall. Nature 470, 344–345. https://doi.org/10.1038/470344a

Allan, R.P., Soden, B.J., John, V.O., Ingram, W., Good, P., 2010. Current changes in tropical precipitation. Environmental Research Letters 5, 025205.

Allen, M.R., Ingram, W.J., 2002. Constraints on future changes in climate and the hydrologic cycle. Nature 419, 228–232.

Aminti, P., Cammelli, C., Cappietti, L., Jackson, N.L., Nordstrom, K.F., Pranzini, E., 2004. Evaluation of Beach Response to Submerged Groin Construction at Marina di Ronchi, Italy, Using Field Data and a Numerical Simulation Model. J Coast Res 99–120.

Anfuso, G., Pranzini, E., Vitale, G., 2011. An integrated approach to coastal erosion problems in northern Tuscany (Italy): Littoral morphological evolution and cell distribution. Geomorphology 129, 204–214. https://doi.org/https://doi.org/10.1016/j.geomorph.2011.01.023

Anthony, E.J., 2018. Sand and gravel supply from rivers to coasts: A review from a Mediterranean perspective. Atti della Societa Toscana di Scienze Naturali, Memorie Serie A 125, 13–33.

Anthony, E.J., Marriner, N., Morhange, C., 2014. Human influence and the changing geomorphology of Mediterranean deltas and coasts over the last 6000years: From progradation to destruction phase? Earth Sci Rev 139, 336–361. https://doi.org/https://doi.org/10.1016/j.earscirev.2014.10.003

Antonetti, M., Zappa, M., 2018. How can expert knowledge increase the realism of conceptual hydrological models? A case study based on the concept of dominant runoff process in the Swiss Pre-Alps. Hydrol Earth Syst Sci 22, 4425–4447. https://doi.org/10.5194/hess-22-4425-2018

Autorità di bacino del Fiume Arno, 2000. Attività estrattive, in: Supplemento Alla Gazzetta Ufficiale, Serie Generale n. 122.

Autorità di Bacino del Fiume Arno, 1989. PIANO DI BACINO DEL FIUME ARNO.

Bates, B., Kundzewicz, Z.W., Wu, S., Burkett, V., Doell, P., Gwary, D., Hanson, C., Heij, B., Jiménez, B., Kaser, G., Kitoh, A., Kovats, S., Kumar, P., Magadza, C.H.D., Martino, D., Mata, L., Medany, M., Miller, K., Arnell, N., 2008. Climate Change and Water. Technical Paper of the Intergovernmental Panel on Climate Change.

Bates, B.C. (Bryson C.), Kundzewicz, Z., Wu, S., Palutikof, J., Intergovernmental Panel on Climate Change. Working Group II, n.d. Climate change and water.

Becchi I., 1986. Introduction to the Arno basin flooding problems, in: CNR-GNDCI pubbl. (Ed.), International Conference on the Arno Project.

Bellotti, P., Calderoni, G., di Rita, F., D'Orefice, M., D'Amico, C., Esu, D., Magri, D., Martinez, M.P., Tortora, P., Valeri, P., 2011. The Tiber river delta plain (central Italy): Coastal evolution and implications for the ancient Ostia Roman settlement. Holocene 21, 1105–1116. https://doi.org/10.1177/0959683611400464

Berg, P., Haerter, J.O., Thejll, P., Piani, C., Hagemann, S., Christensen, J.H., 2009. Seasonal characteristics of the relationship between daily precipitation intensity and surface temperature. Journal of Geophysical Research: Atmospheres 114.

Berg, P., Moseley, C., Haerter, J.O., 2013. Strong increase in convective precipitation in response to higher temperatures. Nat Geosci 6, 181–185.

Bertola, M., Viglione, A., Hall, J., Blöschl, G., 2019. Flood trends in Europe: are changes in small and big floods different? Hydrology and Earth System Sciences Discussions 1–23. https://doi.org/10.5194/hess-2019-523

Bertoni, D., Bini, M., Luppichini, M., Cipriani, L.E.L.E., Carli, A., Sarti, G., 2021. Anthropogenic impact on beach heterogeneity within a littoral cell (Northern Tuscany, Italy). J Mar Sci Eng 9, 1–22. https://doi.org/10.3390/jmse9020151

Bertoni, D., Mencaroni, M., 2015. Four different coastal settings within the northern Tuscany littoral cell: how did we get here? Atti Soc. Sci. nat., Mem., Serie A. 125, 55–68.

Bertoni, D., Sarti, G., Alquini, F., Ciccarelli, D., 2019. Implementing a coastal dune vulnerability index (CDVI) to support coastal management in different settings (Brazil and Italy). Ocean Coast Manag 180. https://doi.org/10.1016/j.ocecoaman.2019.104916

Besset, M., Anthony, E.J., Bouchette, F., 2019. Multi-decadal variations in delta shorelines and their relationship to river sediment supply: An assessment and review. Earth Sci Rev 193, 199–219. https://doi.org/10.1016/j.earscirev.2019.04.018

Besset, M., Anthony, E.J., Sabatier, F., 2017. River delta shoreline reworking and erosion in the Mediterranean and Black Seas: The potential roles of fluvial sediment starvation and other factors. Elementa Science of the Anthropocene 5. https://doi.org/10.1525/elementa.139

Billi, P., Fazzini, M., 2017. Global change and river flow in Italy. Glob Planet Change 155, 234–246. https://doi.org/https://doi.org/10.1016/j.gloplacha.2017.07.008

Billi, P., Rinaldi, M., 1997. Human impact on sediment yield and channel dynamics in the Arno River Basin (central Italy). Human impact on erosion and sedimentation. Proc. international symposium, Rabat, Morocco, 1997 245, 301–311.

Bini, M., Casarosa, N., Luppichini, M., 2021. Exploring the relationship between river discharge and coastal erosion: An integrated approach applied to the pisa coastal plain (italy). Remote Sens (Basel) 13. https://doi.org/10.3390/rs13020226

Bini, M., Casarosa, N., Ribolini, A., 2008. L'evoluzione diacronica della linea di riva del litorale Pisano (1938-2004) sulla base del confront di immagini aeree georeferenziate. Atti della Societa Toscana di Scienze Naturali, Memorie Serie A 113, 1–12.

Bini, M., Rossi, V., 2021. Climate Change and Anthropogenic Impact on Coastal Environments. Water (Basel) 13. https://doi.org/10.3390/w13091182

Bini, M., Rossi, V., Amorosi, A., Pappalardo, M., Sarti, G., Noti, V., Capitani, M., Fabiani, F., Gualandi, M.L., 2015. Palaeoenvironments and palaeotopography of a multilayered city during the Etruscan and Roman periods: early interaction of fluvial processes and urban growth at Pisa (Tuscany, Italy). J Archaeol Sci 59, 197–210. https://doi.org/https://doi.org/10.1016/j.jas.2015.04.005

Bird, E.C.F. (Eric C.F., on the Dynamics of Coastline Erosion, I.G.Union.W.G., on the Coastal Environment, I.G.Union.C., 1985. Coastline changes : a global review. Chichester (West Sussex] ; New York : Wiley.

Blenkinsop, S., Chan, S.C., Kendon, E.J., Roberts, N.M., Fowler, H.J., 2015. Temperature influences on intense UK hourly precipitation and dependency on large-scale circulation. Environmental Research Letters 10, 054021.

Blöschl, G., Hall, J., Viglione, A., Perdigão, R.A.P., Parajka, J., Merz, B., Lun, D., Arheimer, B., Aronica, G.T., Bilibashi, A., Boháč, M., Bonacci, O., Borga, M., Čanjevac, I., Castellarin, A., Chirico, G.B., Claps, P., Frolova, N., Ganora, D., Gorbachova, L., Gül, A., Hannaford, J., Harrigan, S., Kireeva, M., Kiss, A., Kjeldsen, T.R., Kohnová, S., Koskela, J.J., Ledvinka, O., Macdonald, N., Mavrova-Guirguinova, M., Mediero, L., Merz, R., Molnar, P., Montanari, A., Murphy, C., Osuch, M., Ovcharuk, V., Radevski, I., Salinas, J.L., Sauquet, E., Šraj, M., Szolgay, J., Volpi, E., Wilson, D., Zaimi, K., Živković, N., 2019. Changing climate both increases and decreases European river floods. Nature 573, 108–111. https://doi.org/10.1038/s41586-019-1495-6

Blott, S., Pye, K., 2001. GRADISTAT: A grain size distribution and statistics package for the analysis of unconsolidated sediments. Earth Surf Process Landf 26, 1237–1248. https://doi.org/10.1002/esp.261

Boak, E.H., Turner, I.L., 2005. Shoreline Definition and Detection: A Review. J Coast Res 21, 688–703. https://doi.org/10.2112/03-0071.1

Börgel, F., Frauen, C., Neumann, T., Meier, H.E.M., 2020. The Atlantic Multidecadal Oscillation controls the impact of the North Atlantic Oscillation on North European climate. Environmental Research Letters 15. https://doi.org/10.1088/1748-9326/aba925

Borgh, L., 1970. Apporto allo studio sulle cause di variazione del litorale pisano, Rassegna Periodico culturale e di informazioni. Comune di Pisa.

Boulmaiz, T., Guermoui, M., Boutaghane, H., 2020. Impact of training data size on the LSTM performances for rainfall–runoff modeling. Model Earth Syst Environ 6, 2153–2164. https://doi.org/10.1007/s40808-020-00830-w

Bouvier, C., Balouin, Y., Castelle, B., 2017. Video monitoring of sandbar-shoreline response to an offshore submerged structure at a microtidal beach. Geomorphology 295, 297–305. https://doi.org/10.1016/j.geomorph.2017.07.017

Brandimarte, L., di Baldassarre, G., Bruni, G., D'Odorico, P., Montanari, A., D'Odorico, P., Montanari, A., 2011. Relation Between the North-Atlantic Oscillation and Hydroclimatic Conditions in Mediterranean Areas. Water Resources Management 25, 1269–1279. https://doi.org/10.1007/s11269-010-9742-5

Bryndal, T., Franczak, P., Kroczak, R., Cabaj, W., Kołodziej, A., 2017. The impact of extreme rainfall and flash floods on the flood risk management process and geomorphological changes in small Carpathian catchments: a case study of the Kasiniczanka river (Outer Carpathians, Poland). Natural Hazards 88, 95–120. https://doi.org/10.1007/s11069-017-2858-7

Busuioc, A., Birsan, M., Carbunaru, D., Baciu, M., Orzan, A., 2016. Changes in the large-scale thermodynamic instability and connection with rain shower frequency over Romania: verification of the Clausius–Clapeyron scaling. International Journal of Climatology 36, 2015–2034.

Caloiero, T., Caloiero, P., Frustaci, F., 2018. Long-term precipitation trend analysis in Europe and in the Mediterranean basin. Water and Environment Journal 32, 433–445. https://doi.org/https://doi.org/10.1111/wej.12346

Caloiero, T., Coscarelli, R., Ferrari, E., Mancini, M., 2011. Precipitation change in Southern Italy linked to global scale oscillation indexes. Nat. Hazards Earth Syst. Sci. 11, 1683–1694. https://doi.org/10.5194/nhess-11-1683-2011

Caporali, E., Lompi, M., Pacetti, T., Chiarello, V., Fatichi, S., 2021. A review of studies on observed precipitation trends in Italy. International Journal of Climatology. https://doi.org/10.1002/joc.6741

Caporali, E., Rinaldi, M., Casagli, N., 2005. The Arno River Floods. Giornale di Geologia Applicata 1, 177–192. https://doi.org/10.1474/GGA.2005-01.0-18.0018

Cappucci, S., Bertoni, D., Cipriani, L.E., Boninsegni, G., Sarti, G., 2020. Assessment of the Anthropogenic Sediment Budget of a Littoral Cell System (Northern Tuscany, Italy). Water (Basel) 12, 3240. https://doi.org/10.3390/w12113240

Cardoso Pereira, S., Marta-Almeida, M., Carvalho, A.C., Rocha, A., 2020. Extreme precipitation events under climate change in the Iberian Peninsula. International Journal of Climatology 40, 1255–1278. https://doi.org/https://doi.org/10.1002/joc.6269

Casarosa, N., 2016. Studio dell ' evoluzione del litorale pisano tramite rilievi con GPS differenziale (2008-2014). Studi costieri 3–19.

Cavazza, S., 1984. Regionalizzazione geomorfologica del trasporto solido in sospensione dei corsi d'acqua tra il magra e l'ombrone (* *). Atti della Societa Toscana di Scienze Naturali, Memorie Serie A 91, 119–132.

Chattopadhyay, A., Nabizadeh, E., Hassanzadeh, P., 2020. Analog Forecasting of Extreme-Causing Weather Patterns Using Deep Learning. J Adv Model Earth Syst 12, e2019MS001958. https://doi.org/10.1029/2019MS001958

Chernokulsky, A., Kozlov, F., Zolina, O., Bulygina, O., Mokhov, I.I., Semenov, V.A., 2019. Observed changes in convective and stratiform precipitation in Northern Eurasia over the last five decades. Environmental Research Letters 14, 045001.

Chollet, F., 2015. Keras.

Cipriani, L.E., Ferri, S., Iannotta, P., Paolieri, F., Pranzini, E., 2001. Morfologia e dinamica dei sedimenti del litorale della Toscana settentrionale. Studi costieri 119–156.

Climate Prediction Center, 2021. East Atlantic [WWW Document]. URL https://www.cpc.ncep.noaa.gov/data/teledoc/ea.shtml (accessed 9.22.21).

Climatic Research Unit, 2021. Mediterranean Oscillation Indices (MOI) [WWW Document]. URL https://crudata.uea.ac.uk/cru/data/moi/ (accessed 9.22.21).

Colantoni, A., Delfanti, L., Cossio, F., Baciotti, B., Salvati, L., Perini, L., Lord, R., 2015. Soil Aridity under Climate Change and Implications for Agriculture in Italy. Applied Mathematical Sciences 9, 2467–2475. https://doi.org/10.12988/ams.2015.52112

D'Amato Avanzi, G., Giannecchini, R., Puccinelli, A., 2004. The influence of the geological and geomorphological settings on shallow landslides. An example in a temperate climate environment: the June 19, 1996 event in northwestern Tuscany (Italy). Eng Geol 73, 215–228. https://doi.org/https://doi.org/10.1016/j.enggeo.2004.01.005

Degeai, J.-P., Bertoncello, F., Vacchi, M., Augustin, L., de Moya, A., Ardito, L., Devillers, B., 2020. A new interpolation method to measure delta evolution and sediment flux: Application to the late Holocene coastal plain of the Argens River in the western Mediterranean. Mar Geol 424, 106159. https://doi.org/https://doi.org/10.1016/j.margeo.2020.106159

Deitch, M.J., Sapundjieff, M.J., Feirer, S.T., 2017. Characterizing Precipitation Variability and Trends in the World's Mediterranean-Climate Areas. Water (Basel) 9. https://doi.org/10.3390/w9040259

Deser, C., Hurrell, J.W., Phillips, A.S., 2017. The role of the North Atlantic Oscillation in European climate projections. Clim Dyn 49, 3141–3157. https://doi.org/10.1007/s00382-016-3502-z

Dewi, R.S., Bijker, W., 2020. Dynamics of shoreline changes in the coastal region of Sayung, Indonesia. Egyptian Journal of Remote Sensing and Space Science 23, 181–193. https://doi.org/10.1016/j.ejrs.2019.09.001

Di Luccio, D., Benassai, G., Di Paola, G., Rosskopf, C.M., Mucerino, L., Montella, R., Contestabile, P., 2018. Monitoring and modelling coastal vulnerability and mitigation proposal for an archaeological site (Kaulonia, Southern Italy). Sustainability (Switzerland) 10, 1–18. https://doi.org/10.3390/su10062017

Diodato, N., 2007. Climatic fluctuations in southern Italy since the 17th century: Reconstruction with precipitation records at Benevento. Clim Change 80, 411–431. https://doi.org/10.1007/s10584-006-9119-1

Diodato, N., Ljungqvist, F.C., Bellocchi, G., 2021. Outcome of environmental change from historical sediment discharge in a Mediterranean fluvial basin, 1500–2019 CE. Environ Res Commun 3, 071002. https://doi.org/10.1088/2515-7620/ac0b83

Dogliotti, A.I., Ruddick, K.G., Nechad, B., Doxaran, D., Knaeps, E., 2015. A single algorithm to retrieve turbidity from remotely-sensed data in all coastal and estuarine waters. Remote Sens Environ 156, 157–168. https://doi.org/10.1016/j.rse.2014.09.020

Dolan, R., Hayden, P.B., May, P., May, S.K., 1980. The reliability of shoreline change measurements from aerial photographs. Shore Beach 48, 22–29.

Dünkeloh, A., Jacobeit, J., 2003. Circulation dynamics of Mediterranean precipitation variability 1948–98. International Journal of Climatology 23, 1843–1866. https://doi.org/https://doi.org/10.1002/joc.973

Ercolani, G., Castelli, F., 2017. Variational assimilation of streamflow data in distributed flood forecasting. Water Resour Res 53, 158–183. https://doi.org/10.1002/2016WR019208

Ericson, J., Vörösmarty, C., Dingman, S., Ward, L., Meybeck, M., 2006. Effective Sea-level Rise and Deltas: Causes of Change and Human Dimension Implications. Glob Planet Change 50, 63–82. https://doi.org/10.1016/j.gloplacha.2005.07.004

European Environment Agency, 2019. Economic losses from climate -related extremes in Europe [WWW Document]. Indicator Assessment. URL https://www.eea.europa.eu/data-and-maps/indicators/direct-losses-from-weather-disasters-3/assessment-2 (accessed 1.31.20).

Faust, J.C., Fabian, K., Milzer, G., Giraudeau, J., Knies, J., 2016. Norwegian fjord sediments reveal NAO related winter temperature and precipitation changes of the past 2800 years. Earth Planet Sci Lett 435, 84–93. https://doi.org/https://doi.org/10.1016/j.epsl.2015.12.003

Favalli, M., Fornaciai, A., Isola, I., Tarquini, S., Nannipieri, L., 2012. Multiview 3D reconstruction in geosciences. Comput Geosci 44, 168–176. https://doi.org/https://doi.org/10.1016/j.cageo.2011.09.012

Fawaz, H.I., Forestier, G., Weber, J., Fawaz, H.I., Forestier, G., Weber, J., Idoumghar, L., Muller, P., 2020. Deep learning for time series classification : a review To cite this version : HAL Id : hal-02365025 Deep learning for time series classification : a review.

Federici, Mazzanti, 1993. Note sulle pianure costiere della Toscana. Roma.

Ferrari, E., Caloiero, T., Coscarelli, R., 2013. Influence of the North Atlantic Oscillation on winter rainfall in Calabria (southern Italy). Theor Appl Climatol 114, 479–494. https://doi.org/10.1007/s00704-013-0856-6

Formayer, H., Fritz, A., 2017. Temperature dependency of hourly precipitation intensities–surface versus cloud layer temperature. International Journal of Climatology 37, 1–10.

Frankignoul, C., Friederichs, P., Kestenare, E., 2003. Influence of Atlantic SST anomalies on the atmospheric circulation in the Atlantic-European sector, ANNALS OF GEOPHYSICS.

García-Rubio, G., Huntley, D., Russell, P., 2015. Evaluating shoreline identification using optical satellite images. Mar Geol 359, 96–105. https://doi.org/10.1016/j.margeo.2014.11.002

Gaume, E., Bain, V., Bernardara, P., Newinger, O., Barbuc, M., Bateman, A., Blaškovičová, L., Blöschl, G., Borga, M., Dumitrescu, A., Daliakopoulos, I., Garcia, J., Irimescu, A., Kohnova, S., Koutroulis, A., Marchi, L., Matreata, S., Medina, V., Preciso, E., Sempere-Torres, D., Stancalie, G., Szolgay, J., Tsanis,

I., Velasco, D., Viglione, A., 2009. A compilation of data on European flash floods. J Hydrol (Amst) 367, 70–78. https://doi.org/https://doi.org/10.1016/j.jhydrol.2008.12.028

Gaume, E., Borga, M., LLASSAT, M.C., Maouche, S., Lang, M., DIAKAKIS, M., 2016. Mediterranean extreme floods and flash floods , in: The Mediterranean Region under Climate Change. A Scientific Update, Coll. Synthèses. IRD Editions, pp. 133–144.

George, D.G., Järvinen, M., Arvola, L., 2004. The influence of the North Atlantic Oscillation on the winter characteristics of Windermere (UK) and Pääjärvi (Finland).

Giannecchini, R., 2006. Relationship between rainfall and shallow landslides in the southern Apuan Alps (Italy). Natural Hazards and Earth System Science 6, 357–364. https://doi.org/10.5194/nhess-6-357-2006

Giannecchini, R., D'Amato Avanzi, G., 2012. Historical research as a tool in estimating hydrogeological hazard in a typical small alpine-like area: The example of the Versilia River basin (Apuan Alps, Italy). Physics and Chemistry of the Earth, Parts A/B/C 49, 32–43. https://doi.org/10.1016/J.PCE.2011.12.005

Giorgi, F., 2006. Climate change hot-spots. Geophys Res Lett 33. https://doi.org/https://doi.org/10.1029/2006GL025734

Goodfellow, I., Bengio, Y., Courville, A., 2016. Deep Learning. MIT Press.

Grottoli, E., Bertoni, D., Pozzebon, A., Ciavola, P., 2019. Influence of particle shape on pebble transport in a mixed sand and gravel beach during low energy conditions. Ocean Coast Manag. https://doi.org/10.1016/j.ocecoaman.2018.12.014

Haerter, J.O., Berg, P., Hagemann, S., 2010. Heavy rain intensity distributions on varying time scales and at different temperatures. Journal of Geophysical Research: Atmospheres 115.

Halifa-Marín, A., Lorente-Plazas, R., Pravia-Sarabia, E., Montávez, J.P., Jiménez-Guerrero, P., 2021. Atlantic and Mediterranean influence promoting an abrupt change in winter precipitation over the southern Iberian Peninsula. Atmos Res 253. https://doi.org/10.1016/j.atmosres.2021.105485

Hardwick Jones, R., Westra, S., Sharma, A., 2010. Observed relationships between extreme sub-daily precipitation, surface temperature, and relative humidity. Geophys Res Lett 37. https://doi.org/https://doi.org/10.1029/2010GL045081

Hu, Y., Yan, L., Hang, T., Feng, J., 2020. Stream-Flow Forecasting of Small Rivers Based on LSTM.

Hurrell, J.W., 1995. Decadal Trends in the North Atlantic Oscillation: Regional Temperatures and Precipitation. Science (1979) 269, 676 LP – 679. https://doi.org/10.1126/science.269.5224.676

IPCC, 2018. Global warming of 1.5°C. An IPCC Special Report on the impacts of global warming of 1.5°C above pre-industrial levels and related global greenhouse gas emission pathways, in the context of strengthening the global response to the threat of climate change,.

IPCC, 2014. Climate Change 2014: Synthesis Report. Contribution of Working Groups I, II and III to the Fifth Assessment Report of the Intergovernmental Panel on Climate Change.

IPCC, 2013. Climate change 2013 The Physical Science Basis (eds Stocker, T. F. et al.).

Izquierdo, R., Alarcón, M., Aguillaume, L., Àvila, A., 2014. Effects of teleconnection patterns on the atmospheric routes, precipitation and deposition amounts in the north-eastern Iberian Peninsula. Atmos Environ 89, 482–490. https://doi.org/https://doi.org/10.1016/j.atmosenv.2014.02.057

Jaiswal, R.K., Ali, S., Bharti, B., 2020. Comparative evaluation of conceptual and physical rainfall–runoff models. Appl Water Sci 10, 48. https://doi.org/10.1007/s13201-019-1122-6

James, H., Makiko, S., Reto, R., Ken, L., W, L.D., Martin, M.-E., 2006. Global temperature change. Proceedings of the National Academy of Sciences 103, 14288–14293. https://doi.org/10.1073/pnas.0606291103

Jonkman, S.N., 2005. Global Perspectives on Loss of Human Life Caused by Floods. Natural Hazards 34, 151–175. https://doi.org/10.1007/s11069-004-8891-3

Kabir, M.A., Salauddin, M., Hossain, K.T., Tanim, I.A., Saddam, M.M.H., Ahmad, A.U., 2020. Assessing the shoreline dynamics of Hatiya Island of Meghna estuary in Bangladesh using multiband satellite imageries and hydro-meteorological data. Reg Stud Mar Sci 35, 101167. https://doi.org/10.1016/j.rsma.2020.101167

Kalimeris, A., Ranieri, E., Founda, D., Norrant, C., 2017. Variability modes of precipitation along a Central Mediterranean area and their relations with ENSO, NAO, and other climatic patterns. Atmos Res 198, 56–80. https://doi.org/https://doi.org/10.1016/j.atmosres.2017.07.031

Kelly, J.T., Gontz, A.M., 2018. Using GPS-surveyed intertidal zones to determine the validity of shorelines automatically mapped by Landsat water indices. International Journal of Applied Earth Observation and Geoinformation 65, 92–104. https://doi.org/10.1016/j.jag.2017.10.007

Kingma, D.P., Ba, J., 2014. Adam: A Method for Stochastic Optimization.

Knight, J.R., Allan, R.J., Folland, C.K., Vellinga, M., Mann, M.E., 2005. A signature of persistent natural thermohaline circulation cycles in observed climate. Geophys Res Lett 32. https://doi.org/10.1029/2005GL024233

Kohv, M., Sepp, E., Vammus, L., 2017. Assessing multitemporal water-level changes with uav-based photogrammetry. The Photogrammetric Record 32, 424–442. https://doi.org/10.1111/phor.12214

Kotsias, G., Lolis, C.J., Hatzianastassiou, N., Levizzani, V., Bartzokas, A., 2020. On the connection between large-scale atmospheric circulation and winter GPCP precipitation over the Mediterranean region for the period 1980-2017. Atmos Res 233, 104714. https://doi.org/https://doi.org/10.1016/j.atmosres.2019.104714

Koyama, T., Stroeve, J., 2019. Greenland monthly precipitation analysis from the Arctic System Reanalysis (ASR): 2000–2012. Polar Sci 19, 1–12. https://doi.org/https://doi.org/10.1016/j.polar.2018.09.001

Kratzert, F., Klotz, D., Brenner, C., Schulz, K., Herrnegger, M., 2018. Rainfall – runoff modelling using Long Short-Term Memory (LSTM) networks 6005–6022.

Le, X.H., Ho, H., Lee, G., Jung, S., 2019. Application of Long Short-Term Memory (LSTM) Neural Network for Flood Forecasting. Water (Basel) 11, 1387. https://doi.org/10.3390/w11071387

LeCun, Y., Bengio, Y., Hinton, G., 2015. Deep learning. Nature 521, 436–444. https://doi.org/10.1038/nature14539

Lenderink, G., Barbero, R., Loriaux, J.M., Fowler, H.J., 2017. Super-Clausius–Clapeyron Scaling of Extreme Hourly Convective Precipitation and Its Relation to Large-Scale Atmospheric Conditions. J Clim 30, 6037–6052. https://doi.org/10.1175/JCLI-D-16-0808.1

Lenderink, G., Barbero, R., Westra, S., Fowler, H.J., 2018. Reply to comments on “Temperature-extreme precipitation scaling: A two-way causality?” International Journal of Climatology 38, 4664–4666.

Lenderink, G., Mok, H.Y., Lee, T.C., van Oldenborgh, G.J., 2011. Scaling and trends of hourly precipitation extremes in two different climate zones–Hong Kong and the Netherlands. Hydrol Earth Syst Sci 15, 3033–3041.

Lenderink, G., van Meijgaard, E., 2010. Linking increases in hourly precipitation extremes to atmospheric temperature and moisture changes. Environmental Research Letters 5, 025208.

Lenderink, G., van Meijgaard, E., 2008. Increase in hourly precipitation extremes beyond expectations from temperature changes. Nat Geosci 1, 511–514.

Lenôtre, N., Thierry, P., Batkowski, D., Vermeersch, F., 2004. EUROSION project The Coastal Erosion Layer WP 2.6 45.

Lepore, C., Veneziano, D., Molini, A., 2015. Temperature and CAPE dependence of rainfall extremes in the eastern United States. Geophys Res Lett 42, 74–83.

Li, W., Gong, P., 2016. Continuous monitoring of coastline dynamics in western Florida with a 30-year time series of Landsat imagery. Remote Sens Environ 179, 196–209. https://doi.org/10.1016/j.rse.2016.03.031

Li, W., Kiaghadi, A., Dawson, C., 2020. High temporal resolution rainfall–runoff modeling using long-short-term-memory (LSTM) networks. Neural Comput Appl. https://doi.org/10.1007/s00521-020-05010-6

Liu, D., Jiang, W., Mu, L., Wang, S., 2020. Streamflow Prediction Using Deep Learning Neural Network: Case Study of Yangtze River. IEEE Access 8, 90069–90086. https://doi.org/10.1109/ACCESS.2020.2993874

Livieris, I.E., Pintelas, E., Pintelas, P., 2020. A CNN–LSTM model for gold price time-series forecasting. Neural Comput Appl 32, 17351–17360. https://doi.org/10.1007/s00521-020-04867-x

Longobardi, A., Villani, P., 2010. Trend analysis of annual and seasonal rainfall time series in the Mediterranean area. International Journal of Climatology 30, 1538–1546. https://doi.org/https://doi.org/10.1002/joc.2001

Lopez-Bustins, J.A., Arbiol-Roca, L., Martin-Vide, J., Barrera-Escoda, A., Prohom, M., 2020. Intra-annual variability of the Western Mediterranean Oscillation (WeMO) and occurrence of extreme torrential precipitation in Catalonia (NE Iberia). Natural Hazards and Earth System Sciences 20, 2483–2501. https://doi.org/10.5194/nhess-20-2483-2020

Lopez-Bustins, J.-A., Martin-Vide, J., Sanchez-Lorenzo, A., 2008. Iberia winter rainfall trends based upon changes in teleconnection and circulation patterns. Glob Planet Change 63, 171–176. https://doi.org/https://doi.org/10.1016/j.gloplacha.2007.09.002

López-Moreno, J.I., Vicente-Serrano, S.M., Morán-Tejeda, E., Lorenzo-Lacruz, J., Kenawy, A., Beniston, M., 2011. Effects of the North Atlantic Oscillation (NAO) on combined temperature and precipitation winter modes in the Mediterranean mountains: Observed relationships and projections for the 21st century. Glob Planet Change 77, 62–76. https://doi.org/https://doi.org/10.1016/j.gloplacha.2011.03.003

Lowe, D.G., 2004. Distinctive Image Features from Scale-Invariant Keypoints. Int J Comput Vis 60, 91–110. https://doi.org/10.1023/B:VISI.0000029664.99615.94

Luijendijk, A., Hagenaars, G., Ranasinghe, R., Baart, F., Donchyts, G., Aarninkhof, S., 2018. The State of the World's Beaches. Sci Rep 8, 6641. https://doi.org/10.1038/s41598-018-24630-6

Luppichini, M., Barsanti, M., Giannecchini, R., Bini, M., 2022a. Deep learning models to predict flood events in fast-flowing watersheds. Science of The Total Environment 813, 151885. https://doi.org/https://doi.org/10.1016/j.scitotenv.2021.151885

Luppichini, M., Barsanti, M., Giannecchini, R., Bini, M., 2021. Statistical relationships between large-scale circulation patterns and local-scale effects: NAO and rainfall regime in a key area of the Mediterranean basin. Atmos Res 248, 105270.

Luppichini, M., Bini, M., Barsanti, M., Giannecchini, R., Zanchetta, G., 2022b. Seasonal rainfall trends of a key Mediterranean area in relation to large-scale atmospheric circulation: How does current global change affect the rainfall regime? J Hydrol (Amst) 612, 128233. https://doi.org/https://doi.org/10.1016/j.jhydrol.2022.128233

Luppichini, M., Bini, M., Paterni, M., Berton, A., Merlino, S., 2020. A new beach topography-based method for shoreline identification. Water (Switzerland) 12, 1–11. https://doi.org/10.3390/w12113110

Luppichini, M., Favalli, M., Isola, I., Nannipieri, L., Giannecchini, R., Bini, M., 2019. Influence of topographic resolution and accuracy on hydraulic channel flow simulations: Case study of the Versilia River (Italy). Remote Sens (Basel) 11. https://doi.org/10.3390/rs11131630

Mackenzie, J.R., Duke, N.C., Wood, A.L., 2016. The Shoreline Video Assessment Method (S-VAM): Using dynamic hyperlapse image acquisition to evaluate shoreline mangrove forest structure, values, degradation and threats. Mar Pollut Bull 109, 751–763. https://doi.org/10.1016/j.marpolbul.2016.05.069

Mahabot, M.M., Jaud, M., Pennober, G., Le Dantec, N., Troadec, R., Suanez, S., Delacourt, C., 2017. The basics for a permanent observatory of shoreline evolution in tropical environments; lessons from back-reef beaches in La Reunion Island. Comptes Rendus - Geoscience 349, 330–340. https://doi.org/10.1016/j.crte.2017.09.010

Marçais, J., de Dreuzy, J.-R., 2017. Prospective Interest of Deep Learning for Hydrological Inference. Groundwater 55, 688–692. https://doi.org/https://doi.org/10.1111/gwat.12557

Martín, P., Sabatés, A., Lloret, J., Martin-Vide, J., 2012. Climate modulation of fish populations: The role of the Western Mediterranean Oscillation (WeMO) in sardine (Sardina pilchardus) and anchovy (Engraulis encrasicolus) production in the north-western Mediterranean. Clim Change 110, 925–939. https://doi.org/10.1007/s10584-011-0091-z

Martinez-Artigas, J., Lemus-Canovas, M., Lopez-Bustins, J.A., 2021. Precipitation in peninsular Spain: Influence of teleconnection indices and spatial regionalisation. International Journal of Climatology 41, E1320–E1335. https://doi.org/https://doi.org/10.1002/joc.6770

Martin-Vide, J., Lopez-Bustins, J.-A., 2006. The Western Mediterranean Oscillation and rainfall in the Iberian Peninsula. International Journal of Climatology 26, 1455–1475. https://doi.org/https://doi.org/10.1002/joc.1388

Mazzanti, R., 1994. La pianura pisana e i rilievi contermini.

Meehl, G., Goddard, L., Murphy, J., Boer, G., Danabasoglu, G., Dixon, K., Giorgetta, M., Greene, A., Hawkins, E., Hegerl, G., Karoly, D., Kimoto, M., 2009. Decadal Prediction: Can It Be Skillful? Bull Am Meteorol Soc 90, 1467–1485. https://doi.org/10.1175/2009BAMS2778.1

Mellado-Cano, J., Barriopedro, D., García-Herrera, R., Trigo, R.M., Hernández, A., 2019. Examining the North Atlantic Oscillation, East Atlantic Pattern, and Jet Variability since 1685. J Clim 32, 6285–6298. https://doi.org/10.1175/JCLI-D-19-0135.1

Mentaschi, L., Vousdoukas, M.I., Pekel, J.-F., Voukouvalas, E., Feyen, L., 2018. Global long-term observations of coastal erosion and accretion. Sci Rep 8, 12876. https://doi.org/10.1038/s41598-018-30904-w

Merabtene, T., Siddique, M., Shanableh, A., 2016. Assessment of Seasonal and Annual Rainfall Trends and Variability in Sharjah City, UAE. Advances in Meteorology 2016, 6206238. https://doi.org/10.1155/2016/6206238

Moussaid, J., Fora, A.A., Zourarah, B., Maanan, Mehdi, Maanan, Mohamed, 2015. Using automatic computation to analyze the rate of shoreline change on the Kenitra coast, Morocco. Ocean Engineering 102, 71–77. https://doi.org/10.1016/j.oceaneng.2015.04.044

Myhre, G., Alterskjær, K., Stjern, C.W., Hodnebrog, Ø., Marelle, L., Samset, B.H., Sillmann, J., Schaller, N., Fischer, E., Schulz, M., Stohl, A., 2019. Frequency of extreme precipitation increases extensively with event rareness under global warming. Sci Rep 9, 16063. https://doi.org/10.1038/s41598-019-52277-4

Nalley, D., Adamowski, J., Biswas, A., Gharabaghi, B., Hu, W., 2019. A multiscale and multivariate analysis of precipitation and streamflow variability in relation to ENSO, NAO and PDO. J Hydrol (Amst) 574, 288–307. https://doi.org/https://doi.org/10.1016/j.jhydrol.2019.04.024

National Center for Atmospheric Research Staff (Eds), 2021. The Climate Data Guide: Hurrell North Atlantic Oscillation (NAO) Index (PC-based). [WWW Document]. https://climatedataguide.ucar.edu/climate-data/hurrell-north-atlantic-oscillation-nao-index-pc-based.

Nguyen, D.H., Bae, D.-H., 2020. Correcting mean areal precipitation forecasts to improve urban flooding predictions by using long short-term memory network. J Hydrol (Amst) 584, 124710. https://doi.org/https://doi.org/10.1016/j.jhydrol.2020.124710

NOAA, 2021. Extended Reconstructed SST [WWW Document]. URL https://www.ncei.noaa.gov/products/extended-reconstructed-sst (accessed 9.28.21).

Nunziata, F., Buono, A., Migliaccio, M., Benassai, G., Luccio, D. Di, 2019. Shoreline erosion of microtidal beaches examined with UAV and remote sensing techniques. 2018 IEEE International Workshop on Metrology for the Sea; Learning to Measure Sea Health Parameters, MetroSea 2018 - Proceedings 162–166. https://doi.org/10.1109/MetroSea.2018.8657843

O'Gorman, P.A., Muller, C.J., 2010. How closely do changes in surface and column water vapor follow Clausius–Clapeyron scaling in climate change simulations? Environmental Research Letters 5, 025207.

Pall, P., Allen, M.R., Stone, D.A., 2007. Testing the Clausius–Clapeyron constraint on changes in extreme precipitation under CO2 warming. Clim Dyn 28, 351–363.

Palla, B., 1983. Variazioni della linea di riva tra i Fiumi Arno e Serchio (Tenuta di S. Rossore - Pisa) dal 1878 al 1981. Atti Soc. Tosc. Sci. Nat., Mem. Serie A XC, 125–149.

Panthou, G., Mailhot, A., Laurence, E., Talbot, G., 2014. Relationship between surface temperature and extreme rainfalls: A multi-time-scale and event-based analysis. J Hydrometeorol 15, 1999–2011.

Papakonstantinou, A., Topouzelis, K., Pavlogeorgatos, G., 2015. Coastline change detection using UAV, Remote Sensing, GIS and 3D reconstruction.

Paris, E., Becchi, D.I., 1989. Il torso dell'Arno e la sua evoluzione storica. Acqua Aria 6.

Paris, E., Solari, L., Bechi, G., 2012. Applicability of the De Marchi Hypothesis for Side Weir Flow in the Case of Movable Beds. Journal of Hydraulic Engineering 138, 653–656. https://doi.org/10.1061/(ASCE)HY.1943-7900.0000566

Parrish, C., White, S., Calder, B., Pe'eri, S., Rzhanov, Y., 2010. New Approaches for Evaluating Lidar-Derived Shoreline. https://doi.org/10.1364/ORSE.2010.OMC5

Pastor, F., Valiente, J.A., Khodayar, S., 2020. A warming Mediterranean: 38 years of increasing sea surface temperature. Remote Sens (Basel) 12. https://doi.org/10.3390/RS12172687

Petropoulos, G.P., Ireland, G., Barrett, B., 2015. Surface soil moisture retrievals from remote sensing: Current status, products & future trends. Physics and Chemistry of the Earth, Parts A/B/C 83–84, 36–56. https://doi.org/https://doi.org/10.1016/j.pce.2015.02.009

Philandras, C., Nastos, P., Kapsomenakis, J., Douvis, K., Tselioudis, G., Zerefos, C., 2011. Long Term Precipitation Trends and Variability within the Mediterranean Region. Natural Hazards and Earth System Sciences 11, 3235–3250. https://doi.org/10.5194/nhess-11-3235-2011

Pitman, S.J., Hart, D.E., Katurji, M.H., 2019. Application of UAV techniques to expand beach research possibilities: A case study of coarse clastic beach cusps. Cont Shelf Res 184, 44–53. https://doi.org/10.1016/j.csr.2019.07.008

Plant, N.G., Holman, R.A., 1997. Intertidal beach profile estimation using video images. Mar Geol 140, 1–24. https://doi.org/https://doi.org/10.1016/S0025-3227(97)00019-4

Pollard, J.A., Brooks, S.M., Spencer, T., 2019. Harmonising topographic & remotely sensed datasets, a reference dataset for shoreline and beach change analysis. Sci Data 6, 42. https://doi.org/10.1038/s41597-019-0044-3

Pozzebon, A., Cappelli, I., Mecocci, A., Bertoni, D., Sarti, G., Alquini, F., 2018. A Wireless Sensor Network for the Real-Time Remote Measurement of Aeolian Sand Transport on Sandy Beaches and Dunes. Sensors 18, 820. https://doi.org/10.3390/s18030820

Pranzini, E., 2001. Updrift river mouth migration on cuspate deltas: two examples from the coast of Tuscany (Italy). Geomorphology 38, 125–132. https://doi.org/https://doi.org/10.1016/S0169-555X(00)00076-3

Pranzini, E., 1989. A model for cuspidate delta erosion. Coastal zone 89, 4345–4357.

Pranzini, E., Anfuso, G., Cinelli, I., Piccardi, M., Vitale, G., 2018. Shore protection structures increase and evolution on the Northern Tuscany Coast (Italy): Influence of tourism industry. Water (Switzerland) 10. https://doi.org/10.3390/w10111647

Pranzini, E., Simonetti, D., 2008. Influenza del fattore scala sulla classificazione delle spiagge in base alla loro tendenza evolutiva. Studi costieri 14, 13–28.

Pratellesi, M., Ciavola, P., Ivaldi, Roberta., Anthony, E.J., Armaroli, C., 2018. River-mouth geomorphological changes over >130 years (1882–2014) in a small Mediterranean delta: Is the Magra delta reverting to an estuary? Mar Geol 403, 215–224. https://doi.org/https://doi.org/10.1016/j.margeo.2018.06.003

Pulido-Velazquez, M., Peña-Haro, S., García-Prats, A., Mocholi-Almudever, A.F., Henriquez-Dole, L., Macian-Sorribes, H., Lopez-Nicolas, A., 2015. Integrated assessment of the impact of climate and land use changes on groundwater quantity and quality in the Mancha Oriental system (Spain). Hydrol Earth Syst Sci 19, 1677–1693. https://doi.org/10.5194/hess-19-1677-2015

Pumo, D., Carlino, G., Arnone, E., Noto, L. v, 2018. Relationship between extreme rainfall and surface temperature in Sicily (Italy). EPiC Series in Engineering 3, 1718–1726.

Pumo, D., Carlino, G., Blenkinsop, S., Arnone, E., Fowler, H., Noto, L. v, 2019. Sensitivity of extreme rainfall to temperature in semi-arid Mediterranean regions. Atmos Res 225, 30–44. https://doi.org/https://doi.org/10.1016/j.atmosres.2019.03.036

Rapetti, F., Vittorini, S., 1994. Le precipitazioni in Toscana: osservazioni sui casi estremi. Riv Geogr Ital 101, 47–76.

Regione Toscana, 2009. I rimboschimenti in Toscana e la loro gestione. ARSIA.

Riaz, S.M.F., Iqbal, M.J., Hameed, S., 2017. Impact of the North Atlantic Oscillation on winter climate of Germany. Tellus, Series A: Dynamic Meteorology and Oceanography 69. https://doi.org/10.1080/16000870.2017.1406263

Ríos-Cornejo, D., Penas, Á., Álvarez-Esteban, R., del Río, S., 2015. Links between teleconnection patterns and precipitation in Spain. Atmos Res 156, 14–28.

Robertson, A.W., Mechoso, C.R., Kim, Y.-J., 2000. The Influence of Atlantic Sea Surface Temperature Anomalies on the North Atlantic Oscillation. J Clim 13, 122–138. https://doi.org/10.1175/1520-0442(2000)013<0122:TIOASS>2.0.CO;2

Rousi, E., Rust, H.W., Ulbrich, U., Anagnostopoulou, C., 2020. Implications of Winter NAO Flavors on Present and Future European Climate. Climate 8, 13. https://doi.org/10.3390/cli8010013

Sánchez-García, E., Pardo-Pascual, J.E., Balaguer-Beser, A., Almonacid-Caballer, J., 2015. Analysis of the shoreline position extracted from landsat TM and ETM+ imagery. International Archives of the Photogrammetry, Remote Sensing and Spatial Information Sciences - ISPRS Archives 40, 991–998. https://doi.org/10.5194/isprsarchives-XL-7-W3-991-2015

Sarti, G., Bini, M., Giacomelli, S., 2010. The growth and the decline of Pisa (Tuscany, Italy) up to the Middle ages: correlations with landscape and geology. Quat. Ital. J. Quat. Sci. 23, 311–322.

Sarti, G., Rossi, V., Amorosi, A., Bini, M., Giacomelli, S., Pappalardo, M., Ribecai, C., Ribolini, A., Sammartino, I., 2015. Climatic signature of two mid–late Holocene fluvial incisions formed under sea-level highstand conditions (Pisa coastal plain, NW Tuscany, Italy). Palaeogeogr Palaeoclimatol Palaeoecol 424, 183–195. https://doi.org/https://doi.org/10.1016/j.palaeo.2015.02.020

Seabold, S., Perktold, J., 2010. statsmodels: Econometric and statistical modeling with python, in: 9th Python in Science Conference.

Shaw, S.B., Royem, A.A., Riha, S.J., 2011. The relationship between extreme hourly precipitation and surface temperature in different hydroclimatic regions of the United States. J Hydrometeorol 12, 319–325.

Sit, M., Demiray, B.Z., Xiang, Z., Ewing, G.J., Sermet, Y., Demir, I., 2020. A comprehensive review of deep learning applications in hydrology and water resources. Water Science and Technology. https://doi.org/10.2166/wst.2020.369

Smith, R.K., Bryan, K.R., 2007. Monitoring Beach Face Volume with a Combination of Intermittent Profiling and Video Imagery. J Coast Res 2007, 892–898. https://doi.org/10.2112/04-0287.1

Spearman, C., 1904. The proof and measurement of association between two things. Am J Psychol 15, 72–101. https://doi.org/10.2307/1412159

Stagl, J., Mayr, E., Koch, H., Hattermann, F.F., Huang, S., 2014. Effects of Climate Change on the Hydrological Cycle in Central and Eastern Europe BT - Managing Protected Areas in Central and Eastern Europe Under Climate Change, in: Rannow, S., Neubert, M. (Eds.), . Springer Netherlands, Dordrecht, pp. 31–43.

Stockdon, H.F., Sallenger, A.H., List, J.H., Holman, R.A., 2002. Estimation of shoreline position and change using airborne topographic lidar data. J Coast Res 18, 502–513.

Sutskever, I., Vinyals, O., Le, Q. v., 2014. Sequence to Sequence Learning with Neural Networks.

Syvitski, J.P.M., Kettner, A.J., Overeem, I., Hutton, E.W.H., Hannon, M.T., Brakenridge, G.R., Day, J., Vörösmarty, C., Saito, Y., Giosan, L., Nicholls, R.J., 2009. Sinking deltas due to human activities. Nat Geosci 2, 681–686. https://doi.org/10.1038/ngeo629

Templin, T., Popielarczyk, D., Kosecki, R., 2018. Application of Low-Cost Fixed-Wing UAV for Inland Lakes Shoreline Investigation. Pure Appl Geophys 175, 3263–3283. https://doi.org/10.1007/s00024-017-1707-7

Tessler, Z.D., Vörösmarty, C.J., Grossberg, M., Gladkova, I., Aizenman, H., 2016. A global empirical typology of anthropogenic drivers of environmental change in deltas. Sustain Sci 11, 525–537. https://doi.org/10.1007/s11625-016-0357-5

Tien Bui, D., Hoang, N.-D., Martínez-Álvarez, F., Ngo, P.-T.T., Hoa, P.V., Pham, T.D., Samui, P., Costache, R., 2020. A novel deep learning neural network approach for predicting flash flood susceptibility: A case study at a high frequency tropical storm area. Science of The Total Environment 701, 134413. https://doi.org/https://doi.org/10.1016/j.scitotenv.2019.134413

Toimil, A., Camus, P., Losada, I.J., le Cozannet, G., Nicholls, R.J., Idier, D., Maspataud, A., 2020. Climate change-driven coastal erosion modelling in temperate sandy beaches: Methods and uncertainty treatment. Earth Sci Rev 202, 103110. https://doi.org/https://doi.org/10.1016/j.earscirev.2020.103110

Toniolo, A.R., 1927. Le variazioni storiche del litorale toscano fra l'Arno e il Magra, in: Atti Del X Congresso Geografico Italiano. Milan.

Toniolo, A.R., 1910. Sulle Variazioni di spiaggia a foce d'Arno (Marina di Pisa) dalla fine del secolo XViii ai nostri giorni: Studio storico fisiografico, Tipografia Municipale. Tipografia Municipale, Pisa.

Toniolo, A R, 1910. Sulle Variazioni di spiaggia a foce d'Arno (Marina di Pisa) dalla fine del secolo XViii ai nostri giorni: Studio storico fisiografico, Tipografia Municipale. Tipografia Municipale, Pisa.

Tramblay, Y., el Adlouni, S., Servat, E., 2013. Trends and variability in extreme precipitation indices over Maghreb countries. Natural Hazards and Earth System Sciences 13, 3235–3248. https://doi.org/10.5194/nhess-13-3235-2013

Tramblay, Y., Llasat, M.C., Randin, C., Coppola, E., 2020. Climate change impacts on water resources in the Mediterranean. Reg Environ Change 20, 83. https://doi.org/10.1007/s10113-020-01665-y

Trenberth, K.E., Dai, A., Rasmussen, R.M., Parsons, D.B., 2003. The changing character of precipitation. Bull Am Meteorol Soc 84, 1205–1218.

Trigo, I.F., Bigg, G.R., Davies, T.D., 2002. Climatology of Cyclogenesis Mechanisms in the Mediterranean.

Trigo, R.M., Pozo-Vázquez, D., Osborn, T.J., Castro-Díez, Y., Gámiz-Fortis, S., Esteban-Parra, M.J., Pozo-Vázquez, D., Osborn, T.J., Castro-Díez, Y., Gámiz-Fortis, S., Esteban-Parra, M.J., 2004. North Atlantic

Oscillation influence on precipitation, river flow and water resources in the Iberian Peninsula. Int J Climatol 24, 925–944. https://doi.org/10.1002/joc.1048

van den Brink, H.W., Können, G.P., Opsteegh, J.D., van Oldenborgh, G.J., Burgers, G., 2005. Estimating return periods of extreme events from ECMWF seasonal forecast ensembles. International Journal of Climatology 25, 1345–1354. https://doi.org/10.1002/joc.1155

van Rossum, G., Drake, F.L., 2009. Python 3 Reference Manual. CreateSpace, Scotts Valley, CA.

Van, S.P., Le, H.M., Thanh, D.V., Dang, T.D., Loc, H.H., Anh, D.T., 2020. Deep learning convolutional neural network in rainfall–runoff modelling. Journal of Hydroinformatics 22, 541–561. https://doi.org/10.2166/hydro.2020.095

Vergni, L., Chiaudani, A., 2015. RELATIONSHIP BETWEEN THE NAO INDEX AND SOME INDICES OF EXTREME PRECIPITATION IN THE ABRUZZO REGION.

Vergni, L., di Lena, B., Chiaudani, A., 2016. Statistical characterisation of winter precipitation in the Abruzzo region (Italy) in relation to the North Atlantic Oscillation (NAO). Atmos Res 178–179, 279–290. https://doi.org/https://doi.org/10.1016/j.atmosres.2016.03.028

Vicente-Serrano, S.M., López-Moreno, J.I., 2008. Nonstationary influence of the North Atlantic Oscillation on European precipitation. Journal of Geophysical Research: Atmospheres 113. https://doi.org/10.1029/2008JD010382

Virtanen, P., Gommers, R., Oliphant, T.E., Haberland, M., Reddy, T., Cournapeau, D., Burovski, E., Peterson, P., Weckesser, W., Bright, J., van der Walt, S.J., Brett, M., Wilson, J., Millman, K.J., Mayorov, N., Nelson, A.R.J., Jones, E., Kern, R., Larson, E., Carey, C.J., Polat, \.Ilhan, Feng, Y., Moore, E.W., VanderPlas, J., Laxalde, D., Perktold, J., Cimrman, R., Henriksen, I., Quintero, E.A., Harris, C.R., Archibald, A.M., Ribeiro, A.H., Pedregosa, F., van Mulbregt, P., SciPy 1.0 Contributors, 2020. SciPy 1.0: Fundamental Algorithms for Scientific Computing in Python. Nat Methods 17, 261–272. https://doi.org/10.1038/s41592-019-0686-2

Visbeck, M.H., Hurrell, J.W., Polvani, L., Cullen, H.M., 2001. The North Atlantic Oscillation: Past, present, and future. Proceedings of the National Academy of Sciences 98, 12876. https://doi.org/10.1073/pnas.231391598

Visser, J.B., Wasko, C., Sharma, A., Nathan, R., 2021. Eliminating the Hook in Precipitation Temperature Scaling. J Clim 34, 9535–9549. https://doi.org/10.1175/JCLI-D-21-0292.1

Vos, K., Harley, M.D., Splinter, K.D., Simmons, J.A., Turner, I.L., 2019a. Sub-annual to multi-decadal shoreline variability from publicly available satellite imagery. Coastal Engineering 150, 160–174. https://doi.org/10.1016/j.coastaleng.2019.04.004

Vos, K., Splinter, K.D., Harley, M.D., Simmons, J.A., Turner, I.L., 2019b. CoastSat: A Google Earth Engine-enabled Python toolkit to extract shorelines from publicly available satellite imagery. Environmental Modelling and Software 122, 104528. https://doi.org/10.1016/j.envsoft.2019.104528

Wang, C., Dong, S., 2010. Is the basin-wide warming in the North Atlantic Ocean related to atmospheric carbon dioxide and global warming? Geophysical Research Letters - GEOPHYS RES LETT 37. https://doi.org/10.1029/2010GL042743

Wasko, C., Sharma, A., 2014. Quantile regression for investigating scaling of extreme precipitation with temperature. Water Resour Res 50, 3608–3614. https://doi.org/https://doi.org/10.1002/2013WR015194

Wentz, F.J., Ricciardulli, L., Hilburn, K., Mears, C., 2007. How much more rain will global warming bring? Science (1979) 317, 233–235.

West, H., Quinn, N., Horswell, M., 2019. Regional rainfall response to the North Atlantic Oscillation (NAO) across Great Britain. Hydrology Research 50, 1549–1563. https://doi.org/10.2166/nh.2019.015

Westoby, M.J., Brasington, J., Glasser, N.F., Hambrey, M.J., Reynolds, J.M., 2012. 'Structure-from-Motion'' photogrammetry: A low-cost, effective tool for geoscience applications.' Geomorphology 179, 300–314. https://doi.org/https://doi.org/10.1016/j.geomorph.2012.08.021

Westra, S., Fowler, H.J., Evans, J.P., Alexander, L. v, Berg, P., Johnson, F., Kendon, E.J., Lenderink, G., Roberts, N., 2014. Future changes to the intensity and frequency of short-duration extreme rainfall. Reviews of Geophysics 52, 522–555.

Xu, H., Taylor, R.G., Xu, Y., 2011. Quantifying uncertainty in the impacts of climate change on river discharge in sub-catchments of the Yangtze and Yellow River Basins, China. Hydrol. Earth Syst. Sci. 15, 333–344. https://doi.org/10.5194/hess-15-333-2011

Yi, A., Li, Z., Gan, M., Zhang, Y., Yu, D., Chen, W., Ju, Y., 2019. A deep learning approach on short-term spatiotemporal distribution forecasting of dockless bike-sharing system. Neural Comput Appl 31, 1–13. https://doi.org/10.1007/s00521-018-3470-9

Zhang, A., Gao, R., XixiWang, Liu, T., Fang, L., 2020. Historical Trends in Air Temperature , Precipitation ,. Water (Basel) 12.

Zheng, J., Fu, X., Zhang, G., 2019. Research on Exchange Rate Forecasting Based on Deep Belief Network. Neural Comput. Appl. 31, 573–582. https://doi.org/10.1007/s00521-017-3039-z